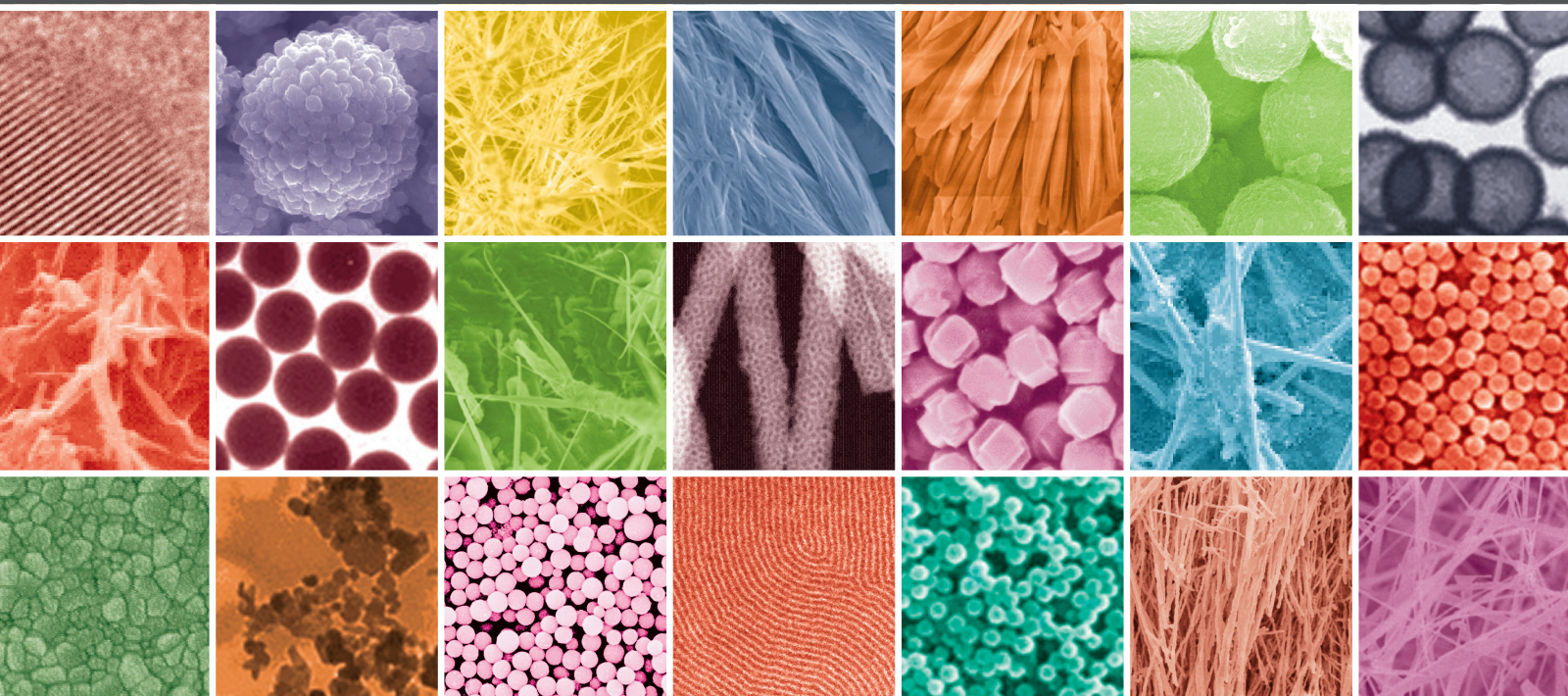


Low-Dimensional Nanomaterials and Their Functional Architectures: Synthesis, Properties, and Applications

Lead Guest Editor: Weilu Gao

Guest Editors: Ciyan Qiu and Xiaowei He



Low-Dimensional Nanomaterials and Their Functional Architectures: Synthesis, Properties, and Applications

Low-Dimensional Nanomaterials and Their Functional Architectures: Synthesis, Properties, and Applications

Lead Guest Editor: Weilu Gao

Guest Editors: Ciyan Qiu and Xiaowei He



Copyright © 2017 Hindawi. All rights reserved.

This is a special issue published in "Journal of Nanomaterials." All articles are open access articles distributed under the Creative Commons Attribution License, which permits unrestricted use, distribution, and reproduction in any medium, provided the original work is properly cited.

Editorial Board

Domenico Acierno, Italy	Kimberly Hamad-Schifferli, USA	Alessandro Pegoretti, Italy
Katerina Aifantis, USA	Simo-Pekka Hannula, Finland	Oscar Perales-Pérez, Puerto Rico
Nageh K. Allam, USA	Michael Harris, USA	Jorge Pérez-Juste, Spain
Margarida Amaral, Portugal	Yasuhiko Hayashi, Japan	Alexey P. Popov, Finland
Martin Andersson, Sweden	Michael Z. Hu, USA	Helena Prima-García, Spain
Raul Arenal, Spain	Nay Ming Huang, Malaysia	Alexander Pyatenko, Japan
Ilaria Armentano, Italy	Zafar Iqbal, USA	You Qiang, USA
Vincenzo Baglio, Italy	Balachandran Jeyadevan, Japan	Philip D. Rack, USA
Lavinia Balan, France	Jeong-won Kang, Republic of Korea	Peter Reiss, France
Thierry Baron, France	Hassan Karimi-Maleh, Iran	Ilker S. Bayer, Italy
Andrew R. Barron, USA	Antonios Kelarakis, UK	Sudipta Seal, USA
Hongbin Bei, USA	Alireza Khataee, Iran	Shu Seki, Japan
Stefano Bellucci, Italy	Ali Khorsand Zak, Iran	Donglu Shi, USA
Enrico Bergamaschi, Italy	Philippe Knauth, France	Bhanu P. Singh, India
Debes Bhattacharyya, New Zealand	Prashant Kumar, UK	Surinder Singh, USA
Sergio Bietti, Italy	Eric Le Bourhis, France	Vladimir Sivakov, Germany
Giovanni Bongiovanni, Italy	Jun Li, Singapore	Adolfo Speghini, Italy
Mohamed Bououdina, Bahrain	Meiyong Liao, Japan	Marinella Striccoli, Italy
Philippe Caroff, Australia	Shijun Liao, China	Xuping Sun, KSA
Victor M. Castaño, Mexico	Silvia Licoccia, Italy	Ashok K. Sundramoorthy, India
Albano Cavaleiro, Portugal	Nathan C. Lindquist, USA	Angelo Taglietti, Italy
Bhanu P. S. Chauhan, USA	Zainovia Lockman, Malaysia	Bo Tan, Canada
Shafiu Chowdhury, USA	Jim Low, Australia	Leander Tapfer, Italy
Jin-Ho Choy, Republic of Korea	Laura M. Maestro, Spain	Valeri P. Tolstoy, Russia
Yu-Lun Chueh, Taiwan	Gaurav Mago, USA	Muhammet S. Toprak, Sweden
Elisabetta Comini, Italy	Muhamamd A. Malik, UK	R. Torrecillas, Spain
Giuseppe Compagnini, Italy	Francesco Marotti de Sciarra, Italy	Achim Trampert, Germany
David Cornu, France	Sanjay R. Mathur, Germany	Takuya Tsuzuki, Australia
Miguel A. Correa-Duarte, Spain	Tony McNally, UK	Tamer Uyar, Turkey
P. Davide Cozzoli, Italy	Yogendra Mishra, Germany	Luca Valentini, Italy
Yong Ding, USA	Paulo Cesar Morais, Brazil	Antonio Vassallo, Italy
Zehra Durmus, Turkey	Paul Munroe, Australia	Ester Vazquez, Spain
Joydeep Dutta, Oman	Jae-Min Myoung, Republic of Korea	Ajayan Vinu, Australia
Ovidiu Ersen, France	Rajesh R. Naik, USA	Ruibing Wang, Macau
Claude Estournès, France	Albert Nasibulin, Russia	Shiren Wang, USA
Andrea Falqui, KSA	Toshiaki Natsuki, Japan	Yong Wang, USA
Matteo Ferroni, Italy	Natalia Noginova, USA	Magnus Willander, Sweden
Ilaria Fratoddi, Italy	Sherine Obare, USA	Ping Xiao, UK
Miguel A. Garcia, Spain	Won-Chun Oh, Republic of Korea	Zhi Li Xiao, USA
Siddhartha Ghosh, Singapore	Abdelwahab Omri, Canada	Yoke K. Yap, USA
Filippo Giubileo, Italy	Ungyu Paik, Republic of Korea	William Yu, USA
Fabien Grasset, France	Piersandro Pallavicini, Italy	Michele Zappalorto, Italy
Jean M. Gremec, France	Edward A. Payzant, USA	Renyun Zhang, Sweden

Contents

Low-Dimensional Nanomaterials and Their Functional Architectures: Synthesis, Properties, and Applications

Weilu Gao, Ciyan Qiu, and Xiaowei He
Volume 2017, Article ID 7350491, 2 pages

Fabrication of a Large-Area Superhydrophobic SiO₂ Nanorod Structured Surface Using Glancing Angle Deposition

Xun Lu, Seok-min Kim, and Seong Jun Seo
Volume 2017, Article ID 8305439, 7 pages

Viscosity and Morphology Modification of Length Sorted Single-Walled Carbon Nanotubes in PIB Matrices

Hanxiao Huang, Bohao Li, Clayton E. Simien, and Daneesh O. Simien
Volume 2017, Article ID 5691692, 9 pages

CO Gas-Induced Resonance Frequency Shift of ZnO-Functionalized Microcantilever in Humid Air

Lia Aprilia, Ratno Nuryadi, Dwi Gustiono, Nurmahmudi, Arief Udharto, Djoko Hartanto, Brian Yuliarto, Makoto Hosoda, Yoichiro Neo, and Hidenori Mimura
Volume 2017, Article ID 4824607, 7 pages

Magnetic-Field-Enhanced Morphology of Tin Oxide Nanomaterials for Gas Sensing Applications

Jonathan C. Briones, Gwen Castillon, Michael P. Delmo, and Gil Nonato C. Santos
Volume 2017, Article ID 4396723, 11 pages

Investigating Visible-Photocatalytic Activity of MoS₂/TiO₂ Heterostructure Thin Films at Various MoS₂ Deposition Times

Hang Nguyen Thai Phung, Van Nguyen Khanh Tran, Lam Thanh Nguyen, Loan Kieu Thi Phan, Phuong Ai Duong, and Hung Vu Tuan Le
Volume 2017, Article ID 3197540, 6 pages

Facile Hydrothermal Synthesis of SnO₂ Nanospheres as Photocatalysts

Wenquan Hu and Xiaoguang Yuan
Volume 2017, Article ID 6976203, 6 pages

Spawns Structure of Rod-Like ZnO Wrapped in Cellulose Nanofibers for Electromagnetic Wave Absorption

Bitao Fan, Qiufang Yao, Chao Wang, Ye Xiong, Qingfeng Sun, and Chunde Jin
Volume 2017, Article ID 6329072, 6 pages

Influence of Heat Treatment on the Morphologies of Copper Nanoparticles Based Films by a Spin Coating Method

Wei Liu, Jiayu Guo, Zhonghua Fan, Xiaorong Wang, Dingkun Yu, Rong Chen, Shisheng Huang, and Peng He
Volume 2017, Article ID 4301768, 6 pages

Editorial

Low-Dimensional Nanomaterials and Their Functional Architectures: Synthesis, Properties, and Applications

Weilu Gao,¹ Ciyan Qiu,² and Xiaowei He³

¹Department of Electrical and Computer Engineering, Rice University, Houston, TX 77005, USA

²Department of Electrical Engineering, Shanghai Jiao Tong University, Shanghai 200240, China

³Los Alamos National Laboratory, Los Alamos, NM 87545, USA

Correspondence should be addressed to Weilu Gao; weilu.gao@rice.edu

Received 10 September 2017; Accepted 14 September 2017; Published 26 October 2017

Copyright © 2017 Weilu Gao et al. This is an open access article distributed under the Creative Commons Attribution License, which permits unrestricted use, distribution, and reproduction in any medium, provided the original work is properly cited.

The objective of this special issue is to address recent research trends and developments in the synthesis and applications of low-dimensional materials and their functional architectures. A substantial number of papers were submitted, and after a thorough peer review process, eight papers were selected to be included in this special issue. These papers cover advances in diverse topics, covering a wide range of low-dimensional materials. We believe that the original papers collected in this special issue highlight the contemporary topics in research related to low-dimensional materials and will introduce readers to the latest advances in this field.

In the paper by J. C. Briones et al., SnO₂ nanowires were first grown using the horizontal vapor phase growth (HVPG) technique. Next, the authors found that the length of nanowires was significantly enhanced by the application of EMF. The aspect ratio, as well as the density of the fabricated nanowires, increased with increasing magnetic field intensity.

In the paper by H. N. T. Phung et al., MoS₂/TiO₂ heterostructure thin films were fabricated using sol-gel and chemical bath deposition methods. Crystal structure, surface morphology, chemical states of all elements, and optical property of the obtained thin films were fully characterized by various techniques. The obtained MoS₂/TiO₂ heterostructure thin films exhibit higher visible light photocatalytic activity than that of pure MoS₂ and TiO₂ counterparts. The optimization of MoS₂/TiO₂ fabrication process together with the mechanism of the enhancement was also discussed.

The paper by B. Fan et al. described the fabrication of spawns structure of rod-like ZnO wrapped in the cellulose nanofibers through a facile one-step hydrothermal method. The composite aerogel in a wax matrix exhibited

excellent electromagnetic wave absorption performance over 2–18 GHz.

The paper by X. Lu et al. developed a glancing angle deposition (GLAD) technique to generate SiO₂ nanorods for a low-cost superhydrophobic functional nanostructured surface. The wettability of the surface was characterized under various fabrication parameters, and a maximum contact angle of 157° was obtained. Furthermore, optically transparent films have been demonstrated to serve as superhydrophobic functional nanostructures for optical applications.

The paper by W. Liu et al. investigated the influence of heat treatment on the morphologies of copper nanoparticles based films on glass slides with a spin coating method. Using TG, XRD, and SEM techniques, it showed that heat treatment can modify the sizes and morphologies of copper nanoparticles. Significant coarsening of copper nanoparticles occurs when the heating temperature is above 200°C.

The paper by W. Hu and X. Yuan reported a facile route to synthesize SnO₂ nanospheres at large scale. The SnO₂ nanospheres were synthesized through a simple and effective hydrothermal method with average diameter of 40 nm. The as-prepared product was used as the photocatalyst for several dyes under UV light irradiation. The results indicate that these nanospheres have high photocatalytic activities and might be a potential candidate in wastewater purification.

The paper by L. Aprilia et al. is about a microcantilever gas sensor based on zinc oxide microrods. ZnO microrods were grown on the microcantilever surface and the measurement of resonance frequency of the microcantilever vibrations under the exposure of CO gas was carried out. The results showed that the resonance frequency is shifted by water vapor

condition. An exchange mechanism of CO and water was used to explain the shift of resonance frequency.

The paper by H. Huang et al. studied length dependence of carbon nanotubes on the viscosity of carbon nanotube-polymer composites. The effects of nanotube length and weight fraction on the polyisobutylene matrices were evaluated with thermal and rheological testing. It showed that viscosity of the nanocomposite systems depended on the nanotube length, indicating the non-Einstein-like behavior of the viscosity in these composite systems.

Acknowledgments

We would like to thank all the authors who contributed to this special issue. This publication would not be possible without the participation of our expert reviewers who provided vital constructive feedback and criticism throughout the review process.

*Weilu Gao
Ciyuan Qiu
Xiaowei He*

Research Article

Fabrication of a Large-Area Superhydrophobic SiO₂ Nanorod Structured Surface Using Glancing Angle Deposition

Xun Lu,¹ Seok-min Kim,¹ and Seong Jun Seo²

¹School of Mechanical Engineering, Chung-Ang University, Seoul 06974, Republic of Korea

²Department of Dermatology, Chung-Ang University Hospital, Seoul 06973, Republic of Korea

Correspondence should be addressed to Seok-min Kim; smkim@cau.ac.kr and Seong Jun Seo; drseo@cau.ac.kr

Received 24 April 2017; Accepted 21 August 2017; Published 16 October 2017

Academic Editor: Weilu Gao

Copyright © 2017 Xun Lu et al. This is an open access article distributed under the Creative Commons Attribution License, which permits unrestricted use, distribution, and reproduction in any medium, provided the original work is properly cited.

A glancing angle deposition (GLAD) technique was used to generate SiO₂ nanorods on a glass substrate to fabricate a low-cost superhydrophobic functional nanostructured surface. GLAD-deposited SiO₂ nanorod structures were fabricated using various deposition rates, substrate rotating speeds, oblique angles, and deposition times to analyze the effects of processing conditions on the characteristics of the fabricated functional nanostructures. The wettability of the surface was measured after surface modification with a self-assembled monolayer (SAM). The measured water contact angles were primarily affected by substrate rotation speed and oblique angle because the surface fraction of the GLAD nanostructure was mainly affected by these parameters. A maximum contact angle of 157° was obtained from the GLAD sample fabricated at a rotation speed of 5 rpm and an oblique angle of 87°. Although the deposition thickness (height of the nanorods) was not a dominant factor for determining the wettability, we selected a deposition thickness of 260 nm as the optimum processing condition based on the measured optical transmittance of the samples because optically transparent films can serve as superhydrophobic functional nanostructures for optical applications.

1. Introduction

Optically transparent multifunctional surfaces play an important role in photovoltaic applications for improving or maintaining system performance. Incident solar energy on the photovoltaic modules is decreased through both surface contamination on the outdoor panels and optical reflection at the interface between the air and packaging glass. It is therefore important to develop optically transparent self-cleaning surfaces with low optical reflectance. In practical operating conditions for solar cells, surface contamination of the photovoltaic modules by dust accumulation is always possible. It has been reported that the accumulation of dust on the window of a solar cell causes degradation in the solar cell efficiency [1, 2]. It is commonly claimed that superhydrophobic surfaces can provide self-cleaning windows in solar cell applications [3, 4]. There are two main approaches that can be considered to increase surface hydrophobicity. One approach is to decrease the surface energy by modifying the surface chemistry, and the other is to create a geometrical structure with a material that has a low surface energy [5, 6].

Although chemical treatment of the surface is convenient, the maximum contact angle attainable on a flat surface with the lowest free energy coating is only 115.2°, as pointed out by Nakajima [7]. Also, since reflection loss is caused by a mismatch in refractive indices, it is not feasible to reduce the reflective optical loss by chemical modification. Higher contact angles can be easily obtained by changing the surface morphology with nanostructures. In addition, nanostructured surfaces both increase the contact angle and increase the optical transmittance due to gradient refractive index effects [8].

Various methods have been tried to create a nanostructured hydrophobic surface with antireflective properties including photolithography [9], chemical etching [10], and plasma enhanced chemical vapor deposition [11]. However, these techniques have limitations that make it difficult to fabricate well-controlled uniform nanostructures on large-area substrates at low cost, which is important for commercialization of superhydrophobic functional nanostructured surfaces. Although a polymer nanoimprinting technique has been proposed to fabricate well-controlled uniform

nanostructures on a large-area substrate at low cost [12], the imprinted nanostructure cannot guarantee long-term stability in an outdoor environment because the different thermal expansion coefficients of the substrate and imprinted layer might cause a delamination problem.

In this paper, we fabricated a SiO_2 nanorod structured superhydrophobic surface on a glass substrate using a glancing angle deposition (GLAD) technique. GLAD is an effective method of fabricating nanostructures on large areas with various materials at low cost, and the shape of a GLAD nanostructure can be easily controlled by changing the processing parameters. In previous reports, superhydrophobic [13, 14] and antireflection surfaces [15, 16] were fabricated using a GLAD technique, but these surfaces are limited as they cannot provide both characteristics at the same time. In this study, we fabricated superhydrophobic and antireflection surfaces using SiO_2 nanorod structures on a conventional glass substrate by employing the GLAD technique. SiO_2 nanorods with various surface morphologies were fabricated under various deposition rates, substrate rotation speeds, oblique angles, and deposition thicknesses to optimize the processing parameters of the GLAD process and maximize the hydrophobicity of the nanostructures. After an additional coating with a self-assembled monolayer (SAM) on the SiO_2 nanorods, water contact angles (WCAs) were measured and compared with that of the theoretical model. Finally, optimal processing parameters of the GLAD process were selected for maximizing water repellency and optical transmittance.

2. Experimental

2.1. Fabrication of the Functional Nanostructured Surface. GLAD is a physical vapor deposition process in which deposition flux is incident onto the substrate at a large oblique angle with respect to the surface normal ($75^\circ \sim 90^\circ$) [17]. GLAD is a single-step fabrication process providing a columnar morphology using the “shadowing effect” and precise in-plane rotation of the substrate. At the early stage of the GLAD process, the deposited particles are randomly scattered and form island structures on the substrate. As the deposition proceeds, the initial nucleated islands act as shadowing centers, with the taller islands receiving more impinging particles than the shorter ones (shadowing effect). This competition causes the taller islands to grow into columns, resulting in the formation of nanorod structures [18–20]. In this study, SiO_2 nanorod structures were fabricated on a $3 \times 1 \text{ inch}^2$ glass slide substrate by the GLAD technique using an electron beam evaporator (Modified SEE-7, Ultech, Co., Ltd., Korea) equipped with a sample holder capable of oblique angle deposition and rotation speed control. Prior to the deposition process, the glass slide substrates were cleaned in a sonication bath using acetone, isopropyl alcohol (IPA), and deionized water for 15 min each. The cleaned substrates were dried with nitrogen gas and mounted on a substrate holder in an electron beam evaporator, and the evaporation chamber was pumped down using a cryopump supported by a mechanical pump until it reached a base pressure of 6.0×10^{-7} Torr. The vacuum pressure during the evaporation was less than 5.0×10^{-6} Torr, and the growth rate during the deposition was monitored

by employing a quartz crystal microbalance positioned at an incidence angle normal to the vapor source. The distance between the evaporation source and the rotating substrate was 680 mm. SiO_2 pellets (RND Korea, 99.999%) were used as a source material for the nanorods. In each experiment, the GLAD SiO_2 nanorods were deposited on 2 glass slide substrates and a $1 \times 1 \text{ cm}^2$ silicon substrate. The GLAD structures on the glass slide substrates were used to measure the WCA and optical transmittance, and those on the silicon substrates were used for scanning electron microscopy (SEM) measurements. To examine the effects of surface morphology on WCA and optical transmittance, various SiO_2 nanorod structures were fabricated at deposition rates of 5 and 10 Å/s, substrate rotation speeds of 0.2 to 20 rpm, oblique angles of 82° to 87° , and deposition thicknesses of 260 to 500 nm. The surfaces of the fabricated SiO_2 nanostructures were modified by a silane self-assembled monolayer (SAM) coating to reduce the surface energy. The SAM coating was achieved by dipping the nanostructured glass slide into a 2% solution of dimethyldichlorosilane dissolved in octamethylcyclotetrasilane.

2.2. Measurement and Analysis of WCA on the Functional Nanostructured Surface. To evaluate the effect of nanostructure morphology on the water repellent properties, WCA was measured using a drop dispensing method at room temperature. A microdropper was utilized to dispense $10 \mu\text{L}$ drops of distilled water droplets onto a sample. An imaging system was employed to capture a static contact angle image, and the contact angle was calculated by imaging processing. To obtain reliable WCA measurements, the WCAs were measured at four random places on each sample, and 2 samples fabricated under the same conditions were used for the measurement. The average values and standard deviation of 8 WCA measurements were used for the analysis.

To explain the relationship between WCA and the morphology of the SiO_2 nanostructure, the measured WCAs were compared with the values obtained from theoretical models, including the Wenzel model [21] and the Cassie-Baxter model [22]. In the Wenzel model, the water droplet penetrates into the nanostructured surface, and no air gap is trapped on the surface. Under this condition, the apparent WCA is described according to the following equation:

$$\cos \theta_w = r \cos \theta_0. \quad (1)$$

Here, θ_w is the theoretical WCA of the nanostructured surface according to the Wenzel model, θ_0 is the measured WCA of the flat surface, and r is the roughness factor, which is defined as the ratio of the actual surface area of the nanostructures to their horizontal projection. In the Cassie-Baxter model, the water droplet cannot penetrate into the nanostructured surface, and the air gap is trapped between the nanostructures and the water droplet. The apparent contact angle in this state is described by

$$\cos \theta_c = f (\cos \theta_0 + 1) - 1. \quad (2)$$

Here, θ_c is the theoretical WCA for the Cassie-Baxter model, and f is the ratio of the solid surface in contact

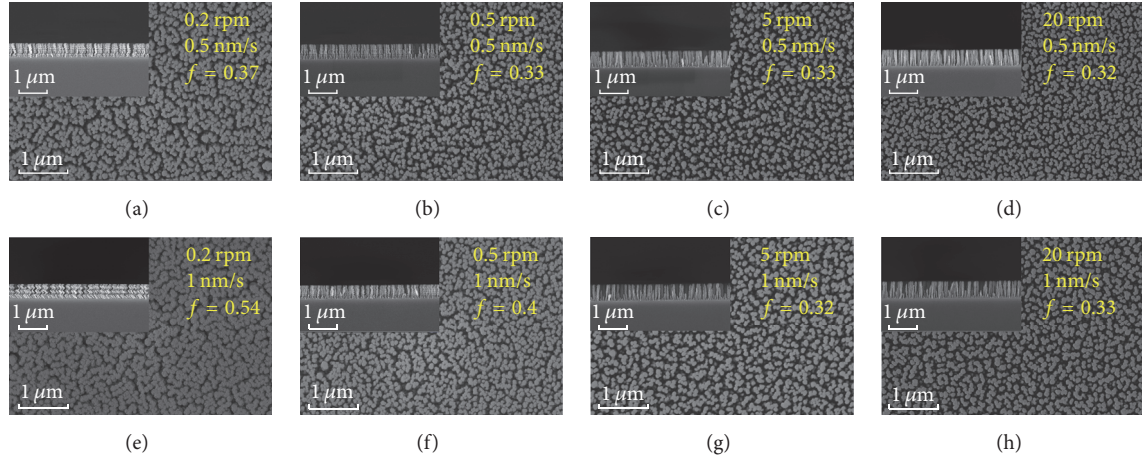


FIGURE 1: Top-view and cross-sectional view SEM images of GLAD SiO₂ nanorods fabricated at different deposition rates of 5 Å/s and 10 Å/s and different substrate rotation speeds of 0.2–20 rpm. The left top inset in each top-view SEM image is the cross-sectional view SEM image. The deposition rate, rotation speed, and the solid fraction are indicated on the right top of each SEM image.

with the water droplet (top area of the columnar structures) to the horizontal projection. The roughness factor (r) or solid fraction ratio (f) must be determined to calculate the predicted WCA for the Wenzel model or the Cassie-Baxter model. Since the GLAD nanorod structure can be simplified as a circular pedestal, the roughness factor (r) and solid fraction ratio (f) can be obtained using the following equations:

$$r = \frac{s + n(\pi dh)}{s} = 1 + \frac{n\pi dh}{s}, \quad (3)$$

$$f = \frac{n\pi d^2}{4s}.$$

Here, d and h are the diameter and height of the nanorod, respectively; n is the number of nanorods per unit area, and s is the size of the unit area. Eventually, we developed two equations describing Wenzel and Cassie-Baxter angles as a function of nanorod geometry as described below:

$$\theta_w = \cos^{-1} [r \cos \theta_0], \quad (4)$$

$$\theta_c = \cos^{-1} [f (\cos \theta_0 + 1) - 1].$$

An image analysis technique was carried out using top-view SEM images to determine n , d , and s values. The grayscale SEM image was converted to a binary image by subtracting the background and adjusting the image contrast. The number (n) and diameter (d) of the nanorods were obtained from the converted binary top-view SEM images (white regions in the binary image were considered to be the top of a single nanorod), and the whole area of the SEM image was considered as the unit area (s). The height (h) of the nanorod was obtained from the cross-sectional SEM image.

In this research, the measured water contact angle (θ_0) of flat SiO₂ after SAM treatment was 103.9°. The Wenzel model loses its physical meaning when $\cos \theta_w$ is larger than 1, and $\cos \theta_w$ is larger than 1 when the r value is larger

than 4.2. In this research, the calculated r value from the top-view SEM image of samples was larger than 5 except for the samples fabricated at an incident angle of 87°. In addition, the theoretical WCAs of the Wenzel model for the samples prepared at an incident angle of 87° did not match the experimental results. Therefore, the theoretical WCAs of this research were calculated using the Cassie-Baxter model.

2.3. Light Transmittance Measurement. Since the proposed SiO₂ nanorod structure can provide both hydrophobicity and antireflection characteristics, the light transmittance of the fabricated samples was also measured and analyzed. The optical transmittance of the fabricated SiO₂ nanorod structure on a glass slide substrate was measured using a spectrophotometer (UV-670 UV-Vis, Jasco Inc., USA) in the visible range.

3. Results and Discussion

3.1. Effects of Substrate Rotation Speed and Deposition Rate on WCA. To examine the effects of substrate rotation speed and deposition rate on the surface morphology and WCA, SiO₂ nanostructures were fabricated using a GLAD technique under the following conditions: substrate rotation from 0.2 to 20 rpm, deposition rates of 5 and 10 Å/s, a fixed thickness of 500 nm, and a fixed oblique angle of 82°. Figure 1 shows the SEM images of the fabricated GLAD nanostructures at different fabrication conditions, where the cross-sectional SEM images of each fabricated sample were inset in the top-view SEM image of the GLAD nanostructures. The rotation speed, deposition rate, and solid fraction ratio are indicated on the right top of the SEM images. In the cross-sectional SEM images, the nanorod shape changed from spiral to a straight vertical shape with increasing rotation speed. In the case of the spiral shape (Figures 1(a), 1(b), 1(e), and 1(f)), the f value and the diameter of the spiral structure decreased with increasing rotation speed and decreasing deposition rate. In the case of the vertical shape (Figures 1(c), 1(d), 1(g), and 1(h))),

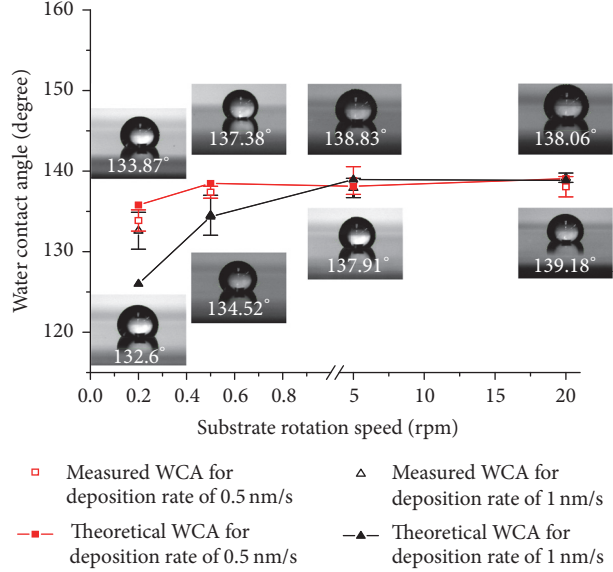


FIGURE 2: Effects of substrate rotation speed and deposition rate on the measured and theoretical (Cassie-Baxter model) WCAs of GLAD nanorod substrates.

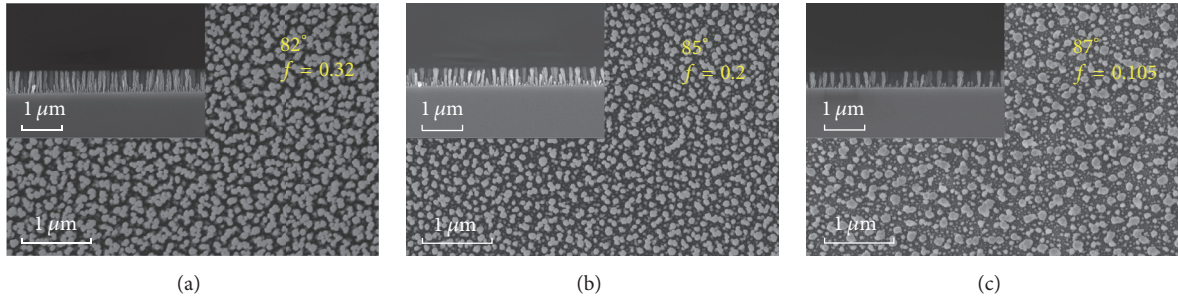


FIGURE 3: Top-view and cross-sectional view SEM images of fabricated GLAD SiO₂ nanorods at different deposition angles of 82°, 85°, and 87°.

however, the f value was not affected by rotation speed and deposition rate. In this research, the GLAD nanorod structure was considered to be a circular pedestal, and the diameter of the circular pedestal used to calculate the f value was obtained by image processing, in which the bright gray area of the top-view SEM image was considered to be the top of the cylinder. The spiral shape of the nanorod structures showed a relatively large solid fraction ratio value, and the values increased with increasing diameter of the spiral shape because the diameter of the spiral shape rather than the diameter of the nanorod was considered to be the diameter of the cylinder during image processing.

The WCAs of the fabricated GLAD nanostructures were measured and compared with the theoretically predicted values using the Cassie-Baxter model. Figure 2 illustrates the experimental and theoretical data of WCAs versus substrate rotation speed. The measured WCAs did not match the theoretical values when the substrate rotation speed was 0.2 rpm because of errors in estimating the diameter of the nanorods with a spiral shape. However, the measured WCAs of the GLAD nanorod samples prepared at a substrate rotation speed of 0.5 to 20 rpm were in a good agreement

with theoretical values. As the f value was saturated when the substrate rotation speed was greater than 5 rpm, the WCA also saturated at about 138° for the samples prepared at a high rotation speed (>5 rpm). Based on this result, a substrate rotation speed of 5 rpm and a deposition rate of 10 Å/s were selected as the optimum processing conditions for the hydrophobic functional GLAD nanostructure because a high rotation speed might cause unexpected problems including vibration and detachment of the substrate during the deposition, and the fast deposition rate was advantageous in terms of fabrication cycle time.

3.2. Effects of Incident Angle on WCA. To examine the effects of incident angle on WCA, GLAD SiO₂ nanorod structures were fabricated with varying oblique angles (82°, 85°, and 87°) and a fixed nanorod height of 500 nm, a deposition rate of 10 Å/s, and a substrate rotation speed of 5 rpm. Figure 3 shows the top-view and cross-sectional SEM images of the GLAD nanostructures fabricated by varying the oblique angle (82°, 85°, and 87°). The data clearly show that that the increasing oblique angle increases the porosity of the surface, which significantly decreased the solid fraction ratio (f).

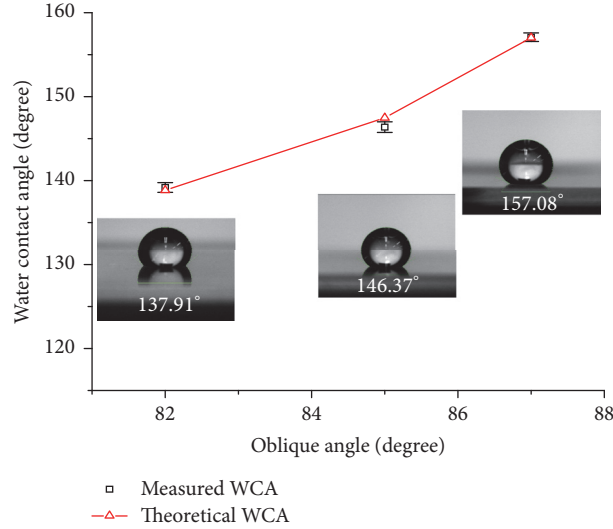


FIGURE 4: Effects of oblique angle on the measured and theoretical WCAs (Cassie-Baxter model) of GLAD nanorod substrates.

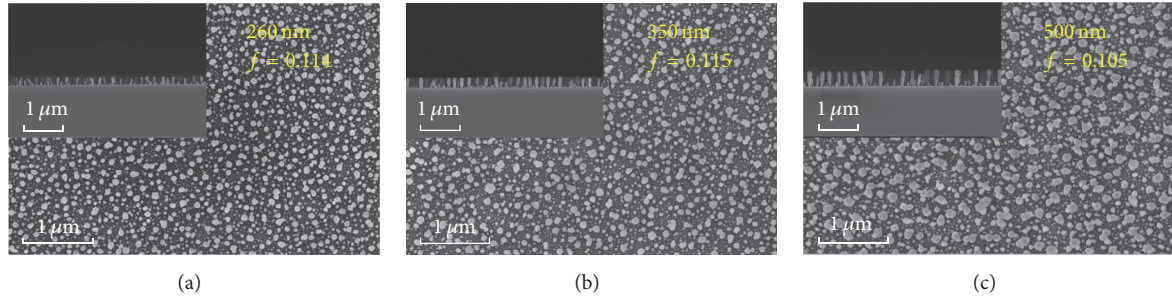


FIGURE 5: Top-view and cross-sectional view SEM images of fabricated GLAD SiO_2 nanorods with different heights of 260, 350, and 500 nm.

Figure 4 illustrates the measured and theoretical values of WCAs. As the oblique angle increased, the solid fraction ratio decreased, and the WCA increased. Since the GLAD SiO_2 nanorod structures used for Figure 3 were fabricated at a high rotation speed (5 rpm), they had a straight vertical shape, and the measured WCAs were in good agreement with the theoretical values. The highest contact angle of 157.08° was observed for columnar nanostructures fabricated at an oblique angle of 87°. Based on this result, the oblique angle of 87° was selected as the optimum processing condition.

3.3. Effects of Height of Nanorods on WCA and Optical Transmittance. To examine the effect of nanorod height on the WCAs, GLAD SiO_2 nanorods with different thicknesses of 260, 350, and 500 nm were fabricated at a 10 Å/s deposition rate, 5 rpm substrate rotation speed, and 87° substrate tilting angle. As shown in Figure 5, the diameter of the nanorods increased as the height of the nanorods increased, and the number of nanorods decreased. Therefore, the solid fraction ratios (f) were almost the same for all fabricated samples with different heights. Figure 6 shows the effects of the height of the nanorod on the measured and theoretical WCAs. As expected, the changes in WCA due to the changes in nanorod height were negligible.

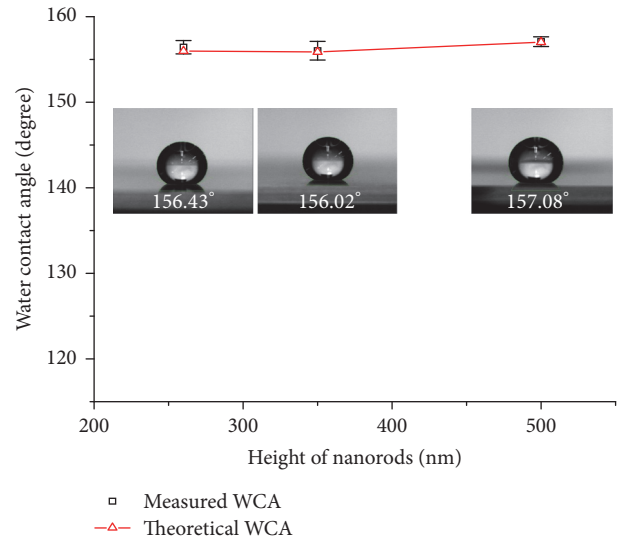


FIGURE 6: Effects of nanorod height on the measured and theoretical WCAs (Cassie-Baxter model) of GLAD nanorod substrates.

To confirm the optimal height of the nanorods for superhydrophobic functional nanostructured surfaces in optical applications, the optical transmission characteristics of the

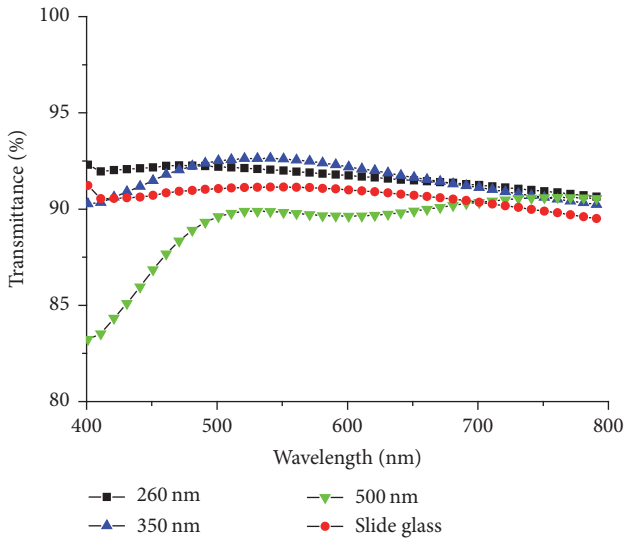


FIGURE 7: Light transmittance of the SiO_2 nanorod films with different thicknesses.

fabricated nanorods with different heights were measured as shown in Figure 7. The GLAD SiO_2 nanorod structures with thicknesses of 260 and 350 nm showed higher transmittance values than the conventional glass slide substrate in the visible range. However, the transmittance of GLAD SiO_2 nanorod structures at a height of 500 nm was lower than that of the glass slide substrate. This can be explained as follows. The taller nanorods had a larger diameter, and the 500 nm tall nanorods scattered the short-wavelength incident light because the transmittance was much lower at short wavelengths (400 to 500 nm). Based on these results, a nanorod height of 260 nm was selected in this study because the short nanorod structure was attractive from a fabrication cost perspective and provided good optical properties. The GLAD SiO_2 nanorod structure with a thickness of 260 nm prepared at a substrate rotation speed of 5 rpm, a deposition rate of 10 Å/s, and an oblique angle of 87° showed a WCA of 156.4° and ~2% higher light transmittance than the glass substrate in the whole visible range.

4. Summary and Conclusions

In this research, superhydrophobic (WCA of ~156°) and antireflection (~2% reduced reflection) functional SiO_2 nanorod structures were fabricated using the simple and inexpensive GLAD process. The GLAD nanorod structures fabricated at high substrate rotation speeds (>5 rpm) were considered circular pedestals, and the measured WCAs of the SiO_2 nanorods with a straight vertical shape well matched the theoretical WCAs from the Cassie-Baxter model. According to the Cassie-Baxter model, the WCA is related to the solid fractional ratio (f). The f value was not affected by the height of the nanorod or the deposition rate when the substrate rotation speed was faster than 5 rpm, but the f value was sensitive to the oblique angle. In this study, an oblique angle of 87° was selected to obtain the maximum water repellency. A substrate rotation speed of 5 rpm was chosen to generate

straight vertical nanorods, and a deposition rate of 10 Å/s was used to minimize fabrication time. A nanorod height of 260 nm was selected to maximize the light transmittance because longer and larger nanorods are better at scattering incident light. Since the GLAD process can also be used for larger substrates, our on-going research is focused on solar cell cover glass production using the proposed GLAD nanorod structure fabrication process.

Conflicts of Interest

The authors declare that they have no conflicts of interest.

Acknowledgments

This research was supported by a grant from the Forensic Research Program of the National Forensic Service (no. NFS2017DNA05).

References

- [1] A. Y. Al-hasan and A. A. Ghoneim, "A new correlation between photovoltaic panel's efficiency and amount of sand dust accumulated on their surface," *International Journal of Sustainable Energy*, vol. 24, no. 4, pp. 187–197, 2005.
- [2] L. K. Verma, M. Sahuja, J. Son et al., "Self-cleaning and antireflective packaging glass for solar modules," *Renewable Energy*, vol. 36, no. 9, pp. 2489–2493, 2011.
- [3] X. Zhao, Q. Zhao, J. Yu, and B. Liu, "Development of multi-functional photoactive self-cleaning glasses," *Journal of Non-Crystalline Solids*, vol. 354, no. 12–13, pp. 1424–1430, 2008.
- [4] K. Han, J. Shin, K. Kim, and H. Lee, "Nanosized structural anti-reflection layer for thin film solar cells," *Japanese Journal of Applied Physics*, vol. 50, no. 2R, p. 020207, 2011.
- [5] T. Nishino, M. Meguro, K. Nakamae, M. Matsushita, and Y. Ueda, "The lowest surface free energy based on -CF₃ alignment," *Langmuir*, vol. 15, no. 13, pp. 4321–4323, 1999.
- [6] B. Bhushan, Y. C. Jung, and K. Koch, "Micro-, nano- and hierarchical structures for superhydrophobicity, self-cleaning and low adhesion," *Philosophical Transactions of the Royal Society A: Mathematical, Physical and Engineering Sciences*, vol. 367, no. 1894, pp. 1631–1672, 2009.
- [7] A. Nakajima, "Design of a Transparent Hydrophobic Coating," *Journal of the Ceramic Society of Japan*, vol. 112, no. 1310, pp. 533–540, 2004.
- [8] T. Aytug, J. T. Simpson, A. R. Lupini et al., "Optically transparent, mechanically durable, nanostructured superhydrophobic surfaces enabled by spinodally phase-separated glass thin films," *Nanotechnology*, vol. 24, no. 31, Article ID 315602, 2013.
- [9] D. Öner and T. J. McCarthy, "Ultrahydrophobic surfaces. Effects of topography length scales on wettability," *Langmuir*, vol. 16, no. 20, pp. 7777–7782, 2000.
- [10] B. Qian and Z. Shen, "Fabrication of superhydrophobic surfaces by dislocation-selective chemical etching on aluminum, copper, and zinc substrates," *Langmuir*, vol. 21, no. 20, pp. 9007–9009, 2005.
- [11] D. K. Sarkar, M. Farzaneh, and R. W. Paynter, "Wetting and superhydrophobic properties of PECVD grown hydrocarbon and fluorinated-hydrocarbon coatings," *Applied Surface Science*, vol. 256, no. 11, pp. 3698–3701, 2010.

- [12] C.-J. Ting, M.-C. Huang, H.-Y. Tsai, C.-P. Chou, and C.-C. Fu, "Low cost fabrication of the large-area anti-reflection films from polymer by nanoimprint/hot-embossing technology," *Nanotechnology*, vol. 19, no. 20, Article ID 205301, 2008.
- [13] D. P. Singh and J. P. Singh, "Controlled growth of standing Ag nanorod arrays on bare Si substrate using glancing angle deposition for self-cleaning applications," *Applied Physics A: Materials Science and Processing*, vol. 114, no. 4, pp. 1189–1193, 2014.
- [14] S. Kumar, P. Goel, D. P. Singh, and J. P. Singh, "Highly sensitive superhydrophobic Ag nanorods array substrates for surface enhanced fluorescence studies," *Applied Physics Letters*, vol. 104, no. 2, Article ID 023107, 2014.
- [15] S. Bruynooghe, D. Tonova, M. Sundermann, T. Koch, and U. Schulz, "Antireflection coatings combining interference multilayers and a nanoporous MgF₂ top layer prepared by glancing angle deposition," *Surface and Coatings Technology*, vol. 267, pp. 40–44, 2015.
- [16] S. Chhajed, M. F. Schubert, J. K. Kim, and E. F. Schubert, "Nanostructured multilayer graded-index antireflection coating for Si solar cells with broadband and omnidirectional characteristics," *Applied Physics Letters*, vol. 93, no. 25, Article ID 251108, 2008.
- [17] S. Kim, W. Zhang, and B. T. Cunningham, "Coupling discrete metal nanoparticles to photonic crystal surface resonant modes and application to Raman spectroscopy," *Optics Express*, vol. 18, no. 5, pp. 4300–4309, 2010.
- [18] Y.-P. Zhao, D.-X. Ye, G.-C. Wang, and T.-M. Lu, "Novel nano-column and nano-flower arrays by glancing angle deposition," *Nano Letters*, vol. 2, no. 4, pp. 351–354, 2002.
- [19] Y.-A. Han, J. Ju, Y. Yoon, and S.-M. Kim, "Fabrication of cost-effective surface enhanced raman spectroscopy substrate using glancing angle deposition for the detection of urea in body fluid," *Journal of Nanoscience and Nanotechnology*, vol. 14, no. 5, pp. 3797–3799, 2014.
- [20] M. Suzuki, "Practical applications of thin films nanostructured by shadowing growth," *Journal of Nanophotonics*, vol. 7, no. 1, Article ID 12150SSP, pp. 073598-073598, 2013.
- [21] R. N. Wenzel, "Surface roughness and contact angle," *The Journal of Physical Chemistry*, vol. 53, no. 9, pp. 1466–1467, 1949.
- [22] A. B. D. Cassie and S. Baxter, "Wettability of porous surfaces," *Transactions of the Faraday Society*, vol. 40, pp. 546–551, 1944.

Research Article

Viscosity and Morphology Modification of Length Sorted Single-Walled Carbon Nanotubes in PIB Matrices

Hanxiao Huang,¹ Bohao Li,¹ Clayton E. Simien,² and Daneesh O. Simien¹

¹*Department of Materials Science and Engineering, Engineering School, University of Alabama at Birmingham, Birmingham, AL, USA*

²*Department of Physics, College of Arts and Sciences, University of Alabama at Birmingham, Birmingham, AL, USA*

Correspondence should be addressed to Daneesh O. Simien; dsimien@uab.edu

Received 28 April 2017; Revised 12 July 2017; Accepted 14 August 2017; Published 18 September 2017

Academic Editor: Xiaowei He

Copyright © 2017 Hanxiao Huang et al. This is an open access article distributed under the Creative Commons Attribution License, which permits unrestricted use, distribution, and reproduction in any medium, provided the original work is properly cited.

This work evaluates the effectiveness of nanoscale particulates in producing non-Einstein-like responses in polymer matrices, to reduce their negative effects in low shear rate processing. This is of value to material processing applications which encompass extrusion, flow into cold mold, and generalized processing of nanocomposites. Through control and understanding of the structure processing relationships entailed through nanoscale additive materials, we begin to manage dispersion characteristics for more reliable and defect-free product development. In pursuit of identifying system characteristics that produce non-Einstein-like responses we isolate and characterize homogenous fractions of single-walled carbon nanotubes (SWNTs) with singular lengths. This enables the definition of a well-defined nanoscale particulate phase, within the polymer matrices. The effect of nanotube length and weight fraction on the polyisobutylene (PIB) matrices was evaluated with thermal and rheological testing. Our findings show that the viscosity of the produced nanocomposite systems has a length dependence and does not demonstrate the expected monotonous increases in the viscosity with an increase in weight fraction of nanotube additive within the matrix, demonstrating a non-Einstein-like viscosity response. Furthermore, we demonstrate length dependent crystallization in the studied systems, as an intermediate length nanotube initiates crystallization of polyisobutylene (PIB) affecting viscosity and mechanical properties.

1. Introduction

Single-walled carbon nanotubes (SWNTs) are an example of the more recently discovered nanoscale materials with unique structure and properties. Composed of single carbon atoms in a rod-like cylindrical pattern, it has a high degree of structural perfection [1]. Furthermore, the dominating covalent bonded structure provides extremely high modulus and strength, even comparable to that of steel, but only at a sixth of its density. Advantages in mechanical strength and thermal and electrical conductivity make carbon nanotubes ideal additives in polymer nanocomposites [2–4]. However, there are several processing concerns in generating nanoscale composites, such as the dispersion of the nanoscale phase within the polymer matrix and the initiation of large increases in viscosity with the addition of nanoscale additives and poor polymer-nanotube interface, all of which ultimately contribute to the formation of defects which do not facilitate the

expected strengthening in mechanical or electrical properties which should be achieved.

In processing SWNT-polymer nanocomposites, viscosity increase can be a primary challenge. It affects flow rates in different temperature zones at different shear rates. It may affect the flow rates and nanoparticle distributions achieved in printing nanoscale inks or defect formation in flow into cold molds for nanocomposite product development. In general, Einstein predicts that the viscosity of Brownian particles is solely a function of its volume in the suspending liquid [5]. Therefore the inclusion of a particle in a suspending phase should increase the viscosity of the system. However it has been shown that nanoscale inclusions may demonstrate non-Einstein-like behavior where a decrease or no change in the viscosity of overall system is observed. This atypical type of system behavior occurs when the nanoparticles provide confinement and surface effects and cause conformational changes to the macromolecules of the polymer system

present. Uniformly dispersed nanoparticles reduce the entanglement of polymer chains, while the blend viscosity reduces with the free volume associated with the nanoscale filler or particles, due to their rigid and stiff characteristics rendering non-Einstein-like behavior. The prerequisite of this behavior is that the nanoscale filler must have comparable scale to the radius of gyration of polymer, at least, in one dimension, for example, length, width, or diameter. The radius of gyration, R_g , is defined as the distance of a collection of atoms from their common center of gravity and influenced by the molecular weight, stiffness, and viscosity of the polymer [5–7].

In previous studies by Mackay et al., non-Einstein-like behavior is demonstrated where spherical nanoparticles (radius of 3 nm–5 nm) synthesized by crosslinking polystyrene (PS) were added to a polystyrene matrix which had R_g of 7.5–15 nm. These systems demonstrated the atypical non-Einstein-like responses which can be observed in nanoparticulate systems. In these systems the spherical particles increased the free volume of the system and also reduced the entanglement of the matrix. The composite displayed a reduction in the low shear rate viscosity with addition of up to 10 wt.% nanoparticle, later showing the expected increases in viscosity at higher loadings associated with the increased stiffness attributed to the present nanoparticles [5]. Jain et al. [8] studied the viscosity reduction from silica particles in polypropylene (PP) matrices, in which they attributed the atypical viscosity responses to the selective physisorption of long macromolecular chains onto the surface of silica particles due to similar surface chemical characteristics. In addition, Xie et al. [9] found a viscosity decrease in PVC/CaCO₃ systems due to a ball bearing effect, while Cho and Paul [10] attributed viscosity reduction in their systems to the molecular degradation and slip at wall for nylon-clay systems. In each of these works it is observed that atypical viscosity can be achieved depending on the particulate morphology, treatment, or interaction dynamics. In our systems, we observe effects that may be more narrowed to interactions such as steric hindrance and a reduction of polymer entanglement. In this process, uniformly dispersed nanoparticles reduce the entanglement of polymer chains while the blend viscosity reduces with the free volume associated with the nanoscale filler or particles, due to the rigid and stiff characteristics of the length sorted single-walled carbon nanotubes (SWNTs) rendering non-Einstein-like behavior. Roberts et al. [11] found that clusters of silica caused viscosity reduction to the linear poly(dimethylsiloxane) when the nanoparticles were less than 0.7 nm in size, which facilitated plasticizing effects. Tuteja et al. used PS nanoparticles and studied its viscosity reduction effect, at different molecular weights of the linear PS matrix [12]. They concluded that, to induce non-Einstein-like viscosity behavior, the polymer must be entangled, and the separation distance between nanoparticles should be comparable to the polymer radius of gyration. They also found that fullerenes resulted in a similar viscosity reduction at a mass fraction of 0.02 [13]. Furthermore, a more quantitative study was conducted by Schmidt et al. [14], in which they defined a critical nanoparticle-to-polymer R_g ratio to induce the transition from plasticization (reduced viscosity) to reinforcement (increased viscosity). In their

work blending polysilicate with poly(dimethylsiloxane), the critical ratio was found to be 0.18, at 298 K and a nanoparticle weight fraction of 0.17. Further research also demonstrates that carbon nanotubes can result in steric hindrance and viscosity reduction. Petriccione et al. found that the viscosity of bifunctional epoxy-ammine systems showed a reduction when the weight fraction of multiwalled carbon nanotubes increased from 0.096 to 0.190 wt.% [15]. Similarly, Zhang et al. found that, at 0.1–0.2 wt.% fraction, SWNTs resulted in a significant viscosity reduction in polyethylene (PE) systems, which then showed viscosity increases again at 1 wt.% due to the formation of nanotube networks [16].

In this publication, we explore non-Einstein-like viscosity behavior in single-walled carbon nanotube (SWNT) composite systems by controlling the weight fraction and the length and diameter of nanotube fractions used as additives to PIB matrices. Our goal is to ensure that these SWNT parameters are comparable to or smaller than the radius of gyration of the PIB molecules in the matrices, with the goal of optimizing our understanding of viscosity control in these nanoscale systems. In evaluating our SWNT-polymer nanocomposite systems, we also find evidence of nanotube induced polymer crystallization. It is well known that nanotubes are one of the most effective nucleation agents for the heterogeneous crystallization of polymers, particularly for crystalline and semicrystalline polymers [17–20]. Li et al. demonstrated, for example, that selected polyethylene (PE) oligomers at a low molecular weight, 800 g/mol, demonstrated evidence of crystallization at nanotube sites [17].

In our work, the as-received single-walled carbon nanotubes (SWNTs) were separated by length using density gradient ultracentrifugation [21]. Polyisobutylene (PIB) was selected as the incorporating polymer matrix, and homogeneous fractions of SWNTs of varying lengths and weight fractions were isolated and blended with the PIB. The effects of, both, nanotube length and weight fraction were studied on the viscosity, thermal behavior, and crystallization of the PIB matrix. We believe this study will broaden the understanding of the fabrication and control of SWNT-polymer nanocomposites and enhance our understanding of nanoparticle usage as additives for thermal applications such as in extending the life of engine oils, for which PIB is sometimes used as a base oil.

2. Results

2.1. UV-Vis-NIR Spectroscopy. Ultraviolet-visible-near infrared (UV-Vis-NIR) spectroscopy was first conducted on the as-received nanotubes which were presorted via ultracentrifugation to remove excess carbon and catalytic materials, shown in Figure 1. The chiralities (n, m) of the presorted nanotube solution were identified. Subsequently, further separation to isolate homogenous length fractions of SWNTs by layers in a density gradient was performed. A UV-Vis-NIR analysis was preformed and the spectra were analyzed for each length separated layer retrieved after the separation process. A normalization was applied at 775 nm, where no π -plasmon transitions are located, to identify variations which occur in the comparative intensity of

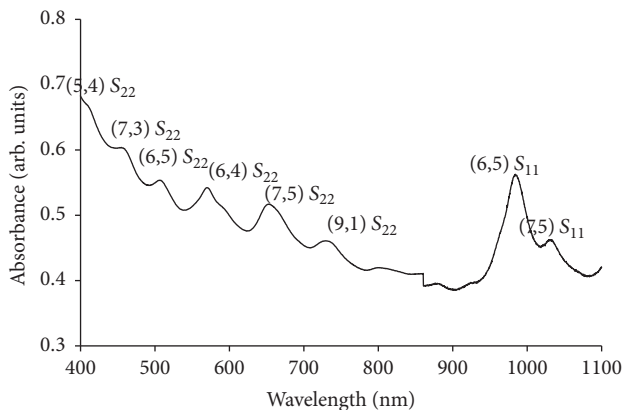


FIGURE 1: UV-Vis spectroscopy curve of presorted nanotubes sample.

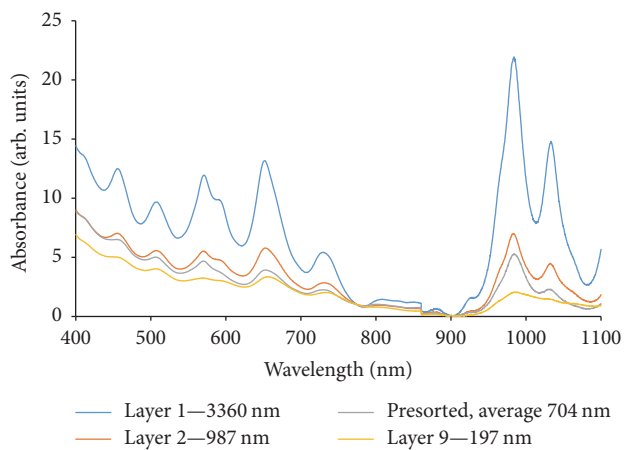


FIGURE 2: Normalized UV-Vis spectroscopy curves of three selected length sorted SWNT samples.

homogeneous length fractions; the result is shown in Figure 2. The length of the SWNTs was estimated by the equation below: $L(\text{nm}) = (A_{984\text{ nm}}/A_{775\text{ nm}} - 1) * 160.4 \text{ nm}$ [21]. The normalized peak ratio and calculated nanotube lengths are summarized in Table 1. According to Table 1, the length of nanotube decreases as depth of separation layer increases.

2.2. Scanning Electron Microscopy. After length separation, nanotube solutions of two lengths 3360 nm and 987 nm were selected for study. The presorted nanotubes of mixed lengths (with an average length parameter of 704 nm) were selected as the control group. According to Figures 3(a) and 3(b), a considerable length difference occurs and can be isolated after sorting. This length difference is consistent with calculations from the UV-Vis-NIR analysis.

2.3. Differential Scanning Calorimetry. The glass transition temperatures (T_g) of all samples were recorded using Differential Scanning Calorimetry (DSC). As shown in Table 2, the pristine PIB has T_g at -69.59°C . As the weight fraction of the nanotubes present in the composite increases to 0.02

and 0.05 wt.%, T_g is reduced by approximately 7.35°C and 5.82°C , respectively, whereas above 0.1 wt.% much smaller changes in the T_g are observed, which is an atypical response. The glass transition of a polymer will generally be affected by its environment when the chain length is within several nanometers of the secondary phase [22]. The larger changes in T_g experienced by the addition of less than 0.08 wt.% nanoparticle may be attributed to the nanoparticles being near their percolation threshold and the initial onset of an interconnected nanotube network, which generated a “nanoscale-effect” which is isolated to that critical concentration regime [23].

The heat flow curves of all length sorted nanotubes at three weight fractions are shown in Figures 4, 5, and 6. Among all the lengths, nanotubes with lengths 638, 384, and 197 nm result in observable melting peaks and the area of the peaks was summarized in Table 3. According to Table 3, 638 nm length samples display the highest peak area indicating the highest crystallinity degree. In contrast, 384 and 197 nm samples display a reduced crystallinity degree while the 3360 and 987 nm samples remained highly amorphous. As weight fraction of nanotube increases, the crystallinity degree decreased among all lengths evaluated.

In observing the morphology of the SWNT-PIB composites, there is a dramatic difference in the samples depending on the length of the incorporated SWNT phase. The presorted samples avg., length 704 nm, 987 nm, and 3360 nm demonstrate an amorphous “gel-like” structure, while the shorter length SWNT composites of 638 nm and below demonstrate a crystalline structure. The longer length SWNT samples are likely providing more steric hindrance and network structures, while the shorter length SWNTs are serving as nucleation sites for PIB crystallization.

2.4. Rheological Testing. Dynamic viscosities of presorted nanotubes-PIB mixtures, at multiple weight fractions, are shown in Figure 7, and the dynamic viscosity at frequency 0.1 rad/s was recorded in Table 4 as the final viscosity value for further discussion. According to Table 4, dynamic viscosity increases dramatically from 1 to 5 wt.%. However, samples with nanotube weight fractions not higher than 0.05 wt.% have dynamic viscosity smaller than that of the virgin PIB. This 0.02 wt.% sample represents a sample which is close to the critical percolation concentration of the nanotubes incorporated and is the first indicator of possible non-Einstein-like behavior among these nanocomposite systems.

The dynamic viscosity of nanocomposites made from select isolated fraction of homogeneous single length nanotubes was shown in Figures 8, 9, and 10. Also, the dynamic viscosity of each sample at 0.1 wt.% was recorded in Table 5 for further discussion. According to Table 5, the dynamic viscosity is the highest among intermediate length 638 nm and shorter lengths 384 and 197 nm nanotube composites. In contrast, the 3360 and 987 nm length SWNT samples have smaller dynamic viscosity while those of presorted nanotubes (mixed lengths with avg. length of 704 nm) have the smallest value. Meanwhile, as nanotube weight fraction increases from 0.1 to 0.25 and further to 0.5 wt.%, the dynamic viscosity of all

TABLE 1: Normalized peak ratio and calculated length and concentration of nanotube.

Layer after length separation	$A_{984\text{ nm}}/A_{775\text{ nm}}$ after normalization	Calculated length [nm]	$A_{775\text{ nm}}$ before normalization	Calculated concentration [mg/ml]
1st	21.97	3360	0.587	0.411
2nd	14.98	2267	0.384	0.269
3rd	7.00	987	0.250	0.175
4th	4.82	638	0.100	0.070
5th	3.24	384	0.207	0.145
6th	2.58	279	0.182	0.127
7th	2.39	248	0.191	0.134
8th	2.23	223	0.248	0.174
9th	2.07	197	0.221	0.155
<i>Presorted nanotube</i>	5.23	704	0.424	0.297

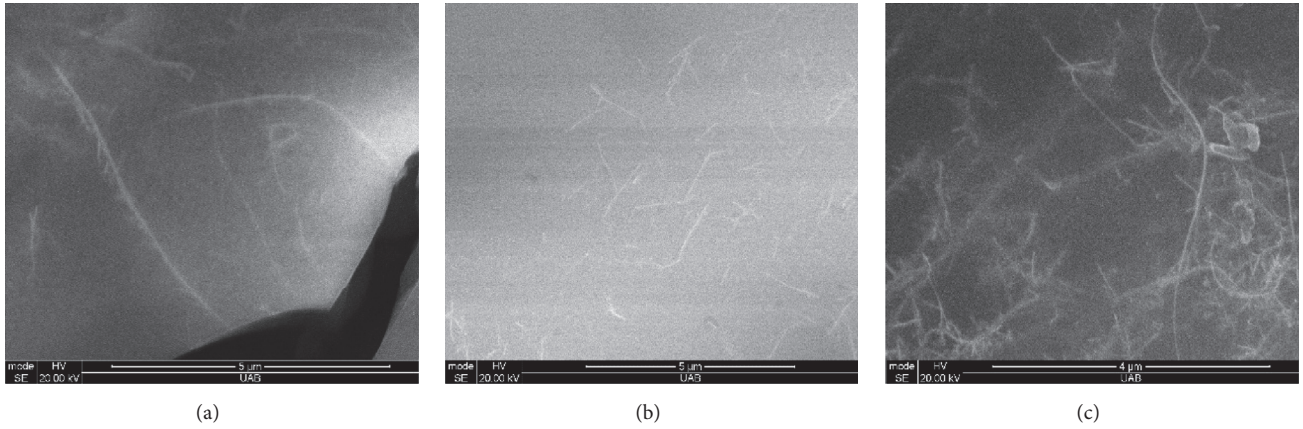


FIGURE 3: SEM images for SWNT fractions of lengths (a) 3360 nm and (b) 987 nm and (c) presorted sample (avg. 704 nm).

TABLE 2: Effect of nanotube weight fraction on glass transition temperatures.

SWNT weight fraction [wt.%]	T_g [°C]
0	-69.59
0.02	-76.94
0.05	-75.41
0.1	-66.30
0.25	-65.45
0.5	-66.18
1	-65.42
5	-66.44

samples increased, but more significantly in 3360 and 987 nm samples.

In isolating the length of the nanotube in singular fractions and exploring the resulting structure-property relationships, we see that very different properties can be obtained, for example, in the crystallization behavior of the matrix. The presorted samples having an average length of c.a. 704 nm but containing both long and short length nanotubes

TABLE 3: Melting peak area of SWNT/PIB at varying lengths and weight fractions.

Melting peak area	0.1 wt.%	0.25 wt.%	0.5 wt.%
638 nm	111.60	75.87	67.08
384 nm	85.21	46.79	21.01
197 nm	66.58	34.40	17.53

demonstrate such behavior. The longer length nanotubes, present in this starting sample, result in a retardation of crystallization behavior in the PIB matrix, which is shown in the data for the (mixed length) presorted nanotubes. This behavior is different from that which is observed when we evaluate a SWNT sample with homogeneous length of 638 nm, for example, which demonstrates a different crystallization response.

3. Discussion

3.1. *UV-Vis-NIR Spectroscopy.* In order to generate isolated lengths species from the as-received fractions an ultracentrifuge technique is used on the nanotubes which have been

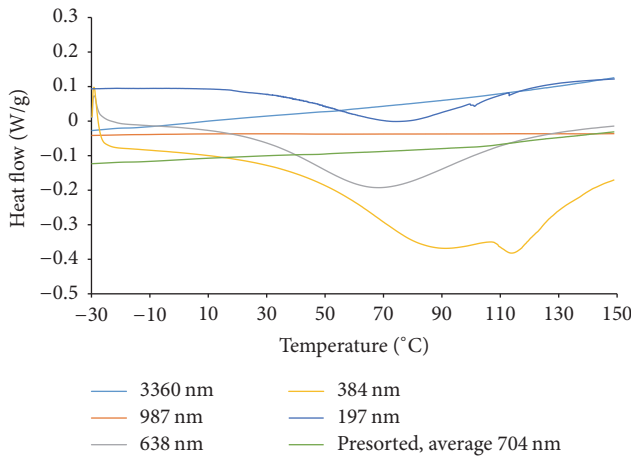


FIGURE 4: Heat flow of length sorted nanotube-PIB composites, 0.1 wt.%.

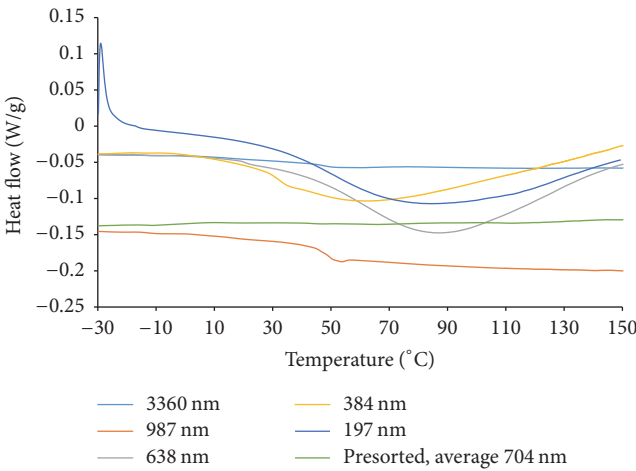


FIGURE 5: Heat flow of length sorted nanotube-PIB composites, 0.25 wt.%.

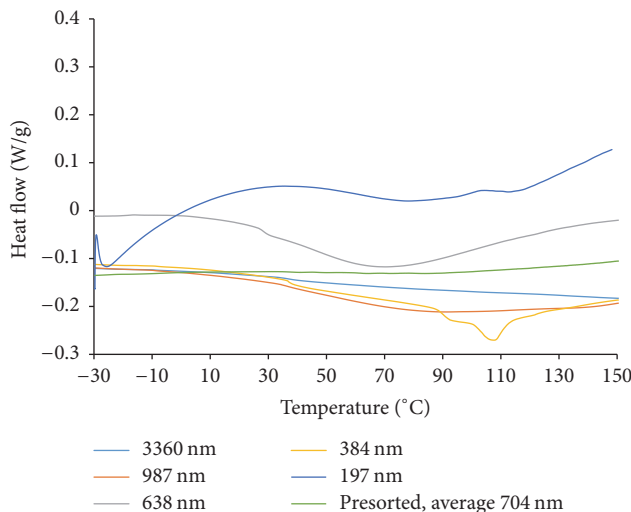


FIGURE 6: Heat flow of length sorted nanotube-PIB composites, 0.5 wt.%.

TABLE 4: Viscosity value of presorted nanotube mixtures at various weight fractions.

Presorted SWNT weight fraction [wt.%]	Viscosity [Pa·s]
0	23,290
0.02	19,910
0.05	20,510
0.1	43,120
0.25	59,860
0.5	88,690
1	104,800
5	784,900

TABLE 5: Viscosity values of length sorted nanotube mixtures at varying lengths and weight fractions at 0.1 rad/s.

Dynamic viscosity [Pa·s]	0.1 wt.%	0.25 wt.%	0.5 wt.%
3360 nm	171,500	575,200	1,124,000
987 nm	107,400	176,000	381,000
638 nm	811,000	1,092,000	1,639,000
384 nm	646,900	821,700	1,050,000
197 nm	492,100	522,800	589,000
Presorted, <i>mixed length</i> , average 704 nm	43,120	59,860	88,690
PIB			23,290

suspended in a density gradient fluid. This technique was initially proposed by Fagan et al. who successfully separated nanotubes by length [21]. In this process, the difference in the buoyancy and frictional force between nanotubes of varying lengths is exploited in order to achieve separation in a transient regime. According to Fagan et al. [21, 24], nanotubes with larger length have a lower frictional coefficient and tend to travel with less opposition to the centrifugal acceleration. Thus, longer length nanotube accumulates near the top of the centrifuge tube, when suspended in a density gradient fluid and subjected to an accelerating field, while the shorter ones tend to sediment deeper. Multiple lengths of nanotube were isolated using this method which will be used for further experiments including 3360, 987, 638, 384, and 197 nm.

3.2. Scanning Electron Microscopy. According to Figures 3(a) and 3(b), the observed length is consistent with calculation from UV-Vis-NIR analysis. As introduced above, the nanoscale filler has the potential to cause conformational change and modified rheological behavior of the polymer to which it is added. On one hand, the nanoscale filler reduces the entanglement of polymer. On the other hand, nanoscale particles are highly rigid and stiff. In other words, they are not deformable. Thus, they add free volume themselves. The prerequisite for conformational change is that the nanoscale filler must have comparable size with the radius of gyration (R_g) of polymer. More specifically, at least one dimension should be in the same order of size with R_g , including length and diameter. Fetters et al. [7] developed a calculation of

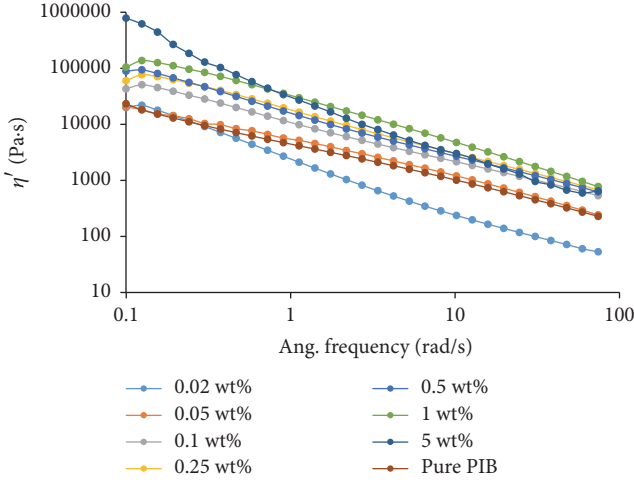


FIGURE 7: Viscosity curve of presorted nanotube mixtures (the same average length 704 nm) at various weight fractions.

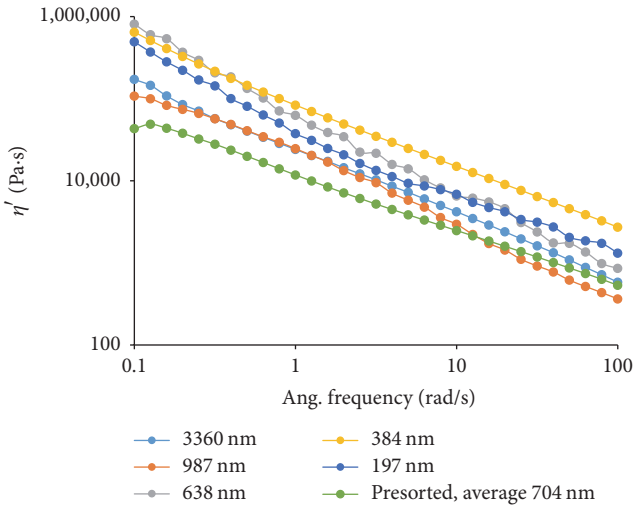


FIGURE 8: Dynamic viscosity of nanotube at various lengths (0.1 wt.% loading of SWNT, at data point 0.1 rad/s).

radius of gyration for various polymers including polybutadiene, polyisoprene, polystyrene, and polyisobutylene. Data for PIB was collected in theta solvents benzene and isoamyl isovalerate at room temperature. The extent of distortion of polymer chain can vary depending on its molecular weight range and solvent environment. Thus, various relationships are generated depending on these variables.

When the radius of gyration is collected in theta solvents isoamyl isovalerate, the applicable molecular weight range is $3.91 * 10^5 < M_n < 4.7 * 10^6$, and the radius of gyration is

$$R_g = 2.62 * 10^{-2} * M_n^{0.511}. \quad (1)$$

If a broader applicable range of molecular weight is required, cyclohexane is considered. In the molecular weight range

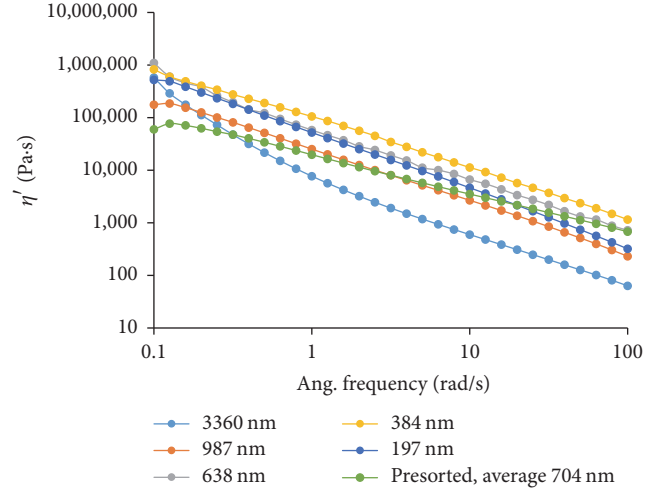


FIGURE 9: Dynamic viscosity of nanotube at various lengths (0.25 wt.% loading of SWNT, at data point 0.1 rad/s).

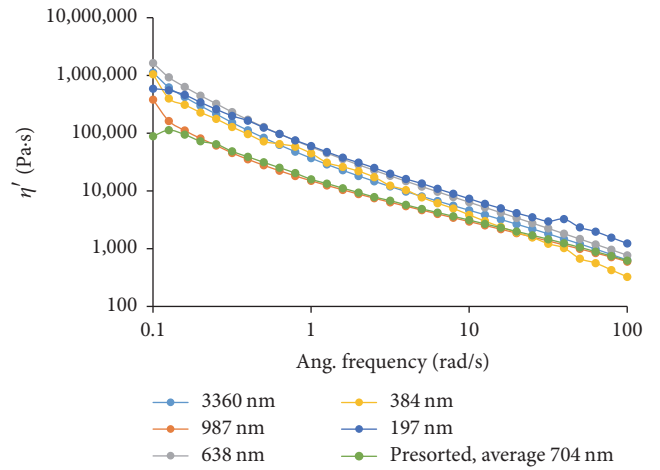


FIGURE 10: Dynamic viscosity of nanotube at various lengths (0.5 wt.% loading of SWNT, at data point 0.1 rad/s).

$1.6 * 10^5 < M^n < 1.41 * 10^7$, radius of gyration can be written as

$$R_g = 1.37 * 10^{-2} * M^{0.595}. \quad (2)$$

See [7].

In this work, the as-received PIB has a molecular weight 200,000 g/mol. Based on the equations above, its radius of gyration is 19.54 nm. To measure the diameter of nanotube bundles, ImageJ Software was utilized to analyze the SEM pictures. The diameter at various positions was measured and compared with the scale bar for calculation. The obtained diameters range from 18.83 to 29.16 nm. R_g of PIB is not only comparable to this size, but also stays within this range. Thus, the perquisite for conformational change was completely satisfied.

3.3. Differential Scanning Calorimetry. T_g shift marks the change in polymer conformation, including extent of entanglement and packing density. More specifically, the shift towards lower temperature refers to a loose arrangement of macromolecules. According to Table 2, a 6–7°C T_g reduction occurs in the 0.02 and 0.05 wt.% samples. As discussed above, nanotube bundles intertwined with macromolecules of PIB, reducing its entanglement. Meanwhile, the rigid-rod-like nanotube brings free volume itself, which further reduces the packing density of polymer. At low nanotube loadings, the combined effect of these two factors leads to a negative T_g shift.

At higher loadings, difficulty arises in the isolation and dispersion of nanotubes in the PIB matrix. A reasonable assertion could be made that this is a regime within which there is a saturation of the number of nanotube bundles which have a size comparable with R_g of the polymer. Beyond 5 wt.% nanoparticulate filler, the likely expression of rheological percolation dominates the structure-property relationships and we begin to see evidence of agglomerations, reducing any effects that would contribute to non-Einstein-like behavior.

It is well known that carbon nanotube can be a nucleation site that initiates polymer crystallization. The effect of nanotube length in this process, however, has hardly been studied. Li used polyethylene (PE) with a molecular weight 800 g/mol [17]. PE is a highly crystalline polymer and can crystallize without nucleation agents. In Li's case, its molecular weight is also extremely low. Thus, the crystallization occurs readily when nanotubes are included. In our case, however, the PIB has a significantly large molecular weight at 200,000 g/mol, and it also has a methyl side group. Thus, crystallization could be more difficult. As discussed above, PIB is highly amorphous. Interestingly, the nanotubes of longer length fail to initiate crystallization, while short ones do. There could be multiple reasons for this difference. On one hand, the nanotubes have a large free volume, being highly rigid-rod-like and poorly deformable, and also the attachment of polymer is limited to steric hindrance and Van der Waals effects. Thus, the effect of free volume and the difficulty of interactions of the polymer could be increased with nanotube size and length. On the other hand, the formation of nanotube networks is easily facilitated and dense at longer lengths. The overlap and mingled arrangement of long length nanotube also provided poor surface area and space for polymer nucleation and lamellar growth.

Another interesting finding is that, among the various lengths of nanotube tested, the 638 nm length samples result in a larger degree of crystallization than the shorter ones. It seems that a minimum length of nanotube is required for optimum nucleation initiation. According to Binsbergen, the nucleation theory of Hoffman and Lauritzen also applies to polymer [25]. Nucleating agents should at least have a size comparable to the thickness of the lamella, to initiate heterogeneous nucleation of the polymer. Thus, the nanotube at an average length of 197 nm fails to achieve the full potential for nucleation. Furthermore, according to Table 1, the presorted, mixed length sample has the highest concentration of longer length SWNT comparatively, which stops crystallization as discussed before. Thus, although its average length is close

to 638 nm, a contrasting difference in crystallization behavior exists.

Finally, the reduced crystallinity degree at higher weight fractions, 0.25 and 0.5 wt.%, is highly possibly due to an increasing of nanotube agglomeration and reduced concentration of nucleation sites of favorable size. However, the crystallization of PIB is not desirable for viscosity control, which will be discussed in the following section.

3.4. Rheological Testing. According to Table 4, the dynamic viscosity of PIB mixed with presorted nanotubes does not increase monotonously with weight fractions, which indicates the effect of conformational change and the occurrence of non-Einstein viscosity behavior. The 0.02 and 0.05 wt.% samples showed reduced viscosity compared to the pure PIB, for multiple reasons. On the one hand, the rigid-rod-like nanotube introduces free volume and decreases the packing density of PIB. On the other hand, it reduces the entanglement of polymer and further decreases viscosity. This conformational change was verified by T_g testing recorded in Table 2, where the 0.02 and 0.05 wt% samples had a T_g reduction as high as 6–7°C. However, at high weight fractions of nanotube filler, the viscosity increases and finally becomes larger than that of PIB due to the saturated solubility of isolated nanotubes and the formation of large clustering. Thus, the weight fraction of nanotube should be carefully controlled for the purpose of viscosity modification, even in unsorted, unmodified SWNT additive, composites, and mixtures.

At a weight fraction of 0.1 wt.%, the mixture with 638 nm, 384 nm, and 197 nm length nanotubes, as discussed above, showed significant crystallization. They also showed the highest viscosity due to the contribution of the crystalline region, which is still not completely melted at the testing temperature. Furthermore, the longer length nanotube samples still result in viscosity one order larger than the pristine presorted nanotube samples. Network structure is more easily formed in longer length nanotubes, which increases the viscosity. The longer length nanotubes therefore cause more resistance to rheological flow due to its rigid-rod-like morphology and their onset of network formations. Comparatively, as the weight fraction increases from 0.1 to 0.25 wt.%, the dynamic viscosity of all samples shows an increase. In particular, the viscosity increases significantly for the longer length SWNT fractions of 3360 and 987 nm, which can be attributed to lower critical percolation concentrations, for nanotube network formations, with higher frequency throughout the polymer matrix. Finally, crystallization was suppressed in the presorted samples that are rich in long length SWNTs. This could result from the shorter average length SWNTs present, compared to the 3360 and 987 nm samples, which would render reduced steric hindrance effects and shift the percolations concentration to higher values for network formation. The presorted, mixed length samples currently display the lowest viscosity profile of all the samples studied in this work.

4. Materials and Methods

4.1. Apparatus and Reagents. SWNTs were purchased from Southwest Nanotechnology, CoMoCAT type of synthesis,

95% purity. Sodium Deoxycholate Detergent (DOC) and Dichloromethane (DCM) were purchased from Fisher Scientific. The OptiPrep density gradient solution (60 wt% iodixanol) was purchased from Sigma Aldrich. A Misounic Ultrasound liquid processer, Qsonica LLC, was used for ultrasound treatment and mixing. A Sorvall Ultracentrifuge (Thermo Fisher) was used for density centrifugation. A PerkinElmer UV-Vis-NIR spectrometer was utilized to study the length of each layer after separation. Scanning Electron Microscopy (SEM, Quanta FEG 650) was used to observe morphology of length sorted nanotube samples. An AFM (ezAFM, NANOMAGNETIC Instruments) was utilized to study the topography and amplitude of nanotube bundles. A DSC Q 100 (TA Instruments) was used to study the glass transition and crystalline behavior of nanotube polymer mixture. An Ares 2000 Rheometer (TA Instruments) was used to measure the dynamic viscosity. Finally, Fourier transform infrared spectroscopy (FTIR, NICOLET 4700 FT-IR, Thermo Electron Corporation) was used to further study the crystallinity degree quantitatively.

4.2. Length Separation of SWNT. 900 mg of SWNT was blended with 900 ml 2 wt.% DOC surfactant solution. The as-formed 1 mg/ml nanotube solution was treated with tip ultrasound mixing at amplitude 40, power 14 W, and 1 h in an ice bath. The solution was then directly treated with ultracentrifugation at 5°C, 30 mins at a rotation speed 20300 rpm. This step removes large bundles formed during ultrasound treatment, rendering the presorted nanotube fractions. Then the density gradient was made by mixing iodixanol solution and deionized water in various ratios. The 13 ml centrifuge tube was used, and from top to bottom the composition of density gradient was 6 ml-18%, 4 ml-25%, and 2 ml-30% iodixanol solution. The bottom solution was made by mixing OptiPrep with SWNT aqueous solution directly, instead of DI water. Then the SWNT-density gradient solution was treated with ultracentrifugation at 5°C, at 39600 rpm, and for 12 hrs. The final product was separated by hand pipetting removing 0.75 ml per layer.

4.3. Fabrication of SWNT-PIB Nanocomposites. 500 mg of virgin high MW PIB was weighted and mixed with 30 ml of Dichloromethane. Ultrasound treatment was applied to the mixture at an amplitude 70, at power 14 W, and for 2 hrs. The nanotube was mixed with PIB at varying weight fractions and lengths separately. First, aqueous solution of presorted nanotube was dropped into the mixture at various weight fractions including 0.05, 0.1, 0.25, 0.5, 1, and 5 wt.%. Then ultrasound treatment was applied for another one hour at the same amplitude. The final mixture was dried vacuum oven overnight. The same treatment was repeated to as-received PIB as the control group. Later PIB was further mixed with nanotubes after length sorting. The selected lengths include 3360 nm, 987 nm, 638 nm, 384 nm, and 197 nm. They were mixed with PIB using the same technique and posttreatment, but all at a weight fraction of 0.1 wt.%. Two repeated groups of test were conducted to nanotube of the same five lengths, but at weight fraction 0.25 and 0.5 wt.%.

4.4. Characterizations. UV-Vis-NIR spectroscopy was utilized to study the length of each layer after separation. The test used wavelength from 400 to 1100 nm. The curve was normalized at 775 nm where amplitude was reset to 1. Later the absorbance at 984 nm was recorded. The equation below was used to calculate the final length.

$$L \text{ (nm)} = \left(\frac{A_{984 \text{ nm}}}{A_{775 \text{ nm}}} - 1 \right) * 160.4 \text{ nm.} \quad (3)$$

See [21].

In order to determine the concentration of SWNT aqueous solution, 50 ml of nanotube solution was tested by UV-Vis-NIR spectroscopy, and the absorbance at 775 nm was recorded. Then it was deposited on the filter paper by vacuum filtration. The weight difference of filter before and after inclusion of nanotube was recorded as the overall weight of SWNT. Since the concentration of CoMoCAT SWNT is directly proportional to the absorbance at 775 nm, the concentration of any other nanotube solution would be calculated using the standard sample measured above.

Scanning Electron Microscopy (SEM) was performed at a Secondary Electron (SE) mode with spot size 4.0 and accelerating voltage 20 kV. The magnification ranges from 50 to 100 k times. The ImageJ Software was applied to estimate the diameter of nanotube bundles with reference to scale bar. An AR 2000 Rheometer was utilized for viscosity measurement. The frequency sweep was conducted to all samples at 160°C, from 0.1 to 100 rad/s. The constant parameter was set as 0.5% strain. Five sweeps at each frequency were automatically conducted by the rheometer and averaged as the final data point. The thermal properties were studied by Differential Scanning Calorimetry (DSC) Q 100, under indium and zinc calibration standard. Uniformly weighted samples of 5–20 mg were sealed within perforated aluminum pans and went through a temperature ramp mode from –80 to 440°C. The ramp rate was 5°C/min under a nitrogen atmosphere.

5. Conclusions

In this work, the length separation of SWNTs was conducted and analyzed. The effect of nanotube length and weight fraction on PIB was studied. The result shows that nanotube facilitates conformational changes to the polymer and causes non-Einstein-like viscosity reduction at lower weight fractions. The shorter length nanotubes of 638 nm proved to be ideal nucleation agents to initiate crystallization of PIB, while longer length nanotubes do not show the same initiation responses. The longer length nanotubes form networks easily and dramatically increase viscosity. We believe this work will broaden our understanding of SWNT-polymer nanocomposites, particularly in the control of nanotube length and weight fractions to achieve optimum properties.

Conflicts of Interest

The authors declare no conflicts of interest.

Authors' Contributions

Daneesh O. Simien is the laboratory's principal investigator. Daneesh O. Simien, Clayton E. Simien, and Hanxiao Huang conceived and designed the experiments. Hanxiao Huang performed the experiments and analyzed the data. Bohao Li conducted research in length separation of carbon nanotubes.

Acknowledgments

The authors acknowledge financial support from the UAB faculty development grant program (FDGP). They also sincerely appreciate operation and instruction from William Monroe, SEM technician in the UAB School of Engineering.

References

- [1] M. Endo, S. Iijima, and M. S. Dresselhaus, *Carbon Nanotubes*, Elsevier, 1997.
- [2] K. Song, Y. Zhang, J. Meng et al., "Structural polymer-based carbon nanotube composite fibers: understanding the processing-structure-performance relationship," *Materials*, vol. 6, no. 6, pp. 2543–2577, 2013.
- [3] P. R. Bandaru, "Electrical properties and applications of carbon nanotube structures," *Journal of Nanoscience and Nanotechnology*, vol. 7, no. 4-5, pp. 1239–1267, 2007.
- [4] A. Moisala, Q. Li, I. A. Kinloch, and A. H. Windle, "Thermal and electrical conductivity of single- and multi-walled carbon nanotube-epoxy composites," *Composites Science and Technology*, vol. 66, no. 10, pp. 1285–1288, 2006.
- [5] M. E. Mackay, T. T. Dao, A. Tuteja et al., "Nanoscale effects leading to non-einstein-like decrease in viscosity," *Nature Materials*, vol. 2, no. 11, pp. 762–766, 2003.
- [6] M. E. Mackay, A. Tuteja, P. M. Duxbury et al., "General strategies for nanoparticle dispersion," *Science*, vol. 311, no. 5768, pp. 1740–1743, 2006.
- [7] L. J. Fetters, N. Hadjichristidis, J. S. Lindner, and J. W. Mays, "Molecular weight dependence of hydrodynamic and thermodynamic properties for well-defined linear polymers in solution," *Journal of Physical and Chemical Reference Data*, vol. 23, no. 4, pp. 619–640, 1994.
- [8] S. Jain, J. G. P. Goossens, G. W. M. Peters, M. Van Duin, and P. J. Lemstra, "Strong decrease in viscosity of nanoparticle-filled polymer melts through selective adsorption," *Soft Matter*, vol. 4, no. 9, pp. 1848–1854, 2008.
- [9] X.-L. Xie, Q.-X. Liu, R. K.-Y. Li et al., "Rheological and mechanical properties of PVC/CaCO₃ nanocomposites prepared by in situ polymerization," *Polymer*, vol. 45, no. 19, pp. 6665–6673, 2004.
- [10] J. W. Cho and D. R. Paul, "Nylon 6 nanocomposites by melt compounding," *Polymer*, vol. 42, no. 3, pp. 1083–1094, 2001.
- [11] C. Roberts, T. Cosgrove, R. G. Schmidt, and G. V. Gordon, "Diffusion of poly(dimethylsiloxane) mixtures with silicate nanoparticles," *Macromolecules*, vol. 34, no. 3, pp. 538–543, 2001.
- [12] A. Tuteja, M. E. Mackay, C. J. Hawker, and B. Van Horn, "Effect of ideal, organic nanoparticles on the flow properties of linear polymers: non-einstein-like behavior," *Macromolecules*, vol. 38, no. 19, pp. 8000–8011, 2005.
- [13] A. Tuteja, P. M. Duxbury, and M. E. Mackay, "Multifunctional nanocomposites with reduced viscosity," *Macromolecules*, vol. 40, no. 26, pp. 9427–9434, 2007.
- [14] R. G. Schmidt, G. V. Gordon, C. A. Dreiss et al., "A critical size ratio for viscosity reduction in poly(dimethylsiloxane)-polysilicate nanocomposites," *Macromolecules*, vol. 43, no. 23, pp. 10143–10151, 2010.
- [15] A. Petriccione, M. Zarrelli, V. Antonucci, and M. Giordano, "Aggregates of chemically functionalized multiwalled carbon nanotubes as viscosity reducers," *Materials*, vol. 7, no. 4, pp. 3251–3261, 2014.
- [16] Q. Zhang, D. R. Lippits, and S. Rastogi, "Dispersion and rheological aspects of SWNTs in ultrahigh molecular weight polyethylene," *Macromolecules*, vol. 39, no. 2, pp. 658–666, 2006.
- [17] L. Li, W. Wang, E. D. Laird, C. Y. Li, M. Defaux, and D. A. Ivanov, "Polyethylene/carbon nanotube nano hybrid shish-kebab obtained by solvent evaporation and thin-film crystallization," *Polymer*, vol. 52, no. 16, pp. 3633–3638, 2011.
- [18] L. Tan, Y. Chen, W. Zhou, S. Ye, and J. Wei, "Novel approach toward poly(butylene succinate)/single-walled carbon nanotubes nanocomposites with interfacial-induced crystallization behaviors and mechanical strength," *Polymer*, vol. 52, no. 16, pp. 3587–3596, 2011.
- [19] M. L. Minus, H. G. Chae, and S. Kumar, "Single wall carbon nanotube templated oriented crystallization of poly(vinyl alcohol)," *Polymer*, vol. 47, no. 11, pp. 3705–3710, 2006.
- [20] S.-N. Li, Z.-M. Li, M.-B. Yang, Z.-Q. Hu, X.-B. Xu, and R. Huang, "Carbon nanotubes induced nonisothermal crystallization of ethylene-vinyl acetate copolymer," *Materials Letters*, vol. 58, no. 30, pp. 3967–3970, 2004.
- [21] J. A. Fagan, M. L. Becher, J. Chun, and E. K. Hobbie, "Length fractionation of carbon nanotubes using centrifugation," *Advanced Materials*, vol. 20, no. 9, pp. 1609–1613, 2008.
- [22] D. R. Paul and L. M. Robeson, "Polymer nanotechnology: nanocomposites," *Polymer*, vol. 49, no. 15, pp. 3187–3204, 2008.
- [23] D. Simien, J. A. Fagan, W. Luo, J. F. Douglas, K. Migler, and J. Obrzut, "Influence of nanotube length on the optical and conductivity properties of thin single-wall carbon nanotube networks," *ACS Nano*, vol. 2, no. 9, pp. 1879–1884, 2008.
- [24] J. A. Fagan, M. Zheng, V. Rastogi et al., "Analyzing surfactant structures on length and chirality resolved (6,5) single-wall carbon nanotubes by analytical ultracentrifugation," *ACS Nano*, vol. 7, no. 4, pp. 3373–3387, 2013.
- [25] F. L. Binsbergen, "Heterogeneous nucleation in the crystallization of polyolefins. III. Theory and mechanism," *Journal of Polymer Science Part A-2: Polymer Physics*, vol. 11, no. 1, pp. 117–135, 1973.

Research Article

CO Gas-Induced Resonance Frequency Shift of ZnO-Functionalized Microcantilever in Humid Air

Lia Aprilia,^{1,2,3} Ratno Nuryadi,¹ Dwi Gustiono,¹ Nurmahmudi,⁴ Arief Udhiarto,² Djoko Hartanto,² Brian Yuliarto,⁵ Makoto Hosoda,³ Yoichiro Neo,³ and Hidenori Mimura³

¹Center for Materials Technology, Agency for the Assessment and Application of Technology, Puspitek Building No. 224, South Tangerang, Banten 15314, Indonesia

²Department of Electrical Engineering, Faculty of Engineering, Universitas Indonesia, Depok 16424, Indonesia

³Research Institute of Electronics, Shizuoka University, 3-5-1 Johoku, Naka-ku, Hamamatsu, Shizuoka 432-8011, Japan

⁴Center for Technology Strategy and Audit, Agency for the Assessment and Application of Technology, South Tangerang, Banten, Indonesia

⁵Engineering Physics Department, Institut Teknologi Bandung, Bandung 40132, Indonesia

Correspondence should be addressed to Ratno Nuryadi; ratno.nuryadi@bppt.go.id

Received 25 April 2017; Revised 6 July 2017; Accepted 3 August 2017; Published 10 September 2017

Academic Editor: Xiaowei He

Copyright © 2017 Lia Aprilia et al. This is an open access article distributed under the Creative Commons Attribution License, which permits unrestricted use, distribution, and reproduction in any medium, provided the original work is properly cited.

Resonance frequency shift of a zinc oxide- (ZnO-) functionalized microcantilever as a response to carbon monoxide (CO) gas has been investigated. Here, ZnO microrods were grown on the microcantilever surface by a hydrothermal method. The measurement of resonance frequency of the microcantilever vibrations due to the gas was carried out in two conditions, that is, gas flow with and without air pumping into an experiment chamber. The results show that the resonance frequency of the ZnO-functionalized microcantilever decreases because of CO in air pumping condition, while it increases when CO is introduced without air pumping. Such change in the resonance frequency is influenced by water vapor condition, and a possible model based on water-CO combination was proposed.

1. Introduction

Microcantilever-based sensors could replace conventional sensors because of the ability to detect ultrasmall mass with fast response time. The working principle of this sensor is based on deflection of microcantilever (MC) due to an object attached on its surface (static mode) or resonance frequency shift of the MC vibration due to an object (dynamic mode). So far, the smallest mass detected using MC has been reported as femtogram (10^{-15} gram) level by Sone et al. [1], attogram level (10^{-18} gram) [2], and zeptogram level (10^{-20} gram) by Roukes group [3].

On the other hand, in order to selectively detect chemical or biological molecules, a sensitive layer must be deposited on the microcantilever surface, such as polymer [4] and metal oxide sensitive layers [5]. In gas detection, several publications have shown that the resonance frequency of MC decreased due to exposure of the gas, such as mercury [6],

volatile organic compounds [7], ethanol [8], carbon dioxide [9], freon [10], and water vapor [11]. However, for real sensor applications, the sensor response should be considered in various conditions, such as in higher humidity or vacuum conditions.

Generally, gas detection on metal oxide surfaces, such as zinc oxide (ZnO) which has a great potential in sensing applications, is especially influenced by the presence of humidity [12]. In ambient condition, the surface is fully covered by molecularly adsorbed water [13]. Gouvea et al. reported that CO_2 and H_2O energetically had same possibility for binding to a ZnO surface [14]. Consequently, the water-CO combination should be considered as a model system for gas detection on metal oxide surfaces.

In this work, we have grown ZnO microrods on the microcantilever surface as sensitive layers for gas detection and studied the effect of carbon monoxide (CO) on resonance frequency of the MC at a room temperature. Here, we studied

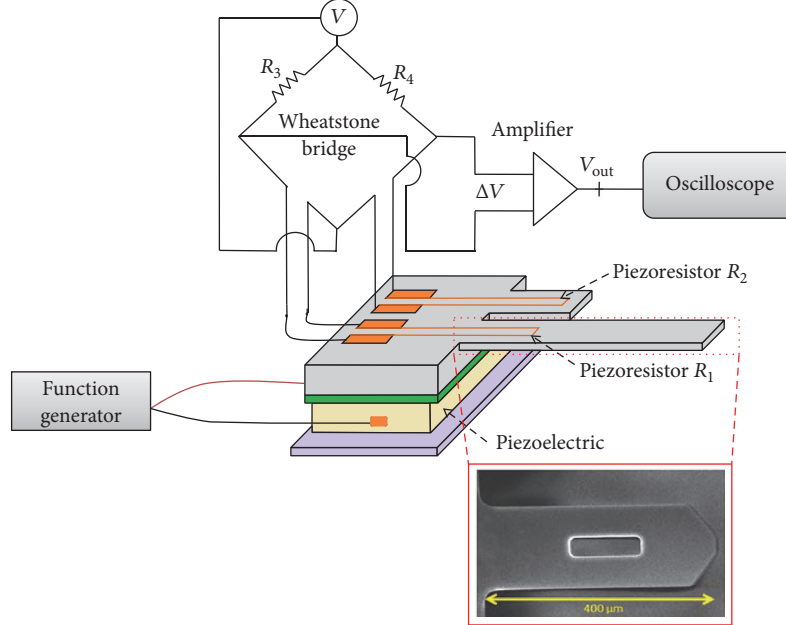


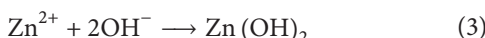
FIGURE 1: Schematic circuit system using piezoresistive microcantilever. The inset figure is a SEM image of the microcantilever.

the effect of CO in different conditions, that is, with and without air flow. We experimentally observed a decrease in the resonance frequency due to gas flow with air pumping and an increase in the resonance frequency without air pumping. The possible model is also proposed to explain the experimental results.

2. Experimental Details

2.1. ZnO Microrods Formation. Formation of the ZnO microrods consists of initial layer preparation and growth of rods. First, the MC was coated by an initial solution which was made of 0.3 M diethanolamine in ethylene glycol and stirred at 75°C for 1 hour. The coated cantilever was annealed at 100°C for 30 minutes.

The ZnO was then grown on the cantilever surface by dipping it in ZnO solution at 90°C for 2 hours. Here, the ZnO solution was prepared by using 0.02 M zinc nitrate tetrahydrate ($\text{Zn}(\text{NO}_3)_2 \cdot 6\text{H}_2\text{O}$) and hexamethylenetetramine ($(\text{CH}_2)_6\text{N}_4$) in ethanol and aqua bidest (1:3). Hexamethylenetetramine acts as a pH buffer of the solution and supply of OH^- ions, as seen in the following reaction equations:



Precipitation of ZnO nuclei starts when the concentration of Zn^{2+} and OH^- ions exceeds a critical value. Here, the ZnO nuclei are building blocks for the formation of the rods.

Thus, $\text{Zn}(\text{OH})_2$ can be transformed into ZnO crystals with hexagonal shape due to the crystal habits of ZnO. As a result, ZnO microrods are grown. Finally, the ZnO-microrods-coated MC is dried at 80°C for 1 hour. To confirm the growth of ZnO, we performed energy dispersive spectroscopy (EDS) analysis and scanning electron microscopy (SEM) on the MC surface.

2.2. Electronic Circuit. In this work, a commercial piezoresistive microcantilever (Seiko Instruments Inc.) was used, as shown in Figure 1. A long MC (see an inserted SEM image in Figure 1) has a length of 400 μm , a width of 50 μm , spring constant (k) of 4 N/m, and piezoresistor R_1 of about 630 Ω [1]. A short cantilever with piezoresistor R_2 (about 630 Ω) is a reference cantilever, which is crucial in order to reduce background noise, such as thermal drift and gas turbulence [15]. In the piezoresistive microcantilever, the deflection of it produces a resistivity change of the piezoresistor. Such resistivity change was measured by using a Wheatstone bridge, which is constructed by two piezoresistors in the MC (R_1 and R_2) and two external resistors (R_3 and R_4), as schematically shown in Figure 1.

Output of Wheatstone bridge (ΔV) in Figure 1 could be written as $\Delta V = (R_1R_3 - R_2R_4)V/(R_1 + R_2)(R_3 + R_4)$. The output ΔV is varied when the value of piezoresistor R_1 changes during gas detection. ΔV is then amplified resulting in V_{out} , which is monitored with an oscilloscope. In order to actuate the MC in dynamic mode operation, a function generator is used for applying a sinusoidal wave to piezoelectric element.

2.3. Carbon Monoxide Gas Measurement. When the actuated microcantilever vibrates in a certain frequency, we measured the resonance frequency of the MC vibration before and

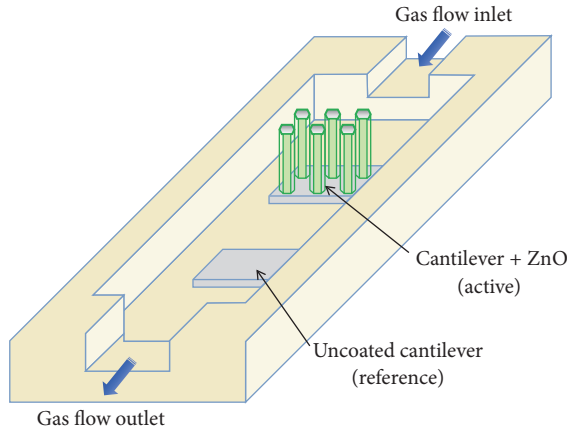


FIGURE 2: Schematic view of chamber for gas measurement.

after gas detection. In gas measurements, we first put two cantilevers inside the chamber, as shown in Figure 2. The first cantilever was coated by ZnO microrods (active cantilever), while the second one was an uncoated reference cantilever. We conducted the measurement at room temperature. First, carbon monoxide gas was introduced into the chamber at various concentrations, that is, 30 ppm, 70 ppm, and 100 ppm. Then air was pumped to the chamber by using an air compressor. The resonance frequency shifts for each gas concentration were measured by using an oscilloscope. Second, carbon monoxide gas was introduced into the chamber at a flow rate of 1 ml/min at 25°C and relative humidity of 65% RH. Here, the gas was inserted (gas ON) and turned off (gas OFF) until stable condition was reached. Then, change of the resonance frequency as a function of time was monitored by using the oscilloscope. We should note that, in contrast to the first condition, air was not pumped into the chamber during gas OFF condition.

3. Results and Discussions

3.1. Characterization of Zinc Oxide Rods. ZnO microrods were successfully grown on silicon microcantilevers as a sensitive layer. Figure 3 shows a SEM image of them deposited on the MC surface forming a flower-like ZnO structure. Even though the formed rods are not well aligned, we can see the hexagonal shape of the rods. It is predicted that the crystal structure of ZnO fabricated in this way is hexagonal wurtzite. The length and diameter of ZnO microrods are approximately 6 μm and 1 μm , respectively. These microstructures have a virtue of large surface area to adsorb gas molecules.

Next, the chemical composition of the ZnO microrods was characterized by EDS. Table 1 shows EDS result for the "A" point of the rod deposited on a silicon MC surface (see Figure 3). The elements of Zn and O refer to ZnO composition with ratio 1.6:1, which indicate the presence of defects of interstitial Zn or deficiency of the oxygen. Oxygen vacancies in ZnO are attributed to donor type defects contributing n-type conductivity of the material. The element Si comes from silicon material of the microcantilever, while the element Au is originated from residual conductive

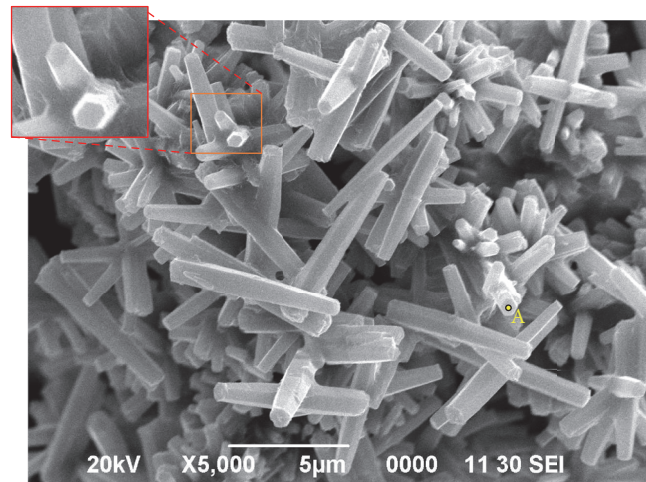


FIGURE 3: Scanning electron micrograph of ZnO sensitive layer. The inset is a zoomed-in image of hexagonal shape of ZnO. The yellow character "A" indicates EDS sensing position.

TABLE 1: Energy dispersive spectroscopy (EDS) result for ZnO.

Element	Mass%	Error%	Atom%
O	12.29	0.31	36.43
Si	2.65	0.35	4.48
Zn	79.63	1.54	57.78
Au	5.43	1.04	1.31
Total	100.00		100.00

material during SEM preparation. Even though the ratio of Zn and O is not equal to 1:1, the EDS result clearly shows that the rods formed on the MC surface are pure ZnO.

3.2. Resonance Frequency Shift due to Gas Adsorption

3.2.1. Various CO Concentrations during Air Pump Treatment. The initial frequencies of both microcantilevers were measured before measurement. The initial resonance frequency (f) of the active cantilever was 29.060 kHz, while the frequency of reference cantilever was 40.340 kHz. Note that the resonance frequency of the active cantilever before ZnO coating was about 40 kHz. The decrease in its resonance frequency ($\Delta f \sim 10 \text{ kHz}$) is caused by ZnO microrods formation.

CO at concentrations of 30 ppm, 70 ppm, and 100 ppm was then introduced and ambient air was pumped into the chamber by using an air compressor pump before and after introducing the gas. The effect of CO at various concentrations is shown in Figure 4. First, 30 ppm CO gas was introduced into the chamber, resulting in decrease of the resonance frequency of the active cantilever (blue marker) to 28.880 kHz. After stabilizing, the gas flow was stopped and air was pumped into the chamber. As a result, the resonance frequency increased to 29.050 kHz. Such resonance frequency shift (Δf) of 180 Hz is a function of a mass change (Δm) due to adsorbed gas on the ZnO surface which can be calculated using (5) and (6) [1]. It is noted that decrease in

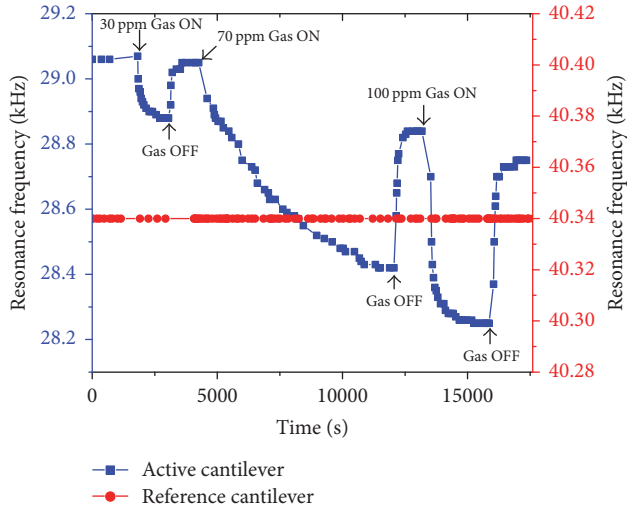


FIGURE 4: Resonance frequency as a function of time for both microcantilevers (active cantilever: blue square markers for left axis, and reference cantilever: red circle markers for right axis) exposed to carbon monoxide gas in constant flow.

Q -factor [16] of ZnO-coated MC occurs when the gas was introduced ($\Delta Q \sim 1$ due to 1 ml/min flow of CO), but such small change of Q -factor does not affect the measurement of resonance frequency shift. Our results about a decrease and an increase in resonance frequency due to gas ON and OFF are consistent with previous reports of the microcantilever-based gas detection [7–10].

From (5), the mass of the ZnO-coated MC (m) is determined to be 120 picograms, and using (6), the absorbed molecules on the ZnO layer are calculated to be 2.56 picograms. So the sensor sensitivity for carbon monoxide detection is about 8.27 femtogram/Hz.

$$m = \frac{k}{(2\pi f)^2}, \quad (5)$$

$$\Delta m = -2 \frac{m}{f} \Delta f. \quad (6)$$

Next, 70 ppm CO was inserted and the resonance frequency decreased to 28.420 kHz. The longer response time for reaching a stable state may be due to air humidity change during this measurement. When the gas was turned off and the air compressor was turned on, the resonance frequency of the MC increased to 28.840 kHz. Finally, the MC was exposed to 100 ppm CO. The resonance frequency shifted to 28.250 kHz and then increased to be 28.750 kHz due to gas OFF and air flow. The difference of 310 Hz in the resonance frequency between initial resonance frequency (29.060 kHz) and frequency after the gas measurement (28.750 kHz) is probably caused by remaining gas molecules of about 1.49 fg on the zinc oxide layer. Such difference was also found for gas concentrations of 30 ppm and 70 ppm. It is noted that the resonance frequency of the reference cantilever (red marker) was almost constant during the measurement. We previously found that the water vapor was directly adsorbed on the

uncoated MC which reduced the resonance frequency of MC [11]. However, in this work, the gas or water vapor may be adsorbed on the uncoated MC surface generating a change in its resonance frequency of less than 10 Hz. As a result, the frequency shift at the graph almost disappeared. Therefore, it is convincing that the ZnO microrods play the role of the sensitive layer for response to gas.

Figure 4 also shows that the resonance frequency shift of the ZnO-coated MC increases with increasing concentration of CO, which is plotted in Figure 5. Such frequency shift depends on the number of CO molecules adsorbed on the ZnO surface. Therefore, the higher gas concentration results in larger resonance frequency shift. In Figure 5, the mass change of each concentration is calculated according to (6).

The decrease of the active resonance frequency due to CO can be probably explained as follows. Mostly, metal oxides adsorb water vapor molecules at their surface in ambient air. In the present experiment, air pumping treatment provides water vapor spreading inside the experiment chamber. Water molecules in air are likely to be dissociated on the ZnO surface into OH^- and H^+ . Such water dissociation on ZnO surface into OH^- and H^+ may produce the hydrogen-rich condition of the hydrogen ion, as discussed by Xu et al. [12]. Air pumping treatment generates a large amount of water vapor inside the chamber resulting in more dissociated hydrogen ion (hydrogen-rich) and vice versa. Under hydrogen-rich conditions, all ZnO surfaces have low formation energies [12] so that it would be easier to bind other molecules, such as CO molecules. Due to the presence of CO, the gas molecules are physically adsorbed on ZnO surface through the dissociated water molecules (illustrated in Figure 6), resulting in the increase in the effective mass of the cantilever. Such increased mass generates the decrease in resonance frequency of the microcantilever.

3.2.2. Constant Flow of CO Gas without Air Pump Treatment. In this experiment, the CO gas was introduced into the chamber at a constant rate of 1 ml/min at humidity of 65% RH, and then the gas was turned off without air pump until reaching a stable frequency. The initial resonance frequency (f) of the active cantilever was 28.026 kHz, while the frequency of reference cantilever was 40.351 kHz. When gas flow was switched ON and OFF, the resonance frequency of both cantilevers was measured and the frequency shift was investigated. The resonance frequency change of both microcantilevers due to CO can be seen in Figure 7. In contrast to the previous result in Figure 4, the resonance frequency of active MC increased due to gas exposure without air pump treatment. In order to explain this result, we firstly calculate the concentration of CO (C_{CO}) in the chamber at stable condition using the following equation [17]:

$$C_{\text{CO}} = \frac{V_{\text{CO}} \rho_{\text{CO}}}{V_{\text{ch}} (\text{Mr}_{\text{CO}}/22.4) (273/(273+T)) (P/101325)} \text{ in ppm,} \quad (7)$$

where V_{CO} is the sample volume of CO in m^3 , ρ_{CO} is relative density (g/m^3), V_{ch} is the chamber volume in m^3 , Mr_{CO} is the molar mass of the CO (g/mol), T is temperature in Kelvin,

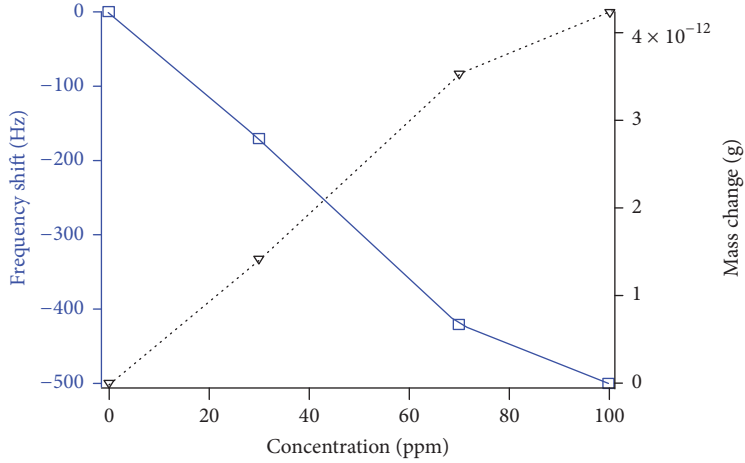


FIGURE 5: Resonance frequency shift (blue solid curve for left axis) and mass change (black dotted curve for right axis) versus CO concentration with average sensitivity of 8.27 femtogram/Hz.

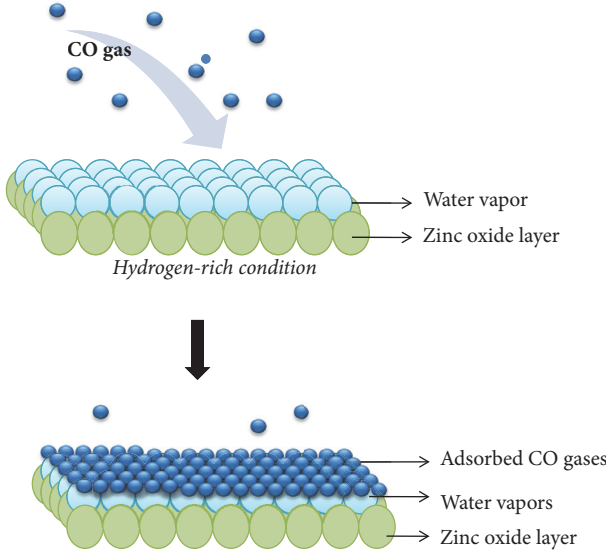


FIGURE 6: Possible model of CO gas adsorption in the presence of water vapors.

and P is pressure in Pascal. In this calculation, we choose the condition at 611 s in Figure 7 where the resonance frequency saturated at $f \sim 29.18$ kHz after resonance frequency change due to CO, and $V_{\text{CO}} = 0.01018 \text{ m}^3$, $\rho_{\text{CO}} = 1.14 \text{ kg/m}^3$, $V_{\text{ch}} = 8 \times 10^{-5} \text{ m}^3$, $M_{\text{CO}} = 28 \text{ g/mol}$, $T = 275 \text{ K}$, and $P = 101.325 \text{ kPa}$. We obtained that the CO concentration inside the chamber at the resonance frequency shift of $\Delta f \sim 1.16 \text{ kHz}$ is approximately 126.68 ppm.

Next, the CO gas flow was turned off, resulting in a decrease in the resonance frequency of active MC (blue marker) to be 28.506 kHz. This frequency did not return back to its initial value. As the gas flow was turned on, the resonance frequency of the active cantilever increased again to 29.276 kHz with the resonance frequency shift of 0.77 kHz, and the frequency decreased to 28.316 kHz due

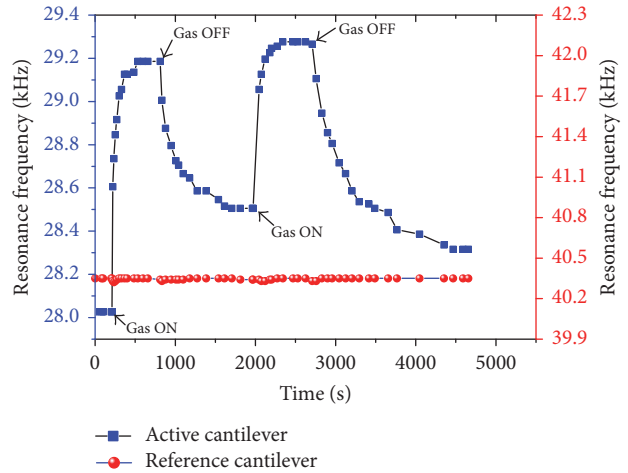


FIGURE 7: Resonance frequency versus time for both microcantilevers exposure to carbon monoxide gas without air pump treatment (active cantilever: blue square markers for left axis; reference cantilever: red circle markers for right axis).

to gas flow being turned off. As shown in Figure 4, the resonance frequency of reference MC (red marker) is also almost unchanged during the measurement.

Unlike the gas measurement with air pump treatment, the resonance frequency of the active MC increases due to effect of CO. The possible mechanism of this result may be due to the influence of water vapor which is explained in Figure 8. In high humidity, water vapor is adsorbed and dissociated on zinc oxide layer. In this experiment, the air pump treatment was not performed, resulting in hydrogen-poor condition on ZnO surface. Therefore, the structures with more dissociated water vapor on the ZnO surface become unstable. As a result, when CO is inserted into the chamber, the dissociated water vapor is desorbed from the ZnO surface and CO is directly adsorbed on the ZnO layer. Due to the lighter mass of CO gas layer, the resonance frequency of the active MC increases.

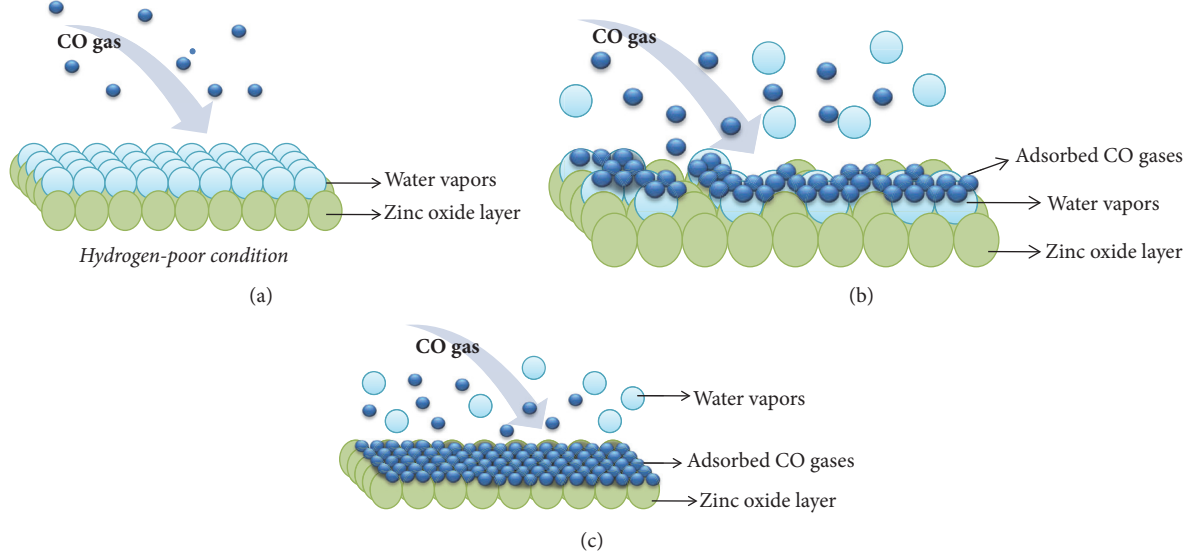


FIGURE 8: Possible model of CO gas adsorption in high humidity condition: (a) water vapors are present on the ZnO surface when CO is introduced; (b) CO gases produce the water vapor adsorption; (c) CO gases bind directly with zinc oxide layer.

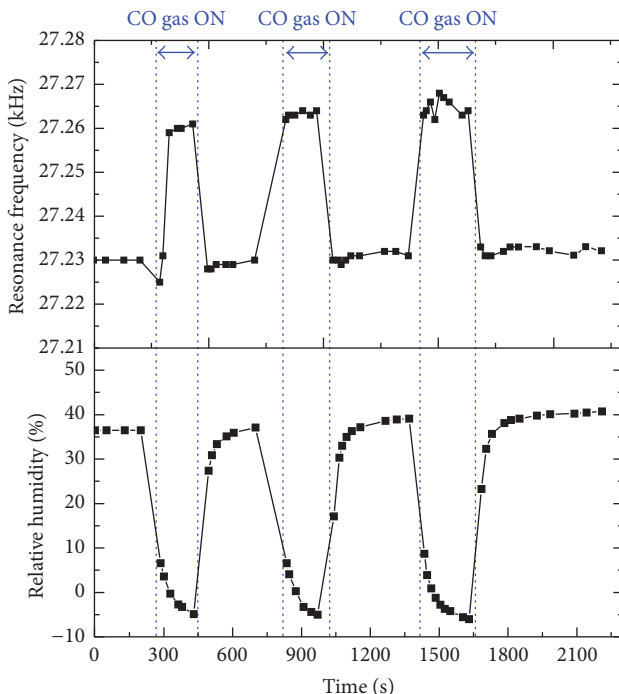


FIGURE 9: Relative humidity change due to introduced CO gas compared to resonance frequency change of the ZnO-coated MC.

Here, the resonance frequency does not return to an initial value after gas OFF because of limitation of the water vapor molecules inside the chamber.

To support the possible model in Figure 8, relative humidity (RH) was changed while CO was inserted, as shown in Figure 9. Before introducing CO, the resonance frequency of active cantilever, relative humidity, and temperature were measured to be 27.230 kHz, 36.5%, and 19.4°C, respectively.

When CO was inserted, the relative humidity decreased. We should note that the minus RH might be originated from sensor's offset error, where the conventional sensor is used in 1 atm air condition. The sensing condition at minus RH is different; that is, ambient gas contains CO gas (not pure air). However, the tendency of the RH changes reflects the humidity change. And intervals showing approximately +35% RH in Figure 9 are measured under pure air conditions. Therefore, decrease in the RH data during insertion of CO exhibited a certain change in the humidity. Such results assumed that water vapor was desorbed from the ZnO surface and CO was adsorbed on the surface. This alteration results in an increase on the resonance frequency of the active microcantilever. As CO was switched off, relative humidity increased. Probably, CO was desorbed from the ZnO surface and replaced by water vapor, resulting in a decrease of the resonance frequency. The measurement was repeated three times with similar results. These results show that the model on Figure 8 can explain the increase of resonance frequency for the active cantilever due to CO exposure.

In this study, the measurements were done in humid air at room temperature. Therefore, the mechanisms proposed above may not be appropriate for high temperature. If the substrate temperature is raised, the water vapors at the ZnO surface evaporate. In this case, CO will be directly absorbed on the ZnO surface, resulting in a decrease in the resonance frequency of the active MC. The same condition occurs if the ZnO surface is modified with a hydrophobic coating, in which the water vapor should not be adsorbed on the ZnO surface, and in case of CO adsorption, the gas will be adsorbed on the hydrophobic layer.

4. Conclusions

We have grown ZnO microrods on MC surfaces and studied the gas response to the ZnO rods in humid air at room

temperature. The results showed that the resonance frequency of the ZnO-MC changed due to interaction with CO. It was found that the sensitivity for CO detection was about 8 femtogram/Hz. However, the response is highly influenced by the presence of humidity. The resonance frequency of the ZnO-MC decreased due to CO in rich water vapor condition, while the resonance frequency increased when CO was introduced in poor water vapor. We proposed the water-CO combination-based model to explain the results.

Conflicts of Interest

The authors declare that they have no conflicts of interest.

Acknowledgments

This paper was funded by an incentive research grant from Ministry of Research, Technology and Higher Education of the Republic of Indonesia which the authors gratefully acknowledge.

References

- [1] H. Sone, A. Ikeuchi, T. Izumi, H. Okano, and S. Hosaka, "Femtogram mass biosensor using self-sensing cantilever for allergy check," *Japanese Journal of Applied Physics, Part 1: Regular Papers and Short Notes and Review Papers*, vol. 45, no. 3B, pp. 2301–2304, 2006.
- [2] M. Li, H. X. Tang, and M. L. Roukes, "Ultra-sensitive NEMS-based cantilevers for sensing, scanned probe and very high-frequency applications," *Nature Nanotechnology*, vol. 2, no. 2, pp. 114–120, 2007.
- [3] Y. T. Yang, C. Callegari, X. L. Feng, K. L. Ekinci, and M. L. Roukes, "Zeptogram-scale nanomechanical mass sensing," *Nano Letters*, vol. 6, no. 4, pp. 583–586, 2006.
- [4] C. Steffens, F. L. Leite, A. Manzoli, R. D. Sandoval, O. Fatibello, and P. S. P. Herrmann, "Microcantilever sensors coated with a sensitive polyaniline layer for detecting volatile organic compounds," *Journal of Nanoscience and Nanotechnology*, vol. 14, no. 9, pp. 6718–6722, 2014.
- [5] N. Kilinc, O. Cakmak, A. Kosemen et al., "Fabrication of 1D ZnO nanostructures on MEMS cantilever for VOC sensor application," *Sensors and Actuators, B: Chemical*, vol. 202, pp. 357–364, 2014.
- [6] T. Thundat, E. A. Wachter, S. L. Sharp, and R. J. Warmack, "Detection of mercury vapor using resonating microcantilevers," *Applied Physics Letters*, vol. 66, pp. 1695–1697, 1995.
- [7] L. Guan, J. Zhao, S. Yu, P. Li, and Z. You, "Investigation of the frequency shift of a SAD circuit loop and the internal microcantilever in a gas sensor," *Sensors*, vol. 10, no. 7, pp. 7044–7056, 2010.
- [8] L. Fadel, F. Lochen, I. Dufour, and O. Français, "Chemical sensing: Millimeter size resonant microcantilever performance," *Journal of Micromechanics and Microengineering*, vol. 14, no. 9, pp. S23–S30, 2004.
- [9] C. Yim, M. Lee, M. Yun, G. Kim, K. T. Kim, and S. Jeon, "CO₂-Selective Nanoporous Metal-Organic Framework Microcantilevers," *Scientific Reports*, vol. 5, no. 1, 2015.
- [10] J. Zhou, P. Li, S. Zhang et al., "Zeolite-modified microcantilever gas sensor for indoor air quality control," *Sensors and Actuators, B: Chemical*, vol. 94, no. 3, pp. 337–342, 2003.
- [11] R. Nuryadi, A. Djajadi, R. Adiel, L. Aprilia, and N. Aisah, "Resonance frequency change in microcantilever-based sensor due to humidity variation," *Materials Science Forum*, vol. 737, pp. 176–182, 2013.
- [12] H. Xu, W. Fan, A. L. Rosa, R. Q. Zhang, and T. Frauenheim, "Hydrogen and oxygen adsorption on ZnO nanowires: a first-principles study," *Physical Review B*, vol. 79, no. 7, 2009.
- [13] P. M. Kowalski, B. Meyer, and D. Marx, "Composition, structure, and stability of the rutile TiO₂(110) surface: Oxygen depletion, hydroxylation, hydrogen migration, and water adsorption," *Physical Review B - Condensed Matter and Materials Physics*, vol. 79, no. 11, Article ID 115410, 2009.
- [14] D. Gouvêa, S. V. Ushakov, and A. Navrotsky, "Energetics of CO₂ and H₂O adsorption on zinc oxide," *Langmuir*, vol. 30, no. 30, pp. 9091–9097, 2014.
- [15] H. P. Lang, R. Berger, F. Battiston et al., "A chemical sensor based on amicromechanical cantilever array for the identification of gases and vapors," *Applied Physics A: Materials Science and Processing*, vol. 66, no. 1, pp. S61–S64, 1998.
- [16] A. Phani, V. Putkaradze, J. E. Hawk, K. Prashanthi, and T. Thundat, "A nanostructured surface increases friction exponentially at the solid-gas interface," *Scientific Reports*, vol. 6, Article ID 32996, 2016.
- [17] Y. Dong, W. Gao, Q. Zhou, Y. Zheng, and Z. You, "Characterization of the gas sensors based on polymer-coated resonant microcantilevers for the detection of volatile organic compounds," *Analytica Chimica Acta*, vol. 671, no. 1-2, pp. 85–91, 2010.

Research Article

Magnetic-Field-Enhanced Morphology of Tin Oxide Nanomaterials for Gas Sensing Applications

Jonathan C. Briones, Gwen Castillon, Michael P. Delmo, and Gil Nonato C. Santos

Physics Department, De La Salle University, 1004 Manila, Philippines

Correspondence should be addressed to Jonathan C. Briones; jonathan.briones@dlsu.edu.ph

Received 9 March 2017; Accepted 3 May 2017; Published 18 June 2017

Academic Editor: Ciuyuan Qiu

Copyright © 2017 Jonathan C. Briones et al. This is an open access article distributed under the Creative Commons Attribution License, which permits unrestricted use, distribution, and reproduction in any medium, provided the original work is properly cited.

We studied the effect of an external magnetic field (up to 0.31 T) on the growth of SnO_2 nanowires fabricated using the horizontal vapor phase growth (HPVG) technique. The morphology of the nanowires was characterized by using scanning electron microscopy (SEM), and the chemical composition was characterized by energy dispersive X-ray (EDX) analysis. We found that the length of nanowires was significantly enhanced by the application of EMF. The aspect ratio, as well as the density of the fabricated nanowires, increased with increasing magnetic field intensity. Although the physics behind the morphology enhancement of the nanowires under magnetic field is still being investigated, nevertheless, we demonstrated that the magnetic field could be used as a key parameter to control the morphology of tin oxide nanomaterials grown via HPVG technique. The magnetically enhanced nanowires were used in the development of a gas sensor and were found to be sensitive to hydrogen sulfide gas and the headspace gas emitted by spoiling meat.

1. Introduction

There are tremendous interests in the fabrication of various nanomaterials with diversified morphologies, such as nanoparticles [1] and nanowires [2, 3], because of their potential applications in electronics [1, 4, 5] and medicine [6]. Physical and chemical [4, 7] methods, such as thermal evaporation [8], chemical vapor deposition [9], sol-gel method [10], and hydrothermal methods [8], are being used to fabricate nanomaterials. Typically, for the physical methods, temperature, pressure, and chemical addition [7] are the key parameters being controlled to modify the morphologies of nanomaterials. In this study, the parameter that was varied to control the morphology of tin oxide (SnO_2) nanomaterials fabricated by using our home-developed horizontal vapor phase growth (HPVG) technique [11] was the presence of an external magnetic field. The use of a magnetic field (0.048 T) as an external parameter in the HPVG method was first reported by De Mesa et al. [6] in the synthesis of iron oxide nanoparticles for glucose sensing applications which were claimed to have enhanced the superparamagnetic property

of the material. No other attempts were made to fabricate nanomaterials using the HPVG technique with external magnetic field as a controlling parameter.

Nanostructured SnO_2 offers a great potential for energy and environmental applications including gas sensing due to large surface area, low cost, and low toxicity [4]. Its gas sensing capabilities are widely reported due to its exceptionally high sensitivity to gas reaction and adsorption. Nonetheless, much innovative science needs discovery, and new techniques must be explored in the fabrication of this type of material by exploiting strategies in the field of materials science and nanotechnology. The use of chemical and biofunctionalized gas sensors is important in many aspects such as personal safety and security, detection and diagnosis of pollutants and poisons, health, semiconductor processing, agriculture, and automotive and aerospace industries [2, 12].

Recently, it has been shown that the HPVG deposition is successful in synthesizing nanostructured SnO_2 . However, the said technique allows the growth of many kinds of structures along the length of the substrate. Thus, understanding the growth mechanism of nanomaterials in HPVG technique

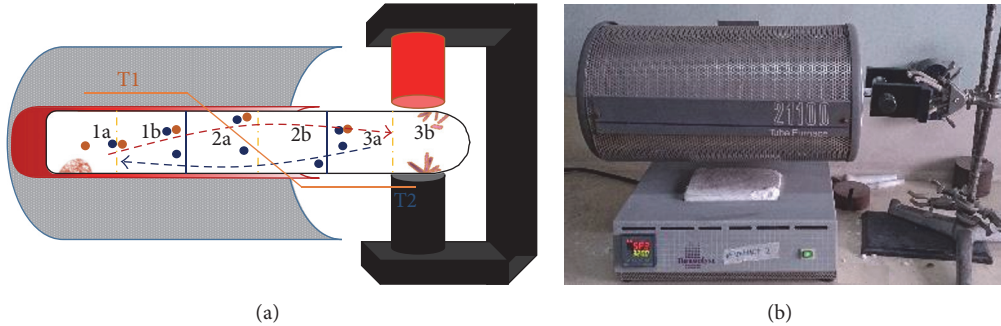


FIGURE 1: Horizontal vapor phase crystal growth setup. (a) Setup illustration. (b) Actual system.

would make it possible to control or alter the growth kinetics of the SnO_2 nanomaterial resulting in better or improved materials and devices.

In this work, the effect of an external magnetic field (0 up to 0.31 T) on the growth of tin oxide nanowires was examined. Magnetostatic interaction has an important role in the growth mechanism of nanomaterials. Several studies have reported on the influence of magnetic field on the nucleation kinetics of paramagnetic and diamagnetic materials during crystallization and precipitation. These reports verify the effect of applied magnetic field on the aspect ratio of nanostructures as well as its properties [13–15]. Applied magnetic field is cited to be an efficient tool in the fabrication of one-dimensional (1D) nanomaterials [16].

The fabrication of 1D metal oxide nanostructures, having diameters below ~ 100 nm, has attracted attention due to various applications in numerous fields. Due to the large surface-to-volume ratio in 1D structures like nanowires, nanorods, nanotubes, and so forth, a significant number of surface atoms (or molecules) can participate in surface reactions resulting in better sensitivity and selectivity [2, 3]. One potential application of 1D structures is the evaluation of the freshness of meat through its headspace gas.

Meat spoilage is a sensorial quality consisting of the occurrence of off-odors (bacterial activity) and off-flavors or discoloration, which are characteristics that help determine its shelf life. Detectable organoleptic spoilage is a result of decomposition and the formation of metabolites caused by the growth of microorganisms. The emission of volatile gases by anaerobic and aerobic bacteria during spoilage can be used to detect the spoilage of meat [17]. Several studies have pointed to the concentrations of sulfurous compounds and biogenic amines as the primary factors that can be used in evaluating meat freshness. Thus, measuring the emission of volatile organic gases can be correlated to the degree of meat deterioration [18].

Sensory analysis of meat spoilage is very expensive and not always practical. Developing sensing materials that can ensure the safety and quality of meat products would benefit both producers and consumers of meat. The devices that need to be developed must not only be robust and compact but also have high sensitivity, selectivity, and reversibility in ambient temperature conditions with low manufacturing cost [12]. In an attempt to develop a device with the above-mentioned

characteristics, the SnO_2 nanostructures fabricated in this study were used as the sensing element of a spoilage detector gas sensor.

In this paper, external magnetic field intensities of 0 T (control), 0.25 T, and 0.31 T were applied during the synthesis of tin oxide nanomaterials. The surface morphology and elemental composition were investigated using scanning electron microscopy (SEM), transmission electron microscopy (TEM), and energy dispersive X-ray (EDX) analysis, while the crystallinity was investigated using X-ray diffraction (XRD) analysis. The responses of the fabricated sensor substrate to hydrogen sulfide (H_2S) gas, ethanol, methanol, and meat headspace were also investigated.

2. Experimental Setup

2.1. Synthesis of Tin Oxide Nanomaterials via HVPG. Fused silica tubes with one end sealed were used as containers of the bulk SnO_2 powder of 99% purity and <5-micron grain size obtained from Merck. The tubes were loaded with fifty (50) milligrams of bulk powder and then evacuated using a Thermionics High Vacuum System to a pressure of about 10^{-6} Torr. The tubes were then fully sealed using a high temperature blow torch to a length of 15 cm.

The sealed tubes were inserted halfway through a ThermoMolyne horizontal tube furnace and then cured at 1,200°C with a ramp time of 40 minutes for 4-hour, 6-hour, and 8-hour curing time. Regions of interest were designated according to their respective position in the furnace during the annealing process. The part of the tube which contained the powder and which was inside the furnace was labeled section 1. The middle portion of the tube near the opening of the furnace was designated as section 2. The last region of interest, the part of the tube that was completely out of the furnace, was designated as section 3. Each section had a length of 5 cm and was further divided into two sections, a and b. The experimental setup and schematic diagram are shown in Figure 1.

The position of the tube in the furnace provided a temperature gradient along its length. Using a type K thermocouple, it was confirmed that section 1 was heated at 1,200°C. The temperature of section 2 was found to range from 353° to 800°C along its length, while the temperature of section 3 was found to range from 63° to 352°C.

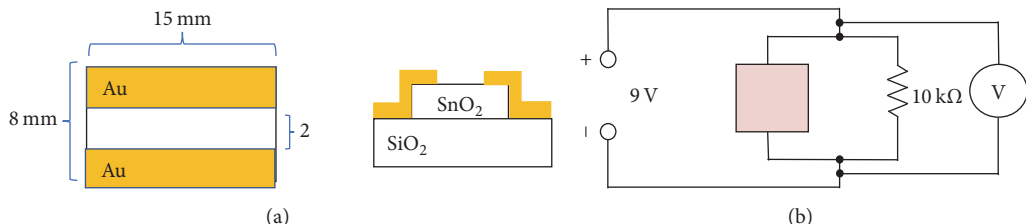


FIGURE 2: Schematic diagram of (a) an embodiment of a gas sensor electrode; (b) circuit diagram of gas sensor setup.

In order to verify the influence of the magnetic field on the growth of nanomaterials, its intensity was varied (0 T, 0.25 T, and 0.31 T) as well as its position along the tube (sections 3a and 3b). The said magnetic field was supplied by a variable gap neodymium magnet.

JEOL-JSM 5310 Scanning Electron Microscope and Libra 200 CsSTEM Transmission Electron Microscope from Carl Zeiss Singapore were used in identifying the structures of the synthesized nanomaterials. Elemental composition of the samples was also determined using an Oxford EDX Link Isis System. The crystal structure of the as-synthesized nanomaterials was determined using Bruker D2 PHASER X-Ray Diffractometer.

2.2. Fabrication of the SnO₂ Nanomaterial Sensor Substrate. The section with the highest density of synthesized nanowires was used in the fabrication of a gas sensing substrate. A 2 mm wide middle section of the collected substrates was then covered. To create gold electrodes on the substrates, the partly covered substrates were sputtered with gold for 30 seconds at 50 mA using a JEOL JFC-1200 Fine Coater. The resulting configuration of the gas sensing substrate is shown in Figure 2. The nanomaterials which were not sputtered with gold were the ones to detect gas emitted from spoiling meat as indicated by the change in the resistivity of the material, which was then converted to a voltage measurement and read via a PASCO Scientific voltage sensor.

A two-neck flat bottom flask was used as the chamber for testing the gas sensing ability of the sensor substrate. A Loadstar DC power supply was used to provide an input voltage of 9 V with current of 0.5 A. A constant resistance provided by a 10 kΩ resistor was utilized (Figure 2(b)). Passport Interfaced PASCO Scientific voltage sensor and DataStudio for data acquisition were employed to measure the voltage response of the sensor (Figure 3). The experimental setup was operated at ambient temperature during the data acquisition.

2.3. Nanomaterial Sensor Substrate Gas Sensing Test. To determine the ability of the sensor substrate to detect gas and volatile compounds such as hydrogen sulfide (H₂S) gas, ethanol, methanol, and the headspace of confined fresh and spoiled pork meat samples were introduced into the gas chamber. The H₂S gas was prepared using 22 g of zinc sulfide (ZnS) powder and 500 mL of 6 M hydrochloric acid (HCl). Meanwhile, the meat samples were allowed to spoil for 24 and 36 hours at room temperature. The response of the sensor substrate containing the synthesized nanowires was

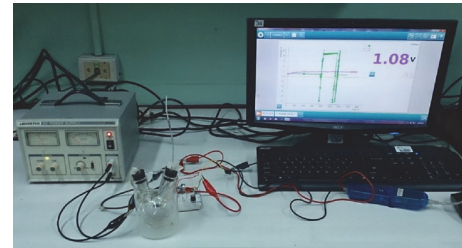


FIGURE 3: Experimental setup to test the gas sensing ability of the SnO₂ sensor substrate.

compared to the response of the substrate with nanoparticles. This is to check the sensing enhancement brought about by the 1D structure.

The headspace gas introduced to the sensor substrate was characterized by gas chromatography-mass spectrometry (GC-MS) using a 50/30 um DVB/carboxen/PDMS coating SPME fiber to absorb the gas introduced to the sensor substrate. Five (5) grams of the meat sample was placed into a flat bottom headspace vial fitted with a septum and crimp cap. The vial was heated using a water bath at 80 deg for 5 minutes. The SPME fiber (50/30 μm DVB/carboxen/PDMS coating) was preconditioned prior to analysis at 240°C for 30 min. After extraction, the SPME fiber was removed from the headspace vial and inserted directly at the injection port of the gas chromatograph. The PerkinElmer Clarus 500 Gas Chromatograph-Mass Spectrometer equipped with MS fused silica capillary column was used. The pressure was set at 43 Pa, with flow rate of 7 mL/min. Chromatographic conditions included oven temperature of 40°C for 2 min which was later increased at a rate of 5°C/min to 240°C. The mass spectrometer was used in electron impact mode with a source temperature of 200°C, ionizing voltage of 70 eV, and transfer line of 240°C. Peak identification was determined by comparison of volatile sample mass spectra with spectra in NIST/EPA/NIH Mass Spectral Database (Nat. Institute of Standards and Tech.).

3. Results and Discussion

The growth mechanism of SnO₂ nanomaterials via the HVPG technique is attributed to the vapor-liquid-solid (VLS) mechanism. The results suggested that, during the crystal growth, the SnO₂ source material, primarily located in section 1, sublimes to vapor phase and was transported to the different

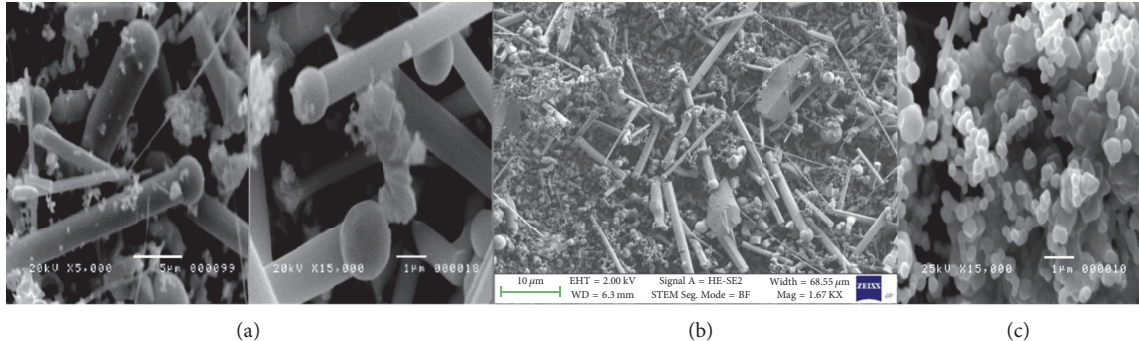


FIGURE 4: Micrographs showing the intermediate step in the formation of nanorods with spherical tips indicating their growth dynamics: (a) SEM (b) TEM, and (c) nanoparticles grown via the HVPG technique.

zones in the tube, mostly to the cooler regions of sections 2 and 3. The convective motion of the gas inside the quartz tube was greatly influenced by the thermal gradient existing along the length of the tube.

One possibility is that as the vapor moved towards section 3, it encountered the colder region section 2, where it could have undergone a phase transition from gas to liquid. It is also possible that some of the vapor interacted with the walls of the tube upon reaching section 3 and lost some of its energy, thereby condensing into liquid Sn in the process. The SnO_2 vapor would have condensed first to liquid state in section 2 and then section 3 together with the liquid Sn metal. This is observed in the intermediate step formation of nanorods (with spherical tips) in section 2 as shown in Figure 4. The Sn metal may have acted as a catalyst to assist the growth of one-dimensional structure, forming a liquid with a component of the solid phase, giving way for the formation of SnO_2 nanowires and nanorods [1, 4]. Following the periods of nucleation and incubation, a crystallite will commonly develop into a three-dimensional object with well-defined low index crystallographic faces. The growth process eventually terminates when the temperature is below the melting point, conforming to sections 2 and 3 temperatures. SnO_2 is reported to crystallize with a tetragonal rutile structure (cassiterite) wherein the tin atoms are 6 coordinates and the oxygen atoms are three coordinates [4, 7, 19].

In the absence of applied magnetic field (0 T), the diameters of the grown nanoparticles were found to increase with increasing curing time. However, there were not any nanowires formed on the substrate. With the presence of magnetic field, nanowire formation with diameter less than 100 nm was favored with a more defined structure when the magnet is farther from the furnace or at section 3b, and at greater intensity (0.31 T). Notably, a strong magnetic field intensity greatly improved the tractability of the growth of nanowires. In addition, the density of the nanowires was observed to increase in longer curing time, 8 hours, as shown in Figure 5.

On the other hand, lower magnetic field intensity, 0.25 T, was observed to produce a lower yield of nanomaterials. The length of the synthesized nanomaterials was also observed

to be shorter than those produced under the influence of a higher magnetic field intensity. A comparison of the synthesized nanostructures at varying positions where the magnetic field was applied (section 3a or section 3b), varying magnetic field intensities, and varying curing times is shown in Figure 5. It can be seen from Figure 5 that the yield of nanowires is greater when the magnet is positioned at section 3b, where the temperature is relatively cooler than that of section 3a.

To verify the influence of magnetic field on the growth of SnO_2 nanowires, the deposited structures on adjacent substrate sections (3a and 3b) were compared. As shown in Figure 6(a), nanoparticles and orthorhombic structures were grown in section 3a without an applied magnetic field. It is clear that there are no nanowires grown on the substrate. Meanwhile, in the adjacent section applied with magnetic field, high yield of nanowires was synthesized (Figure 6(b)). On the other hand, nanowires were found in section 3a applied with magnetic field (Figure 6(c)) whereas no nanowires were seen in the adjacent section (3b) without applied field (Figure 6(d)). Similarly, for the same substrate section applied with 0 T (no external magnetic field), 0.25 T, and 0.31 T magnetic field intensity, nanowires were only seen in the latter two setups. This meant that the presence of the magnetic field influenced the growth of SnO_2 nanowires.

The nanowires formed under the influence of magnetic field were found to have higher aspect ratio at higher magnetic field intensity (0.31 T) as illustrated in Figure 7. At the same magnetic field intensity, higher aspect ratio was computed when the substrate is farther from the furnace or at section 3b of the reaction tube. This means that nanowires with smaller diameter and longer lengths were formed under these conditions.

The formation of the nanowires is believed to be due to the presence of the external magnetic field, along with the presence of temperature gradient. The magnetic field exposure might have retarded the nucleation rate and accelerated the crystal growth favoring nanowire formation [13]. The particles interconnected with each other eventually forming the nanowire-like formation. The morphology enhancement of the nanowires under magnetic field is suspected to be due to thermoelectric magnetohydrodynamics as the flux

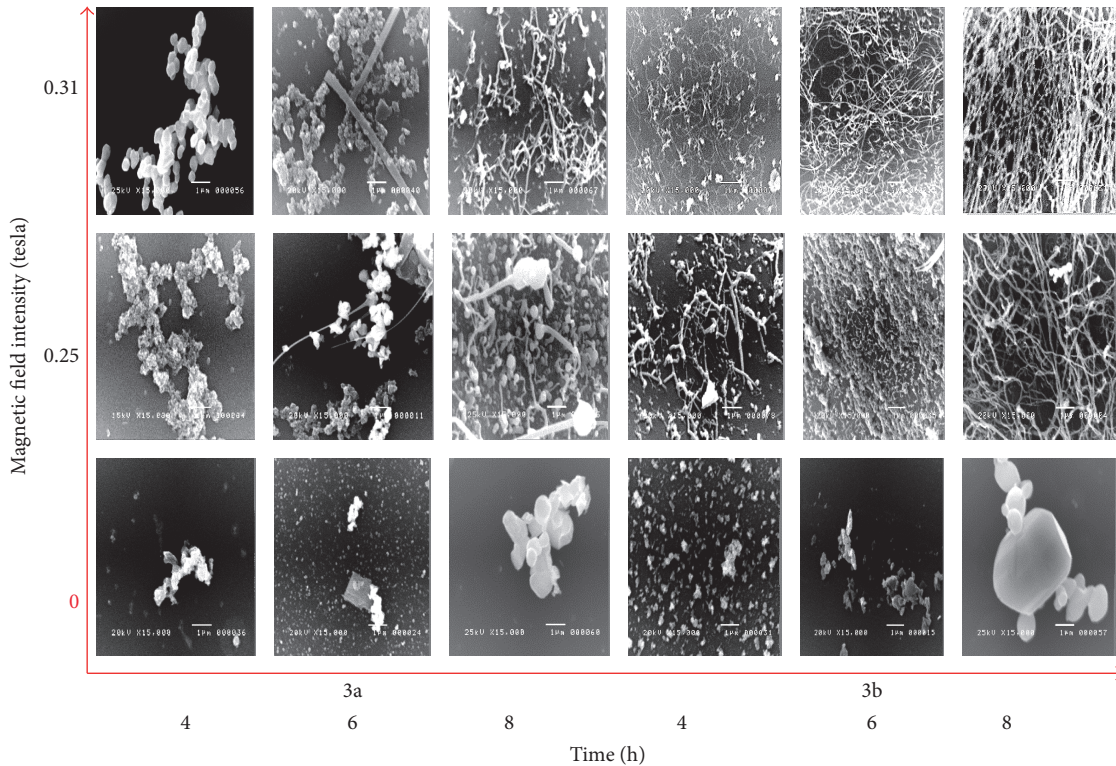


FIGURE 5: SEM micrographs ($\times 15,000$) comparing the nanostructures formed under different magnetic field intensities, substrate section where the magnetic field was applied, and curing time.

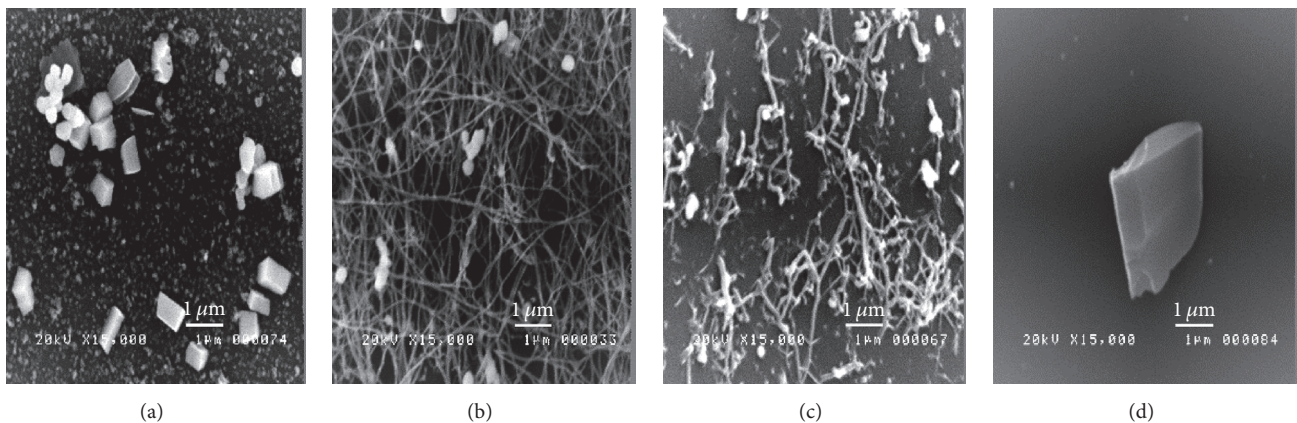


FIGURE 6: Synthesized nanostructures in adjacent sections of the substrates: (a) absence of magnet on section 3a; (b) presence of magnet on section 3b and adjacent sections, (c) presence of magnet on 3a; (d) absence of magnet on 3b.

of vaporized material interacts with the magnetic lines of force together with the presence of a temperature gradient. However, this needs further investigation.

Tin oxide is a wide gap (3.6 eV) n-type semiconductor. Reports have stated a high Seebeck coefficient ($185.38 \mu\text{V}/^\circ\text{C}$) of tin oxide thin film deposited glass substrates. Even higher coefficients were obtained when the samples were deposited with metal films such as Ag ($225.24 \mu\text{V}/^\circ\text{C}$) and Cr ($323.68 \mu\text{V}/^\circ\text{C}$) [20]. It can also be noted that other factors, such as the epitaxial orientation defined by the substrate,

have an influence on the growth direction. EDX spectroscopy confirms the presence of tin and oxygen for the tin oxide samples as shown in Figure 8.

Figure 9 exhibits the XRD pattern of the SnO_2 bulk powder source material and SnO_2 nanomaterial grown at 1200°C using the HVPG method, applied with 0.31 T external magnetic field. The SnO_2 powder has diffraction peaks at (110), (101), (200), and (211) planes which can be readily indexed with a tetragonal rutile structure with lattice constants of $a = 4.738 \text{ \AA}$ and $c = 3.187 \text{ \AA}$ based on JCPDS File

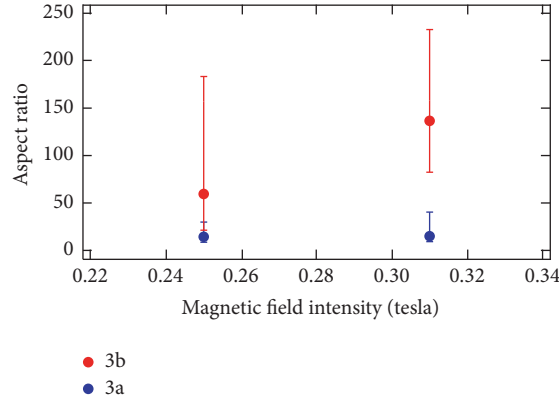


FIGURE 7: Aspect ratio of the nanowires grown under different magnetic field intensities and positions in the tube.

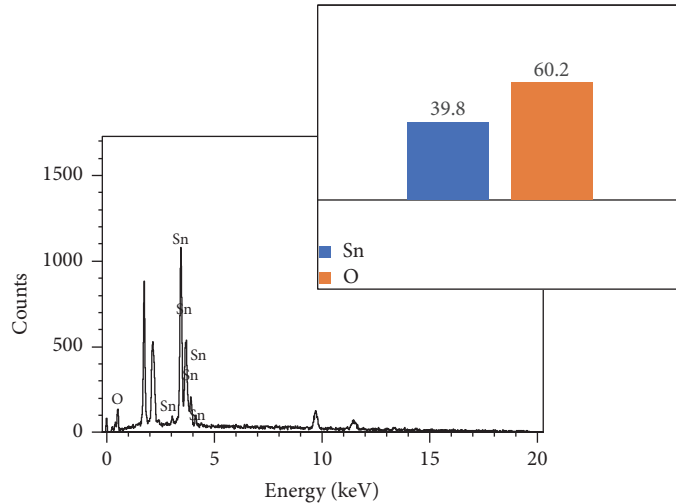


FIGURE 8: Energy dispersive X-ray spectrum of the sample indicating the presence of tin and oxygen and their atomic ratio of approximately 1:2.

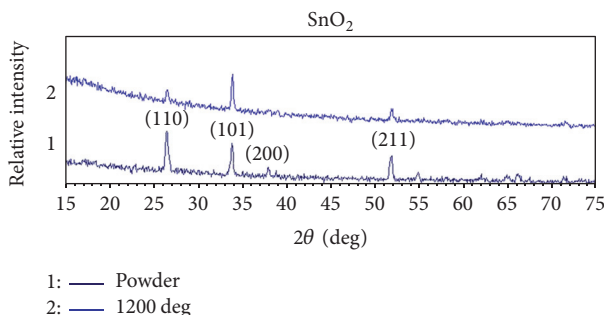


FIGURE 9: XRD pattern of SnO_2 bulk powder and SnO_2 synthesized nanowires.

number 41-1445 while the SnO_2 nanomaterial has similar diffraction peaks but low intensity peaks. This may be due to the crystallite size variations.

To determine the ability of the gas sensor substrate to detect the presence of gas analytes, the headspace gas produced by meat inside the test tube was introduced into the glass chamber. The voltage response of the sensor substrate

with the synthesized nanowires was recorded for each setup as shown in Figure 10. The said response was then compared to a sensor substrate with nanoparticles (Figure 11).

No significant change in the voltage measurements was measured upon the introduction of the fresh meat headspace (Figure 10(a)). On the other hand, an increase in the voltage reading of nearly twice the value as the baseline voltage was recorded with the introduction of the 24 h spoiled meat headspace into the chamber. As shown in Figure 10(b), the voltage measurement increased from 1.26 V to 2.39 V. A similar behavior was observed upon the introduction of the 36 h spoiled meat headspace into the chamber but with a slightly higher change in the measurement, from 1.67 V to 3.28 V (Figure 10(c)).

The meat headspace was also tested in a sensor substrate with different SnO_2 nanomaterial morphology. The nanoparticles synthesized in the substrate without external magnetic field application were used as a sensing material in the same gas extracts. Similar to the nanowires counterpart, no significant change in the voltage measurement was recorded for the fresh meat headspace; however, the baseline was found to be noisy or oscillating (Figure 11(a)). Introduction of the

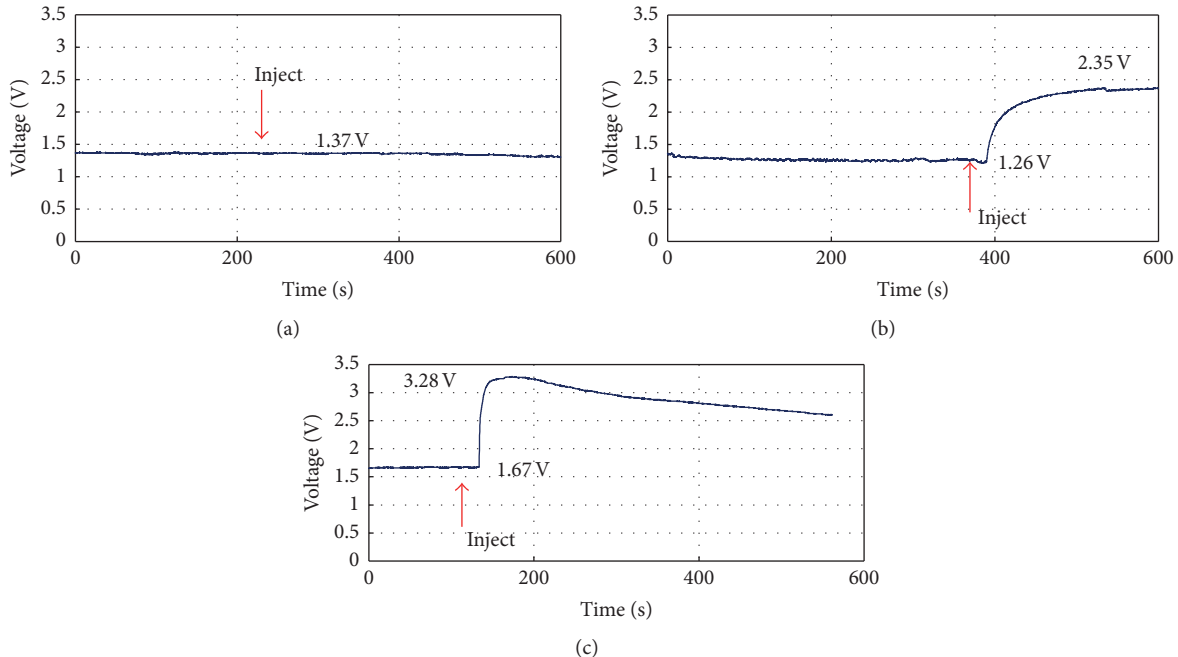


FIGURE 10: Results obtained when the gas sensing device that includes the synthesized SnO_2 nanowires electrode was used to detect headspace gas: (a) fresh meat, (b) 24 h spoiled meat, and (c) 36 h spoiled meat.

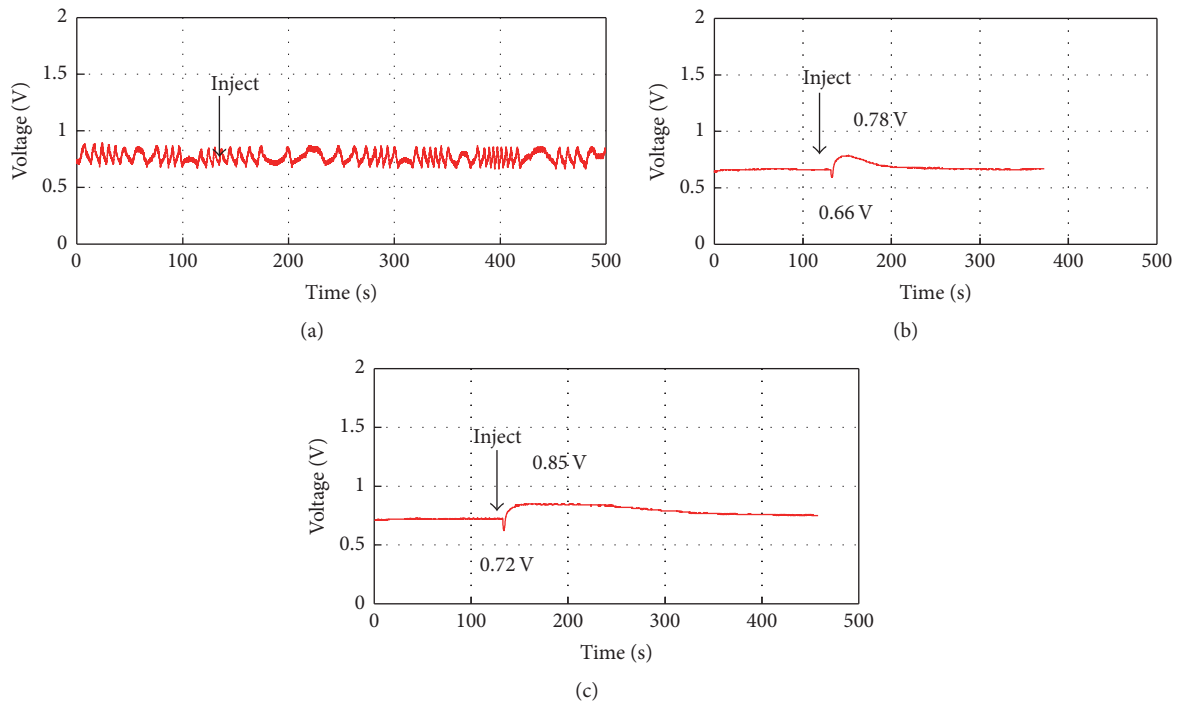


FIGURE 11: Results obtained when the gas sensing device that includes the SnO_2 nanoparticles electrode was used to detect headspace gas: (a) fresh meat, (b) 24 h spoiled meat, and (c) 36 h spoiled meat.

24-hour and 36-hour spoiled meat headspace resulted in an increase in the voltage measurement. The said increase in the voltage measurement for the 24-hour and 36-hour headspace was found to be relatively identical and smaller than the nanowire sensor response. The difference in the signal of the

former to the latter could be attributed to the higher aspect ratio of the nanowires which resulted in a greater sensitivity.

In order to determine the possible compound to which the SnO_2 sensor substrate responds, both fresh and spoiled meat samples were subjected to headspace solid

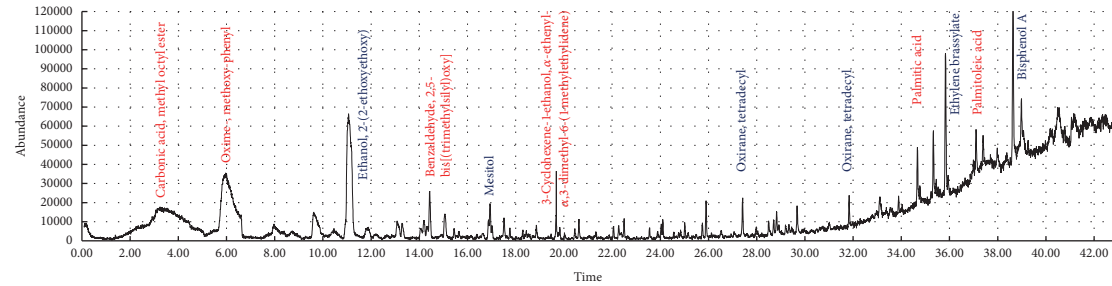


FIGURE 12: GC-MS chromatogram of fresh pork meat headspace. The elevation of the spectrum on the right is due to the high source temperature.

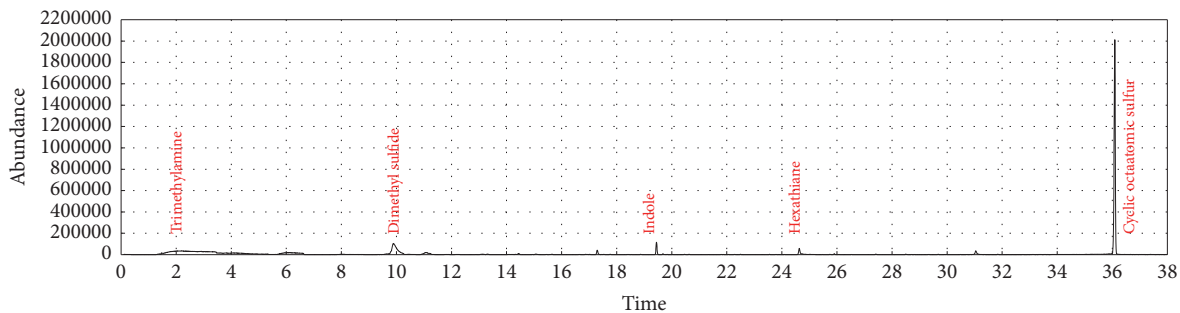


FIGURE 13: GC-MS chromatogram of 36 h spoiled pork meat headspace.

phase microextraction-gas chromatography-mass spectrometry (SPME-GC-MS). This was done to analyze the volatile compounds present in the headspace of the samples and to discriminate the gas that the fabricated sensor substrate responds to.

Mass spectrometry of the fresh meat headspace revealed strong sharp peaks for benzaldehyde, 2,5-bis[(trimethylsilyl)oxy]; 3-cyclohexene-1-ethanol, α -ethenyl- α ,3-dimethyl-6-(1-methylethylidene); and n-hexadecanoic acid (palmitic acid) as shown in Figure 12. Other compounds identified include palmitoleic acid; carbonic acid; methyl octyl ester; and oxime-, methoxy-phenyl. The sensor substrate did not show significant response to the headspace of the fresh sample and thus to its constituent compounds.

Headspace of spoiled pork was found to be largely composed of sulfur compounds with the highest abundance for cyclic octaatomic sulfur (Figure 13). This compound and hexathiane (hexasulfur) are identified to be produced by some strain of *Pseudomonas* (*Pseudomonas* spp.) and are associated with the foul odor in the spoiled meat samples [21, 22]. Aminomethanesulfonic acid and benzaldehyde, 2,5-bis[(trimethylsilyl)oxy] were also found in the samples. Other volatile compounds, in lesser abundance, identified in the pork headspace were indole (foul odor associated with spoiling meat originating from tryptophan), dimethyl sulfide (off-odor produced by organisms like *P. fragi*, *B. thermosphacta*, and *S. putrefaciens*), dimethyl trisulfide, and trimethylamine (a product of decomposition) [21].

With the sensor substrate's recorded response to the headspace of the spoiled meat, it is possible that the said sensor is responding to the sulfur compounds which were found

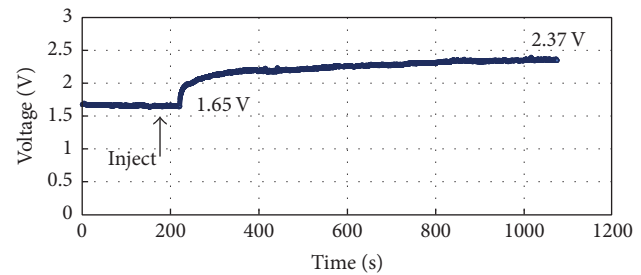


FIGURE 14: Results obtained when the gas sensing device that includes SnO₂ nanowires sensor electrode was used to detect H₂S.

to increase with increasing time of spoilage. A reference test was then conducted using hydrogen sulfide (H₂S) as the gas analyte.

Similar to the response of the sensor substrate to the headspace of spoiled meat, an increase in voltage measurement of about 0.7 V was recorded with the introduction of 1 cm³ of H₂S gas into the chamber (Figure 14). Succeeding trials showed the same pattern of response. Compared to the sensor substrate of a different morphology, the nanoparticle sensor gives out a small increase in voltage as compared to the synthesized nanowires counterpart (Figure 15). The difference in the signal of the nanowire sensor to the nanoparticle sensor could be attributed to the higher aspect ratio of the former leading to its sensitivity enhancement.

The sensor substrates' response to ethanol and methanol vapors was also explored. Ethanol and methanol are among the volatile compounds produced from bacterial metabolism

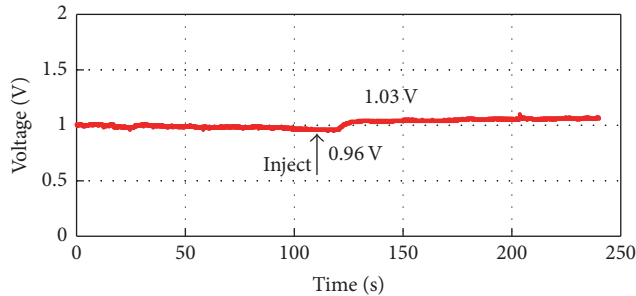


FIGURE 15: Results obtained when the gas sensing device that includes SnO_2 nanoparticles sensor electrode was used to detect H_2S .

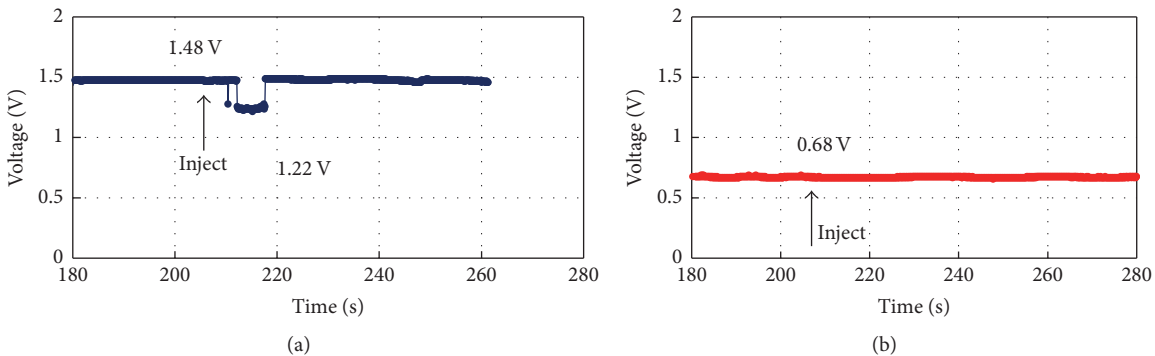


FIGURE 16: Results obtained when the gas sensing device that includes SnO_2 gas sensor electrode was used to detect ethanol vapor: (a) nanowires, (b) nanoparticles.

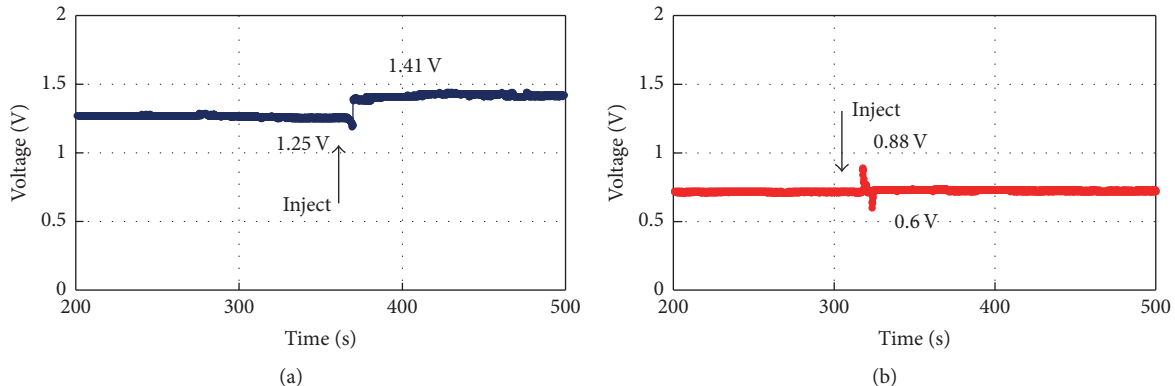


FIGURE 17: Results obtained when the gas sensing device that includes SnO_2 gas sensor electrode was used to detect methanol: (a) nanowires, (b) nanoparticles.

in meat [21, 23, 24]. A decrease in the voltage measurement was observed upon the introduction of the ethanol vapor to the synthesized nanowire sensor substrate (Figure 16(a)); meanwhile, no significant response was recorded for the nanoparticle sensor substrate. Ethanol is reported to be a reducing gas which could possibly explain the decrease in resistance or the voltage reading in the sensor substrate [25].

On the other hand, a successive decrease and increase in the voltage measurement were noted for the nanowire sensor while an increase and then a decrease in reading were observed in the nanoparticles sensor substrate upon

the introduction of methanol gas (Figure 17). Corresponding results were observed in the repeated trials.

The trapping of electrons at adsorbed molecules and band bending induced by these charged molecules are identified as the reasons for the change in the resistivity. The sensing reaction to the H_2S gas or the sulfur compounds found in the meat headspace is believed to occur only on the surface of the sensing material. The application of magnetic field to the synthesis of nanomaterials could have increased its defects, that is, oxygen vacancy which may have resulted in improved sensitivity. A charge depletion layer can be formed

near the grain surface of SnO_2 in an oxidizing atmosphere. The electrons associated with these are drawn from the conduction band of the material leading to an increase in resistance. Given a constant current, this results in the increase in voltage measurement [5, 26].

4. Conclusions

The presence of the magnetic field, along with the presence of temperature gradient, was found to be responsible for the formation of the homogenized nanowires. However, the temperature gradient is believed to be a primary influence as compared to the applied magnetic field intensity on the growth of the nanowire. We found that length of nanowires was significantly enhanced by the application of magnetic field. The aspect ratio, as well as the density of the synthesized nanowires, increased with increasing magnetic field. Thermoelectric magnetohydrodynamics is suspected to be the mechanism for the formation of nanowires but this needs to be validated.

As a proof of concept, the fabricated SnO_2 sensor substrate was found to be more responsive to gaseous sulfur compounds and has potential application in meat spoilage evaluation and H_2S detection.

Conflicts of Interest

The authors declare that there are no conflicts of interest regarding the publication of this paper.

Acknowledgments

The authors would like to express their appreciation to the i-Nano Lab graduate students, staff of the Surface Physics Laboratory, the DLSU College of Science, the DLSU VCRI office, the DOST-SEI-ASTHRDP, and Carl Zeiss Singapore for the TEM micrographs.

References

- [1] R. De Los and G. N. Santos, "Growth mechanism of SnO_2 nano-materials derived from backscattered electron image and Edx observations," *International Journal of Scientific & Engineering Research*, vol. 2, no. 12, 2011.
- [2] A. Kolmakov and M. Moskovits, "Chemical sensing and catalysis by one-dimensional metal-oxide nanostructures," *Annual Review of Materials Research*, vol. 34, pp. 151–180, 2004.
- [3] E.-S. M. A. Duraia, Z. A. Mansorov, and S. Tokmolden, "Synthesis, characterization and photoluminescence of tin oxide nanoribbons and nanowires," *Physica B: Condensed Matter*, vol. 404, no. 21, pp. 3952–3956, 2009.
- [4] S. Das and V. Jayaraman, " SnO_2 : a comprehensive review on structures and gas sensors," *Progress in Materials Science*, vol. 66, pp. 112–255, 2014.
- [5] M. Batzill and U. Diebold, "The surface and materials science of tin oxide," *Progress in Surface Science*, vol. 79, no. 2-4, pp. 47–154, 2005.
- [6] D. M. De Mesa, G. N. Santos, and R. V. Quiroga, "Synthesis and characterization of Fe_2O_3 nanomaterials using Hvpc growth technique for glucose sensing application," *International Journal of Scientific & Engineering Research*, vol. 3, no. 8, 2012.
- [7] G. Cao, *Nanostructures & Nanomaterials: Synthesis, Properties & Applications*, Imperial College Press, 2004.
- [8] A. Johari, M. C. Bhatnagar, and V. Rana, "Growth, characterization and I-V characteristics of tin oxide (SnO_2) nanowires," *Advanced Materials Letters*, vol. 3, no. 6, pp. 515–518, 2012.
- [9] M. Salavati-Niasari, N. Mir, and F. Davar, "Synthesis, characterization and optical properties of tin oxide nanoclusters prepared from a novel precursor via thermal decomposition route," *Inorganica Chimica Acta*, vol. 363, no. 8, pp. 1719–1726, 2010.
- [10] M. A. Batal, G. J. Nashed, and J. Fares Haj, "Electrical properties of nanostructure tin oxide thin film doped with copper prepared by Sol-Gel method," *Latin-American Journal of Physics Education*, vol. 6, no. 2, pp. 311–316, 2012.
- [11] G. N. C. Santos, A. A. Salvador, and R. V. Quiroga, "Temperature and deposition time dependence of the geometrical properties of tin oxide nanostructures," *International Journal of Scientific & Engineering Research*, vol. 2, no. 10, 2011.
- [12] G. Jiménez-Cadena, J. Riu, and F. X. Rius, "Gas sensors based on nanostructured materials," *Analyst*, vol. 132, pp. 1083–1099, 2007.
- [13] T. R. Bastami and M. H. Entezari, "Synthesis of manganese oxide nanocrystal by ultrasonic bath: effect of external magnetic field," *Ultrasonics Sonochemistry*, vol. 19, no. 4, pp. 830–840, 2012.
- [14] A. B. Freitas, F. G. Landgraf, M. M. Seckler, and M. Giulietti, "The influence of magnetic field on crystallization from solutions," in *Proceedings of the International Conference of Industrial Crystallization*, Cambridge, UK, September 1999.
- [15] M. Sacidi, M. Vaezzadeh, and M. Mansouri, "Influence of AC magnetic field on phonon vibrations of superparamagnetic cluster sitting at tip end of ultra-long carbon nanotube," *Journal of Crystal Growth*, vol. 345, no. 1, pp. 7–10, 2012.
- [16] R. P. Ji, J. S. Jiang, and M. Hu, "How does the distribution of external magnetic lines of force influence the growth of ferromagnetic material?" *Journal of Physical Chemistry*, vol. 114, no. 28, pp. 12090–12094, 2010.
- [17] N. El Barri, E. Llobet, N. El Bari, X. Correig, and B. Bouchikhi, "Electronic nose based on metal oxide semiconductor sensors as an alternative technique for the spoilage classification of red meat," *Sensors*, vol. 8, no. 1, pp. 142–156, 2008.
- [18] Z. Li and K. Suslick, "Portable optoelectronic nose for monitoring meat freshness," *ACS Sensors*, vol. 1, no. 11, pp. 1330–1335, 2016.
- [19] A. Ansari, P. Solanki, A. Kaushik, and B. Malhotra, "Recent advances in nano-structured metal oxides based electrochemical biosensors for clinical diagnostics," in *Nanostructured Materials for electrochemical biosensors*, NOVA, New York, NY, USA, 2009.
- [20] S. Anuradha and K. Rajanna, "A novel method for the improvement in thermoelectric property of tin oxide thin films and its application in gas sensing," *International Journal on Smart Sensing and Intelligent Systems*, vol. 1, no. 2, pp. 498–511, 2008.
- [21] J. Jay, *Modern Food Microbiology*, Aspen Publication, Frederick, Md, USA, 6th edition, 2000.
- [22] D. Mayr, R. Margesin, E. Klingsbichel et al., "Rapid detection of meat spoilage by measuring volatile organic compounds by using proton transfer reaction mass spectrometry," *Applied and Environmental Microbiology*, vol. 69, no. 8, pp. 4697–4705, 2003.

- [23] A. Argyri, A. Mallouchos, E. Panagou, and G. Nychas, "The dynamics of the HS/SPME-GC/MS as a tool to assess the spoilage of minced beef stored under different packaging and temperature conditions," *International Journal of Food Microbiology*, vol. 193, pp. 51–58, 2015.
- [24] F. Leroy, C. Vasilopoulus, S. Hemelryk, G. Falony, and L. De Vuyst, "Volatile analysis of spoiled, artisan-type, modified-atmosphere-packaged cooked ham stored under different temperatures," *Food Microbiology*, pp. 94–102, 2009.
- [25] A. Loutfi, S. Coradeschi, G. Mani, P. Shankar, B. Rayappan, and J. Bosco, "Electronic noses for food quality: a review," *Journal of Food Engineering*, vol. 144, pp. 103–111, 2015.
- [26] J. Liu, X. Huang, G. Ye, L. Wei, Z. Jiao, W. Chao et al., "H₂S detection sensing characteristic of CuO/SnO₂ sensor," *Sensors*, vol. 2, pp. 110–118, 2003.

Research Article

Investigating Visible-Photocatalytic Activity of MoS₂/TiO₂ Heterostructure Thin Films at Various MoS₂ Deposition Times

Hang Nguyen Thai Phung,^{1,2} Van Nguyen Khanh Tran,¹ Lam Thanh Nguyen,¹ Loan Kieu Thi Phan,¹ Phuong Ai Duong,¹ and Hung Vu Tuan Le¹

¹*Ho Chi Minh City University of Science, Ho Chi Minh City, Vietnam*

²*Tay Nguyen University, Buon Ma Thuot City, Daklak Province, Vietnam*

Correspondence should be addressed to Hang Nguyen Thai Phung; pnthang@ttn.edu.vn

Received 1 March 2017; Revised 24 April 2017; Accepted 7 May 2017; Published 15 June 2017

Academic Editor: Weilu Gao

Copyright © 2017 Hang Nguyen Thai Phung et al. This is an open access article distributed under the Creative Commons Attribution License, which permits unrestricted use, distribution, and reproduction in any medium, provided the original work is properly cited.

MoS₂/TiO₂ heterostructure thin films were fabricated by sol-gel and chemical bath deposition methods. Crystal structure, surface morphology, chemical states of all elements, and optical property of the obtained thin films were characterized by using X-ray diffraction, scanning electron microscopy, X-ray photoelectron spectroscopy, and UV-Vis spectroscopy techniques, respectively. Photocatalytic activity of all thin films was evaluated by measuring decomposition rate of methylene blue solution under visible light irradiation. The results indicate that ultrathin MoS₂ film on TiO₂-glass substrate improves photocatalytic activity of TiO₂ in the visible light due to the efficient absorption of visible photon of MoS₂ few layers and the transfer of electrons from MoS₂ to TiO₂. All MoS₂/TiO₂ heterostructure thin films exhibit higher visible light photocatalytic activity than that of pure MoS₂ and TiO₂ counterparts. The best MoS₂/TiO₂ heterostructure thin film at MoS₂ layer deposition time of 45 minutes can decompose about 60% MB solution after 150 minutes under visible light irradiation. The mechanism of the enhancement for visible-photocatalytic activity of MoS₂/TiO₂ heterostructure thin film was also discussed.

1. Introduction

TiO₂ with a large band-gap semiconductor (3.0 eV for rutile and 3.2 eV for anatase) has been widely applied in solar energy conversion and environmental purification, such as TiO₂-based photocatalysts and dye-sensitized solar cells [1, 2]. However, due to its large band-gap, TiO₂ can only absorb ultraviolet (UV) light which accounts for only 5% of the solar energy, so some applications of TiO₂ have been limited to the ultraviolet light region [3]. Therefore, it is necessary to improve the photocatalytic activity of TiO₂ under visible light irradiation (~45% of sun energy).

There have been some approaches to be used to improve photocatalytic performance of TiO₂ under visible light, such as doping or semiconductor coupling (TiO₂-based heterostructures). Impurity doping is one of the typical approaches [4–8]. However, doping can usually cause high recombination rate and the low carries mobility of photoexcited electron-hole pairs and make TiO₂ thermally unstable [9].

Semiconductor coupling has been receiving much attention recently. By coupling between TiO₂ and a smaller band-gap semiconductor with matched edge-energy levels, electrons can transfer from semiconductor to TiO₂, which makes a shift of TiO₂'s photocatalytic activity from UV light to visible light. The prerequisite for these semiconductors is that their conduct band minimum has to be more positive than that of TiO₂ [10–12].

Recently, layered molybdenum disulfide (MoS₂) has attracted much attention due to its unique electrical and optical properties. Monolayer MoS₂ is a direct band-gap of 1.9 eV and multilayer/bulk MoS₂ is a 1.2 eV indirect band-gap [13]. The band-gap of MoS₂ ultrathin film matches the solar spectrum absorption closely and its stability against photo-corrosion [14]. Furthermore, the conduction band minimum of MoS₂ ultrathin film is higher than that of TiO₂, so in the heterostructure of MoS₂/TiO₂, electrons from excited band-gap of MoS₂ thin film can inject efficiently into TiO₂ under

visible light [15, 16]. Therefore, MoS_2 is considered either a photo-sensitizer for visible light or an electron transfer mediator in the heterogeneous semiconductor systems [17].

Until now, there have just been few reports on $\text{MoS}_2/\text{TiO}_2$ in composites, nanopowder or core-shell materials for photocatalytic performance under visible light. For example, Kanda et al. fabricated $\text{MoS}_2/\text{TiO}_2$ photocatalyst applied in hydrogen generation [16]. According to Zhou et al., the $\text{MoS}_2/\text{TiO}_2$ heterostructure with 50 wt% MoS_2 exhibits the highest hydrogen production [18]. Zhou et al. deposited MoS_2 thin film layer on TiO_2 nanotubes and the sample with 1 nm thickness of MoS_2 exhibited the strongest H_2 evolution activity [17]. Zhang et al. used mild impregnation method to assemble exfoliated MoS_2 shell on anatase TiO_2 mesocrystal; their photocatalyst had high H_2 evolution rate of $0.55 \text{ mmol h}^{-1} \text{ g}^{-1}$ and good reusability under UV light [19]. Zhang et al. employed ultrasonic-hydrothermal method to synthesize $\text{TiO}_2/\text{MoS}_2$ @zeolite composite photocatalyst which highly enhanced photocatalytic activity for degradation of methyl orange under solar-light irradiation [20]. However, researches have been rarely studied for $\text{MoS}_2/\text{TiO}_2$ heterostructure thin film. The important advantages of photocatalytic thin film over powder are its reusability and recovery. In this study, we fabricated $\text{MoS}_2/\text{TiO}_2$ heterostructure thin film by sol-gel and chemical bath deposition methods. The relationship between physical properties and photocatalytic activity was discussed in detail. Methylene blue dye was selected as a model reactant for photodegradation.

2. Experiment

The $\text{MoS}_2/\text{TiO}_2$ (MT) heterostructure thin films were fabricated by a combination of sol-gel and chemical bath deposition methods.

First, TiO_2 thin films were prepared on glass substrates by using dip coating process. The details of the procedure for making the TiO_2 samples have been described in our previous work [21]. Tetrabutyl orthotitanate (Ti(OBu)_4) (99.99%) was dissolved in a mixture solution of diethanolamine ($\text{HN}(\text{C}_2\text{H}_4\text{OH})_2$) (99.99%) and ethanol ($\text{C}_2\text{H}_5\text{OH}$) (99.99%). Then distilled water was added dropwise with continuous stirring for 2 hours to get TiO_2 sol solution. We used glass plates as the substrates which were dip-coated in the above sol to obtain TiO_2 films. These films were dried at 80°C for 15 minutes and were annealed at 500°C for 2 hours in the air.

Second, we synthesized MoS_2 ultrathin film on TiO_2 thin film via chemical bath deposition method. Thiourea ($\text{CS}(\text{NH}_2)_2$) and ammonium paramolybdate ($(\text{NH}_4)_6\text{Mo}_7\text{O}_{24} \cdot 4\text{H}_2\text{O}$) were alternately added to deionized water under continuous stirring for 90 minutes to form a homogeneous solution. In addition, hydrazine hydrate (35 wt%) was added to the above mixture solution with vigorous stirring for 10 minutes. Inside the chemical bath, we inserted glass substrate which was coated TiO_2 thin film to grow MoS_2 ultrathin film. This bath was kept at 80°C for different deposition time of MoS_2 layer (15, 30, 45, and 60 minutes). After chemical bath deposition process, the bath was cooled down to room temperature naturally. A MoS_2 ultrathin film was deposited onto TiO_2 thin film, which was

washed in the ultrasonic cleaner with distilled water to get rid of heterogeneities and then dried at room temperature. Finally, the obtained products were annealed at 500°C for 2 hours under continuous flow of nitrogen gas. The MT heterostructure thin films at various MoS_2 layer deposition times correspond to different thicknesses of MoS_2 films on the TiO_2 -glass substrates.

All obtained samples include pure TiO_2 and series of $\text{MoS}_2/\text{TiO}_2$ heterostructure thin films at various MoS_2 layer deposition times of 15, 30, 45, and 60 minutes, which were labeled as TiO_2 , MoS_2 , MT15, MT30, MT45, and MT60, respectively. Pure MoS_2 sample at 45-minute deposition time and pure TiO_2 counterparts were prepared and denoted as MoS_2 and TiO_2 to compare with others.

The morphologies of samples were observed by scanning electron microscopy (SEM, Hitachi S-4800). Crystal structure of the samples was examined by X-ray diffraction (Bruker D8 Advance) using $\text{CuK}\alpha$ from $2\theta = 10\text{--}70^\circ$. Optical absorption spectra of films were measured at room temperature in the air using a Halo RB-10 spectrophotometer. Degradation rate of methylene blue (MB) was measured to evaluate the photocatalytic activity of obtained thin films. Every $25 \times 25 \text{ mm}^2$ film was dipped into 10 ml of 10 ppm MB solution with a pH of about 4.72. In the absence and presence of catalysts, MB solution was stored in dark for 30 minutes before irradiation to attain adsorption-desorption equilibrium. A compact light was used as a visible light source in this experiment. MB adsorptions at 662 nm were measured by a Halo RB-10 spectrophotometer at intervals of 30 minutes. We used Lambert-Beer's law to calculate the changes of MB concentration at regular irradiation intervals.

3. Results and Discussion

Figure 1 illustrates MB solution photodegradation by visible light irradiation catalyzed by TiO_2 , MoS_2 , and series of MT thin films at various MoS_2 layer deposition times. From Figure 1, it is clearly observed that TiO_2 thin film has a negligible MB photodegradation in visible light region, which can be originated from its UV light absorption. Meanwhile, we found that pure MoS_2 thin films have MB degradation of 30% within 150 minutes in visible light irradiation. This indicates that MoS_2 sample has a relatively low visible-photocatalytic activity which is explained by high recombination rate of electron-hole pairs. Furthermore, MT15 sample apart, the remaining MT thin films have higher photocatalytic performance in visible band compared with that of TiO_2 or MoS_2 . This enhancement can be explained by the efficient visible light absorption of MoS_2 and the transfer of electrons from MoS_2 to TiO_2 in $\text{MoS}_2/\text{TiO}_2$ heterostructure thin films; from that, it decreases the recombination rate of electron-hole pairs and increases the photocatalytic activity in the visible light region.

In particular, photodegradation rates of MT15 and TiO_2 samples are relatively the same. This could be explained that MoS_2 layer did not exist on surface of MT15. According to Nair et al., in CBD procedure, there is a nucleation period which established various chemical equilibria to prepare for forming MoS_2 layer. Deposition time of 15 minutes is not

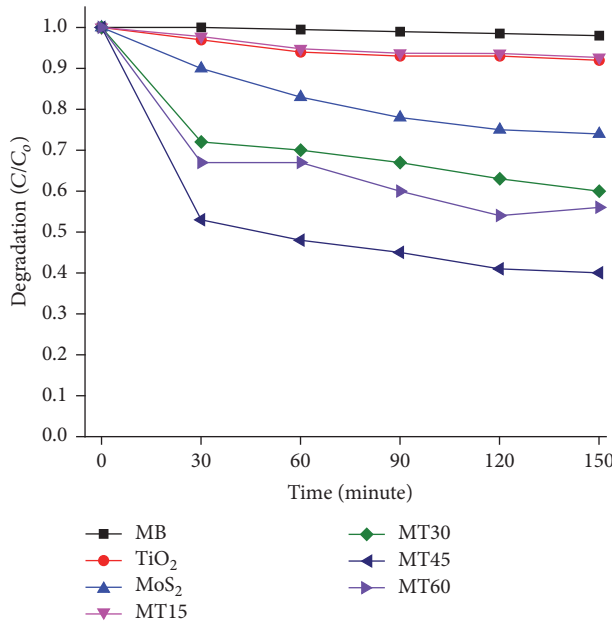


FIGURE 1: The photodegradation of MB solution for MoS₂, TiO₂, and series of MT thin films at different deposition time of MoS₂ under visible light irradiation.

long enough for growth of initial MoS₂ molecules [22]. Thus, it takes more than 15 minutes to form some early MoS₂ molecules on a surface of the substrate.

As demonstrated in Figure 1, MT45 exhibits the highest visible-photocatalytic activity compared to any of the remaining MT samples. Its degradation of MB solution reaches as high as 60% with 150 minutes. For MT30 sample, its thickness can be insufficient to absorb visible light. With MT60, the thickness is more. According to Nair et al. [22], following the nucleation period of CBD process, film growth rate is relatively large, and the number of monolayers of MT60 increases significantly. So its band-gap energy is reduced in which its conduction band bottom lies lower than that of TiO₂, which prevents photoexcited electrons from transferring to TiO₂ [14, 15]. In summary, MT45 sample has the highest visible-photocatalytic activity.

Figure 2 shows UV-Vis absorption spectra of TiO₂, MoS₂, and series of MT thin films. It can be seen that pure TiO₂ has an absorption edge of 380 nm corresponding to a band-gap energy of 3.2 eV, so TiO₂ is only active in UV light region. MoS₂ sample has strong absorption in visible light. Its band-gap energy was calculated from UV-Vis absorption spectrum using Tauc plot method and it was found to be approximately 1.87 eV as in the inset of Figure 2. After coating MoS₂ thin film onto TiO₂/glass substrates, all MT samples have an increase in the absorption of visible light except for MT15. This is attributed to narrow band-gap and dark color of MoS₂ nanosheets, which is beneficial to the visible-photocatalytic activity. In comparison with TiO₂, MT15 sample has relatively the same UV-Vis spectrum, so it confirmed that MoS₂ did not exist on its surface.

The XRD patterns of MoS₂, TiO₂, and MT45 sample are shown in Figure 3.

With pure TiO₂ thin film, diffraction peaks are observed at 25.2°, 37.8°, 48.1°, and 54.3° indexed as (101), (004), (200), and (211) plane lattices, assigned to the anatase phase of TiO₂, respectively [Anatase XRD JCPDS card number 78-2486].

As for pure MoS₂ sample, the two detected peaks at 2θ values of 14.4° and 32.7° can be assigned to the (002) and (100) planes of hexagonal phase MoS₂ ($a = b = 0.316$ nm, $c = 1.230$ nm, JCPDS card number 37-1492). The diffraction peak at 14.4° is corresponding to the *c*-plane of MoS₂ and can be used to study the structure of MoS₂, which is composed of Mo atoms coordinated with S atoms to form the S-Mo-S sandwich layer. The intensity of this peak is not high; it indicates that the MoS₂ nanosheets may have only few layers.

Interestingly, all of the diffraction peaks which are assigned for phases of TiO₂ and MoS₂ exist in XRD of MT45 sample. But the intensities of these diffraction peaks decrease and the peaks assigned to MoS₂ shift slightly to the right. These shifts could be the results from the distinct pressure stress on MoS₂ when MoS₂ nanosheets grow on TiO₂ thin film. So, it is said that TiO₂ might prevent the growth of MoS₂ crystals along the *c*-axis.

We estimated the thickness of the film with the SEM image taken in cross-section mode. Figure 4 shows the cross-sectional SEM image of MT45 sample. It is seen that the ultrathin MoS₂ layer is uniformly coated on TiO₂ thin film. The result exhibits the thicknesses of MoS₂ layer and MoS₂/TiO₂ thin films are approximately 12 nm and 245 nm, respectively. The 12 nm thickness of MoS₂ nanosheets could be the best appropriate thickness to cover on TiO₂ thin film and agrees with schematic illustration of charge-transfer of MoS₂/TiO₂ heterostructure thin film as followed.

X-ray photoelectron spectroscopy (XPS) is used to further clarify the structure of MT45 sample. As shown in Figure 5(a), the Mo⁴⁺ shows two peaks centered at 229 eV and 232 eV, attributing to the Mo 3d_{5/2} and Mo 3d_{3/2}, respectively. Furthermore, there is the small peak at 235.5 eV which indicates the residuals of Mo⁶⁺. For S 2p, there are two peaks consisting of S 2p_{3/2} and S 2p_{1/2} which are centered at 161.9 eV and 163.1 eV, respectively (as shown in Figure 5(b)). Two 2p_{3/2} and 2p_{1/2} peaks of Ti²⁺ were seen at 466 eV and 471 eV in Figure 5(c). The O 1s spectrum shows a peak at 537 eV in Figure 5(d). All the XPS positions of peaks are consistent with the reported values [19]. So there is the existence of Mo⁴⁺ (Mo 3d_{5/2} orbital and Mo 3d_{3/2} orbital), S²⁻ (S 2p_{3/2} orbital and S 2p_{1/2} orbital), Ti²⁺ (Ti 2p_{3/2} orbital and Ti 2p_{1/2}), and O²⁻ (O 1s orbital) in MT45 film. This result indicates that we have successfully fabricated the MoS₂/TiO₂ heterostructure thin film.

A schematic illustration for the photogenerated electron-hole separation and transfer process between MoS₂ and TiO₂ in TiO₂/MoS₂ heterostructure thin film is displayed in Figure 6.

The proposed mechanism for an enhanced photocatalytic activity in the TiO₂/MoS₂ heterostructure thin film under visible light irradiation assumes that the photoexcited electrons are transferred from the conduction band of MoS₂ thin film to the TiO₂ and eventually react with oxygen to produce superoxide anion radical [15]. Simultaneously, some

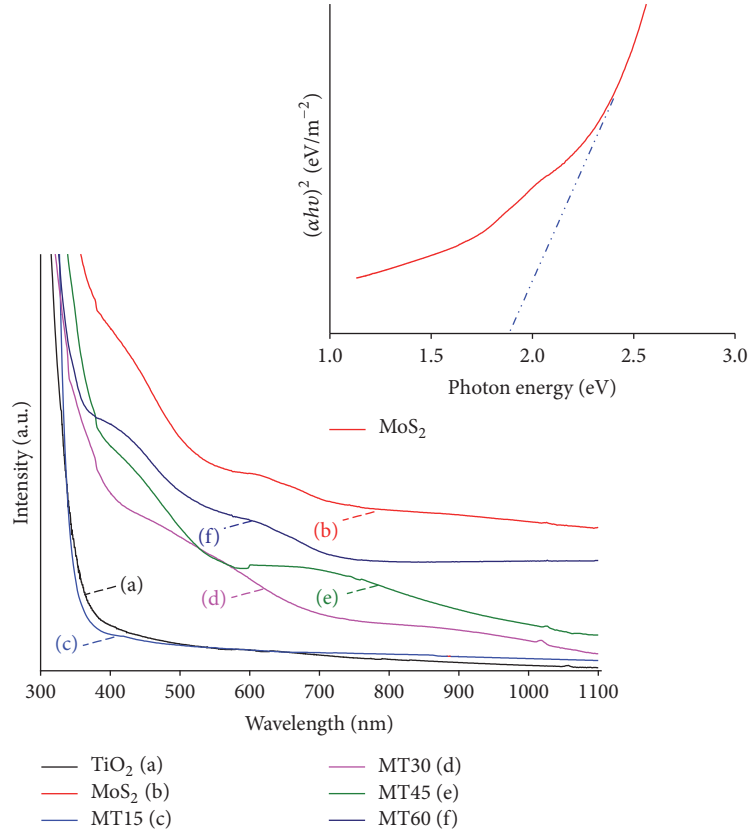


FIGURE 2: UV-visible absorption spectra of MoS_2 , TiO_2 , and series of MT thin films at different deposition time of MoS_2 under visible light irradiation. The inset of the figure: Tauc plot for MoS_2 thin film.

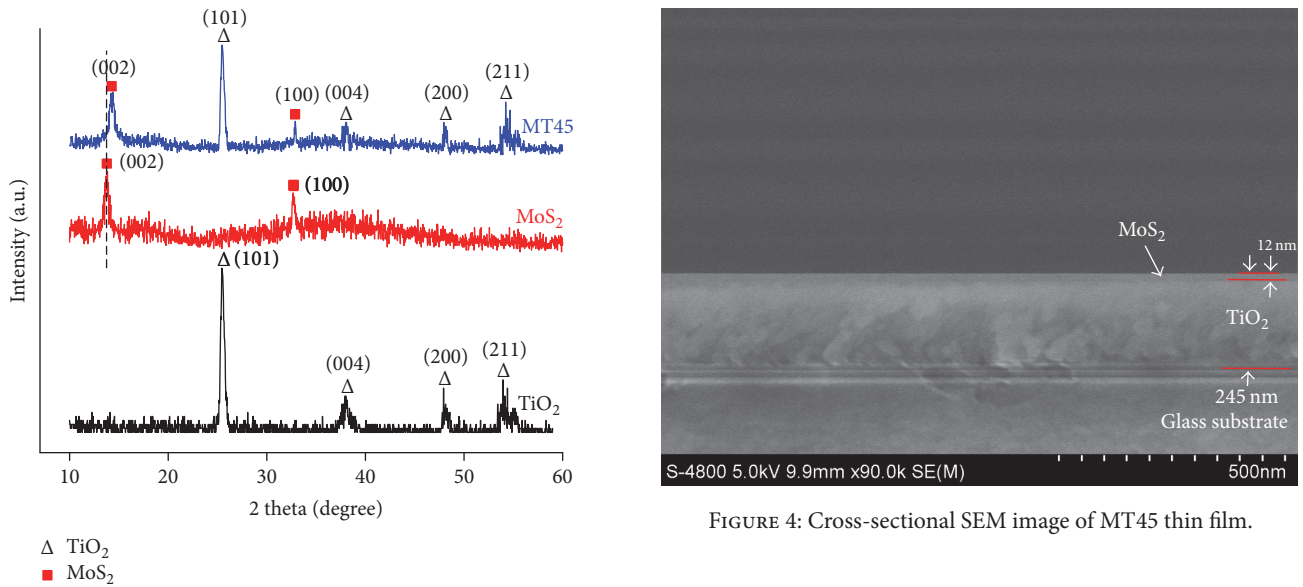


FIGURE 3: XRD pattern of pure MoS_2 , pure TiO_2 , and MT45 thin films.

holes move from the valence band of TiO_2 to the valence band of MoS_2 and MB solution is degraded. Consequently, $\text{MoS}_2/\text{TiO}_2$ heterostructure thin film can absorb visible light efficiently and supply more reaction active sites, leading to the superior photocatalytic activity.

4. Conclusion

$\text{MoS}_2/\text{TiO}_2$ heterostructure thin films have been successfully prepared by combination of sol-gel and chemical bath deposition methods. The results show that coating ultrathin onto TiO_2 -glass substrate enhances photocatalytic activity under visible light. The mechanism for the improved photocatalytic activity in the $\text{MoS}_2/\text{TiO}_2$ heterostructure thin film

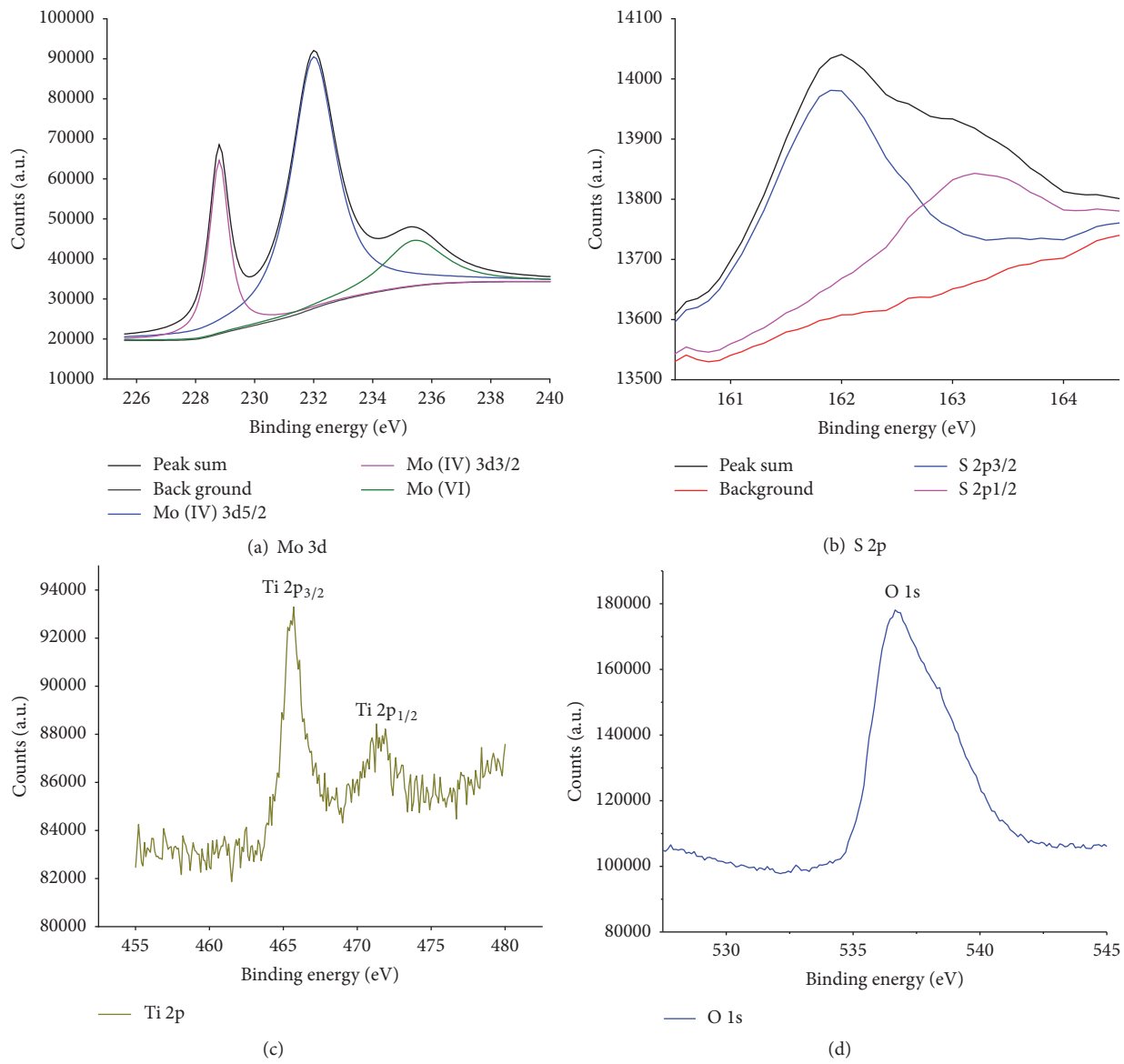


FIGURE 5: XPS spectra of MT45 thin film.

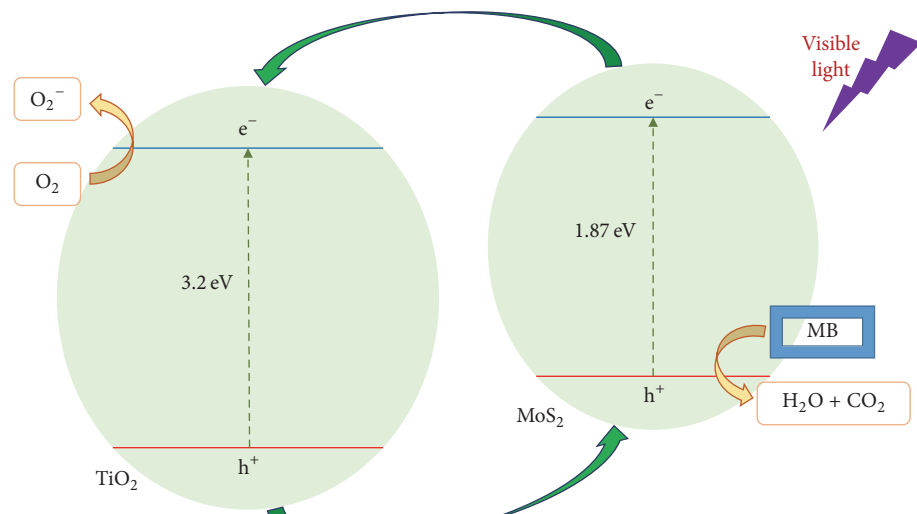


FIGURE 6: Schematic illustration of charge-transfer of MT heterostructure thin film for photocatalytic activity in the visible light.

is discussed in detail. The MoS₂/TiO₂ heterostructure thin film at 45-minute deposition time of MoS₂ layer shows the best visible-photocatalytic activity with MB photodegradation rate about 60% after 150 minutes under compact light irradiation.

Conflicts of Interest

The authors declare that there are no conflicts of interest regarding the publication of this paper.

References

- [1] A. Fujishima and X. Zhang, "Titanium dioxide photocatalysis: present situation and future approaches," *Comptes Rendus Chimie*, vol. 9, no. 5-6, pp. 750–760, 2006.
- [2] U. Diebold, "The surface science of titanium dioxide," *Surface Science Reports*, vol. 48, no. 5–8, pp. 53–229, 2003.
- [3] P. Bouras, E. Stathatos, and P. Lianos, "Pure versus metal-ion-doped nanocrystalline titania for photocatalysis," *Applied Catalysis B: Environmental*, vol. 73, no. 1-2, pp. 51–59, 2007.
- [4] A. di Paola, G. Marci, L. Palmisano et al., "Preparation of polycrystalline TiO₂ photocatalysts impregnated with various transition metal ions: characterization and photocatalytic activity for the degradation of 4-nitrophenol," *The Journal of Physical Chemistry B*, vol. 106, no. 3, pp. 637–645, 2002.
- [5] M.-S. Kim, G. Liu, W. K. Nam, and B.-W. Kim, "Preparation of porous carbon-doped TiO₂ film by sol-gel method and its application for the removal of gaseous toluene in the optical fiber reactor," *Journal of Industrial and Engineering Chemistry*, vol. 17, no. 2, pp. 223–228, 2011.
- [6] H. Tian, J. Ma, K. Li, and J. Li, "Hydrothermal synthesis of S-doped TiO₂ nanoparticles and their photocatalytic ability for degradation of methyl orange," *Ceramics International*, vol. 35, no. 3, pp. 1289–1292, 2009.
- [7] E. A. Reyes-Garcia, Y. Sun, K. Reyes-Gil, and D. Raftery, "¹⁵N solid state NMR and EPR characterization of N-doped TiO₂ photocatalysts," *Journal of Physical Chemistry C*, vol. 111, no. 6, pp. 2738–2748, 2007.
- [8] Y. Zhang, L. Li, and H. Liu, "Photocatalytic reduction activity of {001} TiO₂ codoped with F and Fe under visible light for bromate removal," *Journal of Nanomaterials*, vol. 2016, Article ID 5646175, 7 pages, 2016.
- [9] Z. J. Li, W. Z. Shen, W. S. He, and X. T. Zu, "Effect of Fe-doped TiO₂ nanoparticle derived from modified hydrothermal process on the photocatalytic degradation performance on methylene blue," *Journal of Hazardous Materials*, vol. 155, no. 3, pp. 590–594, 2008.
- [10] H. Su, Y. Xie, P. Gao, Y. Xiong, and Y. Qian, "Synthesis of MS/TiO₂ (M = Pb, Zn, Cd) nanocomposites through a mild sol-gel process," *Journal of Materials Chemistry*, vol. 11, pp. 684–686, 2001.
- [11] V. Štengl, S. Bakardjieva, N. Murafa, V. Houšková, and K. Lang, "Visible-light photocatalytic activity of TiO₂/ZnS nanocomposites prepared by homogeneous hydrolysis," *Microporous and Mesoporous Materials*, vol. 110, no. 2-3, pp. 370–378, 2008.
- [12] A. Hamdi, D. P. Ferreira, A. M. Ferraria et al., "TiO₂-CdS nanocomposites: effect of CdS oxidation on the photocatalytic activity," *Journal of Nanomaterials*, vol. 2016, Article ID 6581691, 11 pages, 2016.
- [13] J. Tao, J. Chai, L. Guan, J. Pan, and S. Wang, "Effect of interfacial coupling on photocatalytic performance of large scale MoS₂/TiO₂ hetero-thin films," *Applied Physics Letters*, vol. 106, no. 8, Article ID 081602, 2015.
- [14] I. Tacchini, E. Terrado, A. Ansón, and M. T. Martínez, "Preparation of a TiO₂MoS₂ nanoparticle-based composite by solvothermal method with enhanced photoactivity for the degradation of organic molecules in water under UV light," *Micro & Nano Letters*, vol. 6, no. 11, pp. 932–936, 2011.
- [15] C. Wang, H. Lin, Z. Liu, J. Wu, Z. Xu, and C. Zhang, "Controlled formation of TiO₂/MoS₂ core-shell heterostructures with enhanced visible-light photocatalytic activities," *Particle & Particle Systems Characterization*, vol. 33, no. 4, pp. 221–227, 2016.
- [16] S. Kanda, T. Akita, M. Fujishima, and H. Tada, "Facile synthesis and catalytic activity of MoS₂/TiO₂ by a photodeposition-based technique and its oxidized derivative MoO₃/TiO₂ with a unique photochromism," *Journal of Colloid and Interface Science*, vol. 354, no. 2, pp. 607–610, 2011.
- [17] W. Zhou, Z. Yin, Y. Du et al., "Synthesis of few-layer MoS₂ nanosheet-coated TiO₂ nanobelt heterostructures for enhanced photocatalytic activities," *Small*, vol. 9, no. 1, pp. 140–147, 2013.
- [18] X. Zhou, M. Licklederer, and P. Schmuki, "Thin MoS₂ on TiO₂ nanotube layers: an efficient co-catalyst/harvesting system for photocatalytic H₂ evolution," *Electrochemistry Communications*, vol. 73, pp. 33–37, 2016.
- [19] P. Zhang, T. Tachikawa, M. Fujitsuka, and T. Majima, "Efficient charge separation on 3D architectures of TiO₂ mesocrystals packed with a chemically exfoliated MoS₂ shell in synergetic hydrogen evolution," *Chemical Communications*, vol. 51, no. 33, pp. 7187–7190, 2015.
- [20] W. Zhang, X. Xiao, L. Zheng, and C. Wan, "Fabrication of TiO₂/MoS₂@zeolite photocatalyst and its photocatalytic activity for degradation of methyl orange under visible light," *Applied Surface Science*, vol. 358, part A, pp. 468–478, 2015.
- [21] H. N. T. Phung, N. D. Truong, L. T. Nguyen, K. L. T. Phan, P. A. Duong, and V. T. H. Le, "Enhancement of the visible light photocatalytic activity of vanadium and nitrogen co-doped TiO₂ thin film," *Journal of Nonlinear Optical Physics & Materials*, vol. 24, no. 4, Article ID 1550052, 2015.
- [22] P. K. Nair, V. M. Garcia, A. B. Hernandez, and M. T. S. Nair, "Photoaccelerated chemical deposition of pbs thin films: novel applications in decorative coatings and imaging techniques," *Journal of Physics D: Applied Physics*, vol. 24, no. 8, pp. 1466–1472, 1991.

Research Article

Facile Hydrothermal Synthesis of SnO₂ Nanospheres as Photocatalysts

Wenquan Hu^{1,2} and Xiaoguang Yuan¹

¹School of Materials Science and Engineering, Shenyang University of Technology, Shenyang 110870, China

²School of Materials Science and Engineering, Liaoning Technical University, Fuxin 123000, China

Correspondence should be addressed to Xiaoguang Yuan; yuanxg@sut.edu.cn

Received 15 March 2017; Accepted 6 April 2017; Published 31 May 2017

Academic Editor: Xiaowei He

Copyright © 2017 Wenquan Hu and Xiaoguang Yuan. This is an open access article distributed under the Creative Commons Attribution License, which permits unrestricted use, distribution, and reproduction in any medium, provided the original work is properly cited.

Large amounts of SnO₂ nanospheres are successfully synthesized through a simple and effective hydrothermal method. The as-synthesized products consist of numerous small SnO₂ nanocrystals with an average diameter of 40 nm. The as-prepared SnO₂ nanospheres are further used as the photocatalysts for photodegrading several organic dyes (methylene blue, methyl orange, Congo red, and rhodamine B) under UV light irradiation. The photocatalytic results show that the as-synthesized SnO₂ nanospheres possess high photocatalytic activities. Compared with the degradation rates of other dyes, that of methylene blue reaches 98.5% by 30 min irradiation. It reveals that the as-prepared product might be potential candidate in wastewater purification.

1. Introduction

Nowadays, with quick development of the industry and the improvement of people's life, environmental pollution has become one of the most serious problems [1–3]. Therefore, it is urgent to find effective solutions for these issues. The photocatalytic technique possesses fast and complete decomposition advantage when the pollutants are degraded by the oxidation of photocatalytic process [4, 5]. Among them, semiconductor oxide nanomaterials as the photocatalysts present many advantages compared with traditional oxidants. They can completely degrade the contaminants with sunlight or UV radiation at room temperature and do not cause any secondary pollution [6]. These oxide nanomaterials include TiO₂ [7–9], ZnO [10–12], SnO₂ [13–15], and Fe₂O₃ [16–19].

SnO₂ is an important n-type semiconductor material with excellent chemical and physical performances. As an effective photocatalyst, SnO₂ nanostructures can photodegrade organic pollutants to other nontoxic small molecules by UV irradiation process. The size and morphology of

the nanomaterials have significant effects on their properties [20–22]. So far, researchers have prepared various morphologies of SnO₂ nanostructures, such as nanospheres, nanocubes, nanoflowers, nanowires, and nanodendrites. In this work, we report on the synthesis of large scale SnO₂ nanospheres using a one-pot hydrothermal method and investigate their photocatalytic properties under UV light irradiation.

2. Experimental Details

In a typical synthesis, the experimental procedures are described as follows: Na₂SnO₃ and C₆H₁₂O₆ with a molar ratio of 1:4 (7.5 mmol and 30 mmol) were added to 50 mL deionized water by stirring for 2 h to form a stable and clear solution at room temperature. Then the above mixture was transferred to a 100 mL Teflon lined stainless steel autoclave and heated at 160°C for 3 h. Then it was naturally cooled to room temperature. The brown precipitates were collected by centrifuging at 4000 rpm and then washed for three times with deionized water and ethanol and dried at 80°C.

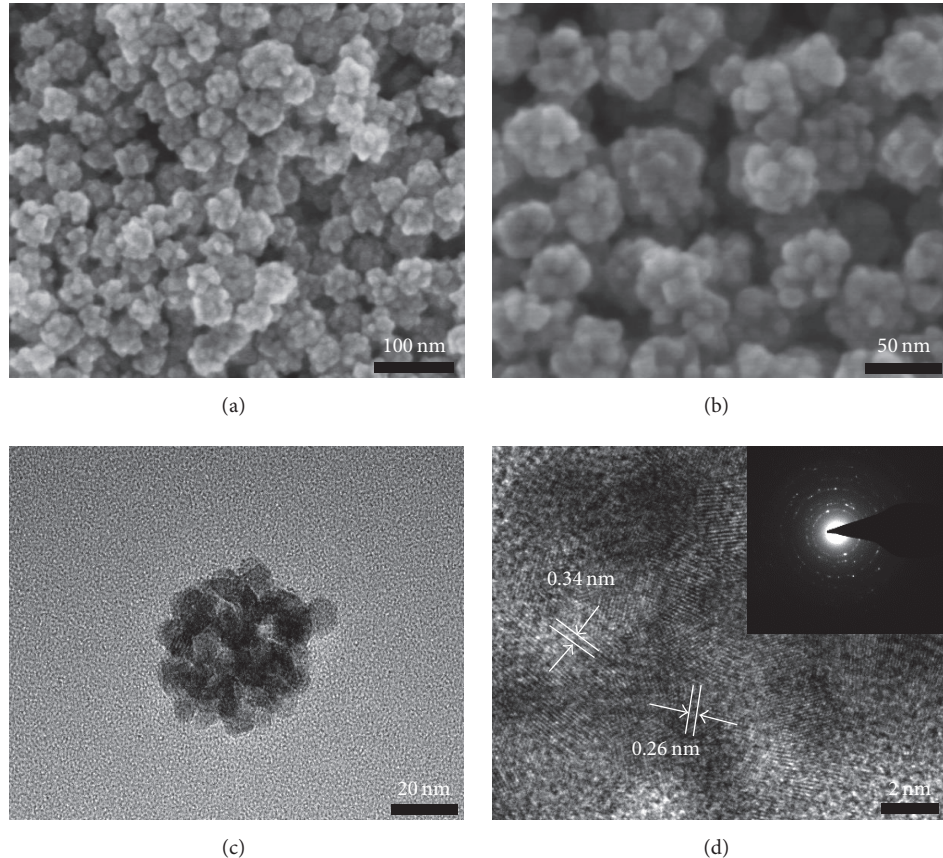


FIGURE 1: SEM and TEM images of SnO_2 nanospheres. (a) Low magnification SEM image of SnO_2 nanospheres. (b) High magnification SEM image of SnO_2 nanospheres. (c) TEM image of single SnO_2 nanosphere. (d) HRTEM image of single SnO_2 nanosphere, the inset is SAED pattern.

Finally, the as-prepared precursors were calcined at 500°C for 5 h.

The morphology and microstructure of the as-prepared product were characterized by using scanning electron microscopy (SEM, Hitachi-4800) and transmission electron microscopy (TEM, JEOL-2010). To examine the crystal structure of the products, the as-prepared sample was investigated by using X-ray diffraction (XRD, Rigaku Dmax-rB, Cuk α radiation, $\lambda = 0.1542 \text{ nm}$, 40 kV, 100 mA). The efficiency of the photocatalytic degradation was analyzed by monitoring dye decolorization at the maximum absorption wavelength using a UV/Vis Spectrometer (Shimadzu UV-2550).

The photocatalytic activities of the as-synthesized products for the degradation of four dyes' aqueous solution were evaluated. 0.1 g of SnO_2 nanospheres was dissolved in 200 mL organic dyes (20 mg L^{-1}). The mixtures were continuously stirred for 1 h in the dark to ensure adsorption/desorption equilibrium. And then the solution was exposed to UV irradiation using a 500 W mercury lamp. For evaluating their photocatalytic activities, the dye samples were collected at regular intervals to measure the dye-degradation using UV-vis spectroscopy. Subsequently, SnO_2 photocatalysts were

separated from the dye solution by centrifugation, washed with ethanol and water, and calcined at 500°C for reuse in the next run.

3. Results and Discussion

Figure 1(a) shows that the as-synthesized sample possesses a sphere-like shape. The average diameter of the nanosphere is 40 nm and their surfaces are very rough and consist of many small particles, as shown in Figure 1(b). TEM characterization was further conducted. Figure 1(c) shows a typical TEM image of a single nanosphere. One can find the nanosphere is formed by the aggregation of several smaller nanoparticles. Figure 1(d) shows the measured lattice fringes from HRTEM image are 0.264 and 0.334 nm, respectively, which are consistent with the (110) and (101) planes of tetragonal rutile SnO_2 phase. The SAED pattern in the inset in Figure 1(d) reveals the as-synthesized nanospheres are polycrystalline.

Crystal structures of the as-prepared SnO_2 product are characterized by XRD, as shown in Figure 2(a). All of the diffraction peaks can be straightforwardly indexed to tetragonal rutile SnO_2 phase which are in accordance with

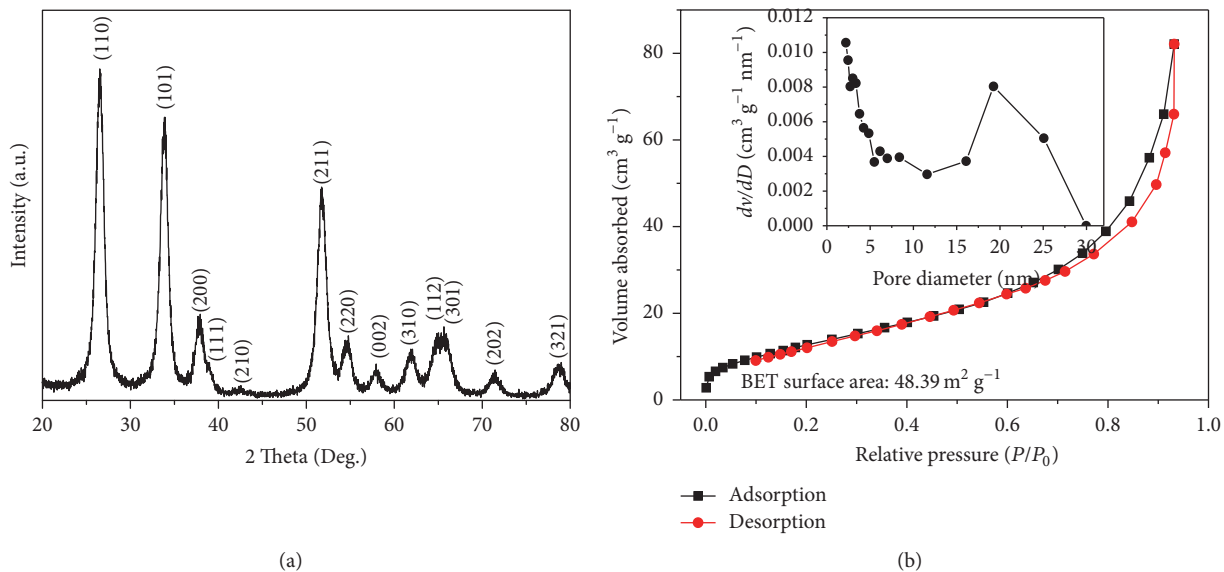


FIGURE 2: XRD pattern and nitrogen adsorption/desorption isotherm of SnO_2 nanospheres. (a) XRD pattern of SnO_2 nanospheres. (b) Nitrogen adsorption/desorption isotherm of SnO_2 nanospheres, the inset is pore diameter distribution.

the standard PDF card (JCPDS: 36-1451). No peaks of other phases were detected in the as-synthesized products, revealing high purity of the as-prepared SnO_2 nanospheres. All the strong and sharp diffraction peaks mean high crystallinity of the as-synthesized products and the broad diffraction peaks might be ascribed to small grain sizes.

In order to further study specific surface area and pore diameter distribution of SnO_2 nanospheres, the sample is characterized by nitrogen adsorption/desorption measurements. Figure 2(b) is the nitrogen adsorption/desorption isotherm, revealing a typical IV isotherm with a typical H_3 type hysteresis loop. Pore diameter distribution curve in the inset of Figure 2(b) shows that the as-synthesized product possesses mesoporous structure and the pore diameter is 5 nm. BET surface area of the product is $48.39 \text{ m}^2 \text{ g}^{-1}$.

To investigate potential applications in wastewater purification of the as-synthesized products, photocatalytic degradation experiments of SnO_2 nanospheres for methylene blue, rhodamine B, methyl orange, and Congo red aqueous solution under a mercury lamp of 500 W irradiation were carried out, respectively. The adsorption spectra of these organic dyes are shown in Figure 3. It is found that main absorption peaks of these dyes are almost completely diminished by irradiation. Figure 3(a) shows the adsorption spectra of methylene blue solution at different time intervals. The color of the solution almost completely disappears when irradiation time reaches 30 min, corresponding to a photocatalytic degradation rate of 98.5%. Figure 3(b) indicates rhodamine B degradation rate of 96.5% with 70 min irradiation under the same photocatalytic

experimental condition. Figure 3(c) represents the adsorption spectra of methyl orange dye with SnO_2 nanospheres. After 40 min irradiation, it was observed that the main absorption peak decreases to 97.6%. The adsorption spectra of Congo red solution is shown in Figure 3(d). The intensity of the characteristic adsorption peak of Congo red diminishes gradually with the extension of the exposure time. After 35 min of irradiation, the decomposing rate reaches 98.4%. The photocatalytic results indicate that the as-synthesized SnO_2 nanospheres exhibit excellent photocatalytic activity toward these organic dyes under UV light irradiation, and each dye solution is almost fully decomposed. In order to illustrate which dye is highly selective to SnO_2 nanospheres, the tests are done to compare the degradation efficiency of different dyes with the same degradation time. Figure 4(a) shows that SnO_2 nanospheres possess highest degradation rate to methylene blue at 30 min irradiation. To investigate the stability and reusability of the photocatalyst, the recycle experiment for methylene blue was performed. Figure 4(b) shows that there is no significant change even after five cycles. The concentration changes of these dyes are calculated as follows:

$$I = \frac{C}{C_0} \times 100\%. \quad (1)$$

C_0 represents the initial concentration of these organic dyes. C is the real time concentration under UV light. C/C_0 can be used to evaluate the photocatalytic efficiency derived from the concentration changes of these dyes.

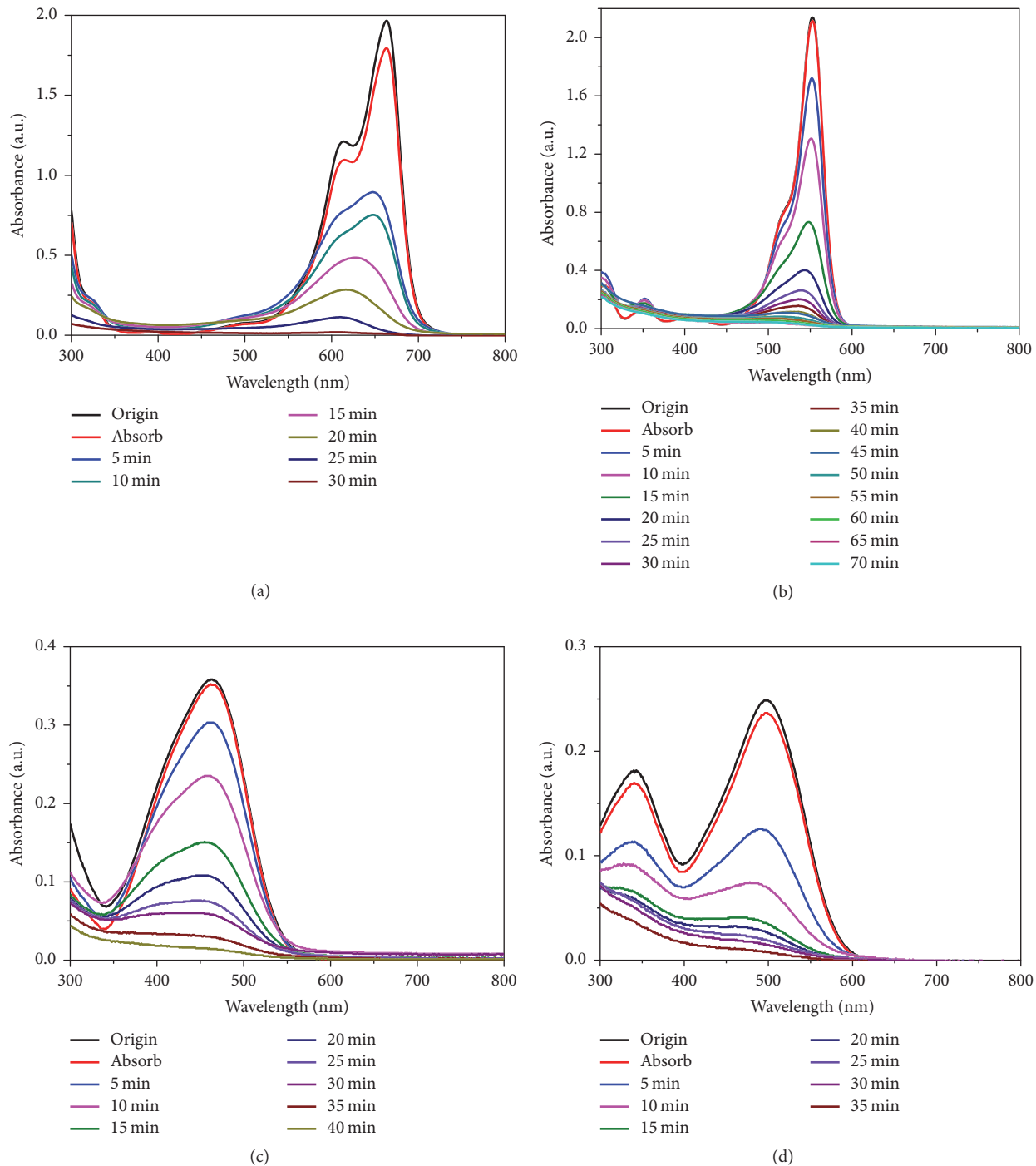


FIGURE 3: Variations in absorption spectra of five organic dye solutions with SnO_2 nanospheres for different time intervals; (a) methylene blue; (b) rhodamine B; (c) methyl orange; (d) Congo red.

4. Conclusion

In summary, large scale SnO_2 nanospheres are successfully synthesized via a simple hydrothermal method. The as-synthesized product consists of numerous small SnO_2

nanocrystals with an average diameter of 40 nm. Photocatalytic experiments show that SnO_2 nanospheres can degrade several organic dyes quickly, revealing excellent photocatalytic performance. The as-prepared photocatalysts might have a potential application in water purification.

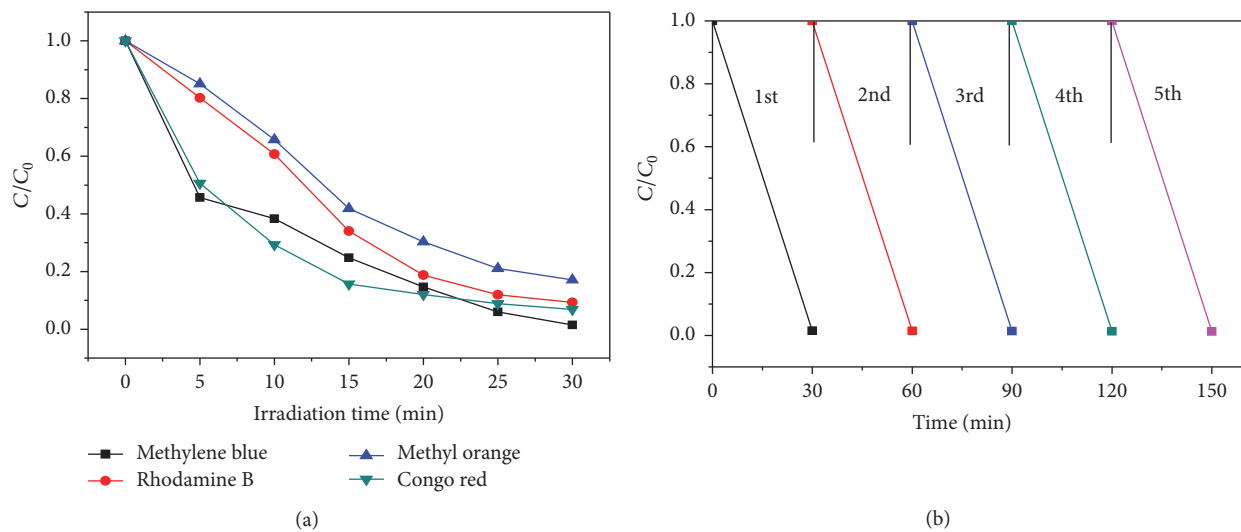


FIGURE 4: Degradation of SnO₂ nanospheres photocatalyst for dye. (a) Degradation rate curve for different dye molecules. (b) Recycling test of SnO₂ nanospheres photocatalyst for MB dye.

Conflicts of Interest

The authors declare that they have no conflicts of interest.

Acknowledgments

This work was supported by Starting Fund from Shenyang University of Technology.

References

- [1] P. Baroni, R. S. Vieira, E. Meneghetti, M. G. C. da Silva, and M. M. Beppu, "Evaluation of batch adsorption of chromium ions on natural and crosslinked chitosan membranes," *Journal of Hazardous Materials*, vol. 152, no. 3, pp. 1155–1163, 2008.
- [2] Y. Han, X. Wu, Y. Ma, L. Gong, F. Qu, and H. Fan, "Porous SnO₂ nanowire bundles for photocatalyst and Li ion battery applications," *CrystEngComm*, vol. 13, no. 10, pp. 3506–3510, 2011.
- [3] Y. Liu, Y. Jiao, Z. Zhang, F. Qu, A. Umar, and X. Wu, "Hierarchical SnO₂ nanostructures made of intermingled ultrathin nanosheets for environmental remediation, smart gas sensor, and supercapacitor applications," *ACS Applied Materials and Interfaces*, vol. 6, no. 3, pp. 2174–2184, 2014.
- [4] S. Han, L. Hu, N. Gao, A. A. Al-Ghamdi, and X. Fang, "Efficient self-assembly synthesis of uniform CdS spherical nanoparticles-Au nanoparticles hybrids with enhanced photoactivity," *Advanced Functional Materials*, vol. 24, no. 24, pp. 3725–3733, 2014.
- [5] W. Jia, X. Wu, B. Jia, F. Qu, and H. J. Fan, "Self-assembled porous ZnS nanospheres with high photocatalytic performance," *Science of Advanced Materials*, vol. 5, no. 10, pp. 1329–1336, 2013.
- [6] Y. H. Jin, K. M. Min, S. D. Seo, H. W. Shim, and D. W. Kim, "Enhanced Li storage capacity in 3 nm diameter SnO₂ nanocrystals firmly anchored on multiwalled carbon nanotubes," *Journal of Physical Chemistry C*, vol. 115, no. 44, pp. 22062–22067, 2011.
- [7] W.-S. Wang, L. Zhen, C.-Y. Xu, and W.-Z. Shao, "Room temperature synthesis, growth mechanism, photocatalytic and photoluminescence properties of cadmium molybdate core-shell microspheres," *Crystal Growth and Design*, vol. 9, no. 3, pp. 1558–1568, 2009.
- [8] M. M. Mahlambi, C. J. Ngila, and B. B. Mamba, "Recent developments in environmental photocatalytic degradation of organic pollutants: the case of Titanium Dioxide nanoparticles-a review," *Journal of Nanomaterials*, vol. 2015, Article ID 790173, 2015.
- [9] Y. Zhang, J. Wan, and Y. Ke, "A novel approach of preparing TiO₂ films at low temperature and its application in photocatalytic degradation of methyl orange," *Journal of Hazardous Materials*, vol. 177, no. 1-3, pp. 750–754, 2010.
- [10] F. Yan, S. Zhang, Y. Liu et al., "High efficient ZnO nanowalnuts photocatalyst: a case study," *Materials Research Bulletin*, vol. 59, pp. 98–103, 2014.
- [11] S. Zhang, B. Yin, Y. Jiao, Y. Liu, F. Qu, and X. Wu, "Nanosheet-assembled ZnO microflower photocatalysts," *Journal of Nanomaterials*, vol. 2014, Article ID 532317, 2014.
- [12] J. Wang, F. Qu, and X. Wu, "Synthesis of ultra-thin ZnO nanosheets: photocatalytic and superhydrophilic properties," *Science of Advanced Materials*, vol. 5, no. 8, pp. 1052–1059, 2013.
- [13] B. Jia, W. Jia, Y. Ma, X. Wu, and F. Qu, "SnO₂ core-shell microspheres with excellent photocatalytic properties," *Science of Advanced Materials*, vol. 4, no. 7, pp. 702–707, 2012.
- [14] L. Wang, L. Shen, L. Zhu, H. Jin, and N. Bing, "Preparation and photocatalytic properties of SnO₂ coated on nitrogen-doped carbon nanotubes," *Journal of Nanomaterials*, vol. 2012, Article ID 794625, 6 pages, 2012.
- [15] B. Jia, W. Jia, F. Qu, and X. Wu, "General strategy for self assembly of mesoporous SnO₂ nanospheres and their applications in water purification," *RSC Advances*, vol. 3, no. 30, pp. 12140–12148, 2013.
- [16] Y. Jiao, Y. Liu, F. Qu, and X. Wu, "Dendritic α -Fe₂O₃ hierarchical architectures for visible light driven photocatalysts," *CrystEngComm*, vol. 16, no. 4, pp. 575–580, 2014.
- [17] S.-W. Cao and Y.-J. Zhu, "Hierarchically nanostructured α -Fe₂O₃ hollow spheres: preparation, growth mechanism, photocatalytic property, and application in water treatment," *Journal of Physical Chemistry C*, vol. 112, no. 16, pp. 6253–6257, 2008.

- [18] K.-J. Noh, H.-J. Oh, B.-R. Kim, S.-C. Jung, W. Kang, and S.-J. Kim, "Photoelectrochemical properties of Fe_2O_3 supported on TiO_2 -based thin films converted from self-assembled hydrogen titanate nanotube powders," *Journal of Nanomaterials*, vol. 2012, Article ID 475430, 2012.
- [19] X. Zheng, Y. Jiao, F. Chai, F. Qu, A. Umar, and X. Wu, "Template-free growth of well-crystalline $\alpha\text{-Fe}_2\text{O}_3$ nanopeanuts with enhanced visible-light driven photocatalytic properties," *Journal of Colloid and Interface Science*, vol. 457, pp. 345–352, 2015.
- [20] X. Wu, W. Cai, and F.-Y. Qu, "Spontaneous formation of single crystal ZnO nanohelices," *Chinese Physics B*, vol. 18, no. 4, pp. 1669–1673, 2009.
- [21] L. Yu, F. Qu, and X. Wu, "Solution synthesis and optimization of ZnO nanowindmills," *Applied Surface Science*, vol. 257, no. 17, pp. 7432–7435, 2011.
- [22] Y. Lei, F. Qu, and X. Wu, "Assembling ZnO nanorods into microflowers through a facile solution strategy: morphology control and cathodoluminescence properties," *Nano-Micro Letters*, vol. 4, no. 1, pp. 45–51, 2012.

Research Article

Spawns Structure of Rod-Like ZnO Wrapped in Cellulose Nanofibers for Electromagnetic Wave Absorption

Bitao Fan,¹ Qiufang Yao,¹ Chao Wang,¹ Ye Xiong,¹ Qingfeng Sun,^{1,2} and Chunde Jin^{1,2}

¹School of Engineering, Zhejiang A&F University, Hangzhou, China

²Key Laboratory of Wood Science and Technology, Hangzhou, China

Correspondence should be addressed to Qingfeng Sun; qfsun@zafu.edu.cn

Received 20 December 2016; Revised 26 February 2017; Accepted 21 March 2017; Published 27 April 2017

Academic Editor: Weilu Gao

Copyright © 2017 Bitao Fan et al. This is an open access article distributed under the Creative Commons Attribution License, which permits unrestricted use, distribution, and reproduction in any medium, provided the original work is properly cited.

Spawns structure of rod-like ZnO wrapped in the cellulose nanofibers was successfully fabricated through a facile one-step hydrothermal method, and their electromagnetic wave absorption properties were investigated. The structure and properties of the composite aerogel were characterized. The enlarged morphology images showed that the as-prepared cellulose nanofiber/ZnO samples were spawns structure of rod-like ZnO wrapped in the cellulose nanofibers. The composite aerogel in a wax matrix exhibited excellent electromagnetic wave absorption performance over 2–18 GHz. The widest absorption bandwidth of 30 wt% contained with reflection loss values less than -10 dB was up to 12 GHz (6–18 GHz) at the thickness of 5.5 mm and the minimum reflection loss value reached -26.32 dB at 15.2 GHz when the thickness of the absorber was 3 mm.

1. Introduction

The nanosized metal oxides are becoming very potential materials due to their physicochemical properties and various applications in different fields [1, 2]. Among oxide metals, zinc oxide (ZnO) nanoparticle has attracted more attention because the zinc oxide nanoparticle is a promising material for applications in sensors, magnetics, electronics, and photocatalysis. In the past decade, ZnO-based materials had been focused on for a candidate for electromagnetic (EM) wave absorption due to their excellent dielectric properties [3, 4], semiconductive properties [5], selectable mechanical properties [6] for a typical structural absorber, and large-scale synthesis [7, 8].

The research of inorganic nanoparticles/polymer composite was a very interesting materials, which could combine the properties of organic and inorganic materials [9, 10]. On the other hand, the inorganic nanoparticles/polymer composite could improve the stability, retain the special morphology, and control the synthesis of nanoparticles [11]. Nanometer-sized single cellulose, the natural polymer, had been extensively used in kinds of fields due to its nanoscale dimensions [12], high surface area [13], unique morphology [14], low density [15], and high mechanical strength [16] with

the entanglement of high-aspect-ratio [17] cellulose nanofibers (CNF).

In this study, the spawns structure of rod-like ZnO wrapped in CNF was successfully fabricated for EM wave absorption. In the system of the CNF/ZnO (CNFZ) composite, cellulose nanofibers were used as a scaffold. Combining cellulose and ZnO rods into the spawns structure could be considered as an effective and competitive route to obtain lightweight composites with outstanding EM wave absorbing performance.

2. Material and Methods

2.1. Materials. Zinc nitrate hexahydrate ($Zn(NO_3)_2 \cdot 6H_2O$), hexamethylene tetramine ($C_6H_{14}N_4$), and other chemicals were of analytical grade and were produced by Aladdin Industrial Co. The bamboo was obtained from the bamboo forest in Zhejiang, China. All the chemicals were used as received. Deionized water was used in all experiments.

2.2. Preparation of CNF. The purified cellulose after ultrasonic treatment was obtained; refer to Xie et al. [18]. Then the CNF colloid solution was obtained from the suspension

after centrifugation at 6000 rpm for 5 minutes. CNF colloid solution was separated into molds and placed in a refrigerator for about 12 h. The frozen samples were freeze-dried for 60 h using a Scientz-18N freeze-dryer to sublime the materials. The cold trap temperature was less than -55°C , and the vacuum pressure was less than $10\ \mu\text{Pa}$ during the freeze-drying process. The sponge-like CNF was successfully prepared.

2.3. Preparation of the CNFZ Composite Aerogel. The spawns structure of rod-like ZnO wrapped in CNF was prepared by one-step hydrothermal approach [19]. 100 mg CNF, 3 mmol $\text{Zn}(\text{NO}_3)_2 \cdot 6\text{H}_2\text{O}$, and 3 mmol $\text{C}_6\text{H}_{14}\text{N}_4$ were put into deionized water (100 mL) with magnetic stirring for 10 min at room temperature. Subsequently, the mixtures were transferred to a Teflon-lined stainless-steel autoclave. The autoclave was placed in an oven and heated at 100°C for 120 min. After the suspension was cooled down naturally, the obtained homogeneous suspension was freeze-dried at -55°C at $10\ \mu\text{Pa}$ for 60 h. The lightweight, solid, and sponge-like CNFZ aerogel was successfully fabricated.

2.4. Characterization. The morphological feature of the CNF and CNFZ was observed using scanning electron microscope (SEM, FEI, Quanta 200, USA) and transmission electron microscope (TEM, FEI, Tecnai G20, USA). Crystalline structures were identified by X-ray diffraction technique (XRD, Rigaku, D/MAX 2200, Japan) operating with $\text{Cu K}\alpha$ radiation ($\lambda = 1.5418\ \text{\AA}$) at a scan rate (2θ) of $4^{\circ}\ \text{min}^{-1}$ and the accelerating voltage of 40 kV and the applied current of 30 mA ranging from 5° to 75° . The X-ray photoelectron spectroscopy (XPS, ULVAC-PHI, Inc., Japan) analysis of the specimen was carried out using a microfocused (100 lm, 25 W, 15 kV) monochromatic Al-K α source ($hm = 1486.6\ \text{eV}$), a hemispherical analyzer, and a multichannel detector. The composite samples used for EM wave absorption measurement were prepared by mixing the aerogel with paraffin wax 30 wt% of the aerogel. The EM wave absorption of the mixtures at 2–18 GHz frequency range was measured by using an Agilent E8363B vector network analyzer.

3. Results and Discussion

Figure 1 showed the morphological features of CNF and CNFZ. As shown in Figure 1(a), it could be observed that the slender fibers were cross-linked with a length of $150\ \mu\text{m}$. Figure 1(b) showed TEM image of CNF, which exhibited some slender fibrils with average diameter of $56.3\ \text{nm}$. It could be concluded that the CNF had a large length-diameter ratio of about 2664. Figure 1(c) showed the SEM image of CNFZ. After the hydrothermal reaction, spawns structure of ZnO rods wrapped in the CNF was formed. Figure 1(d) showed the enlarged image of the spawns structure. Figure 1(e) showed the selected-area electron diffraction (SAED) pattern of CNFZ which indicated that a single rod was a single crystal. HRTEM image was shown in Figure 1(f). It was clearly revealed that lattice fringe with a spacing value of $0.28\ \text{nm}$ depicts the lattice-resolved (100) crystalline plane of hexagonal ZnO.

Figure 2 showed the XRD patterns of the CNF and CNFZ. As shown in Figure 2(a), it was clear that the diffraction peaks in XRD pattern at $2\theta = 16.5^{\circ}$ and 22.5° were typical cellulose structure. In the case of CNFZ, the peaks of cellulose still exist in Figure 2(b), revealing that the crystal structure of cellulose did not change after the hydrothermal treatment. Furthermore, the additional diffraction peaks of CNFZ were observed at 31.75° , 34.5° , 36.3° , 47.5° , 56.6° , 62.9° , 66.4° , 68.0° , and 69.1° corresponding to the planes of (100), (002), (101), (102), (110), (103), (200), (112), and (201), which could be indexed to the hexagonal ZnO (wurtzite, JCPDS Number 36-1451).

Figure 3 showed the XPS spectra of the CNF and CNFZ. As shown in Figure 3(a), the wide scan spectra of the CNF exhibited two major peaks with binding energy at $286.1\ \text{eV}$ and $532.1\ \text{eV}$ corresponding to the C 1s and O 1s of CNF, respectively. However, in the CNFZ, it exhibited four major peaks with binding energy at $286.1\ \text{eV}$, $532.1\ \text{eV}$, $1021.4\ \text{eV}$, and $1044.4\ \text{eV}$ corresponding to the C 1s ($286.1\ \text{eV}$), O 1s ($532.1\ \text{eV}$), and Zn 2p ($1021.4\ \text{eV}$ and $1044.4\ \text{eV}$) of CNFZ, respectively, which could indicate that the Zn element was added in the sample of CNFZ. The high-resolution XPS spectra of key elements (C 1s and O 1s) and extra element (Zn 2p) were carried out and were shown in Figures 3(b)–3(f). As shown in Figure 3(b), the binding energies of Zn appeared at $1021.37\ \text{eV}$ and $1044.47\ \text{eV}$ (Figure 3(b)), respectively, which could be well attributed to the Zn element. It could be concluded that ZnO has been produced in CNFZ successfully. Figure 3(c) showed three peaks observed at $284.9\ \text{eV}$, $286.3\ \text{eV}$, and $287.9\ \text{eV}$ in the high-resolution spectra of C 1s in CNF, which clearly indicated the presence of C-C, C-O, and O-C-O. Upon hydrothermal reaction, the high-resolution C 1s spectrum of CNFZ (Figure 3(d)) showed similar results to those of CNF. The same peaks were located in the same places. The differences in the same peak on intensity at $284.9\ \text{eV}$ were attributed to C-C; the results might be attributed to some degradation during hydrothermal treatment. Two peaks which attributed to O-H and O-C-O and C-O-C were observed at $532.8\ \text{eV}$ in the high-resolution spectra of O 1s in CNF (Figure 3(e)). Another peak was observed at $530.12\ \text{eV}$ in the high-resolution spectra of O 1s in CNFZ except the two peaks in the high-resolution spectra of O 1s in CNF at the same location (Figure 3(f)). The additional peak could be attributed to the original lattice oxygen species in ZnO [20]. According to the above results, it could be deduced that ZnO would have been produced in CNFZ successfully.

Figure 4 showed the formation mechanism of the spawns structure of rod-like ZnO wrapped in CNF. A possible mechanism could be inferred from the basic physics of electrostatic interaction between positively charged ZnO and negatively charged CNF. Firstly, spawns structure of ZnO wrapped in CNF was prepared by a hydrothermal method. When $\text{C}_6\text{H}_{14}\text{N}_4$ and $\text{Zn}(\text{NO}_3)_2$ were added in cellulose nanofibers solution at 100°C for 120 min, ZnO crystal seed was proceeding and homogeneously distributed in the solution. With the ZnO rods growing, spawns structure of rod-like ZnO wrapped in CNF was created by an electrostatic interaction between positively charged ZnO and negatively charged CNF. Therefore, CNF could be close to ZnO rods and

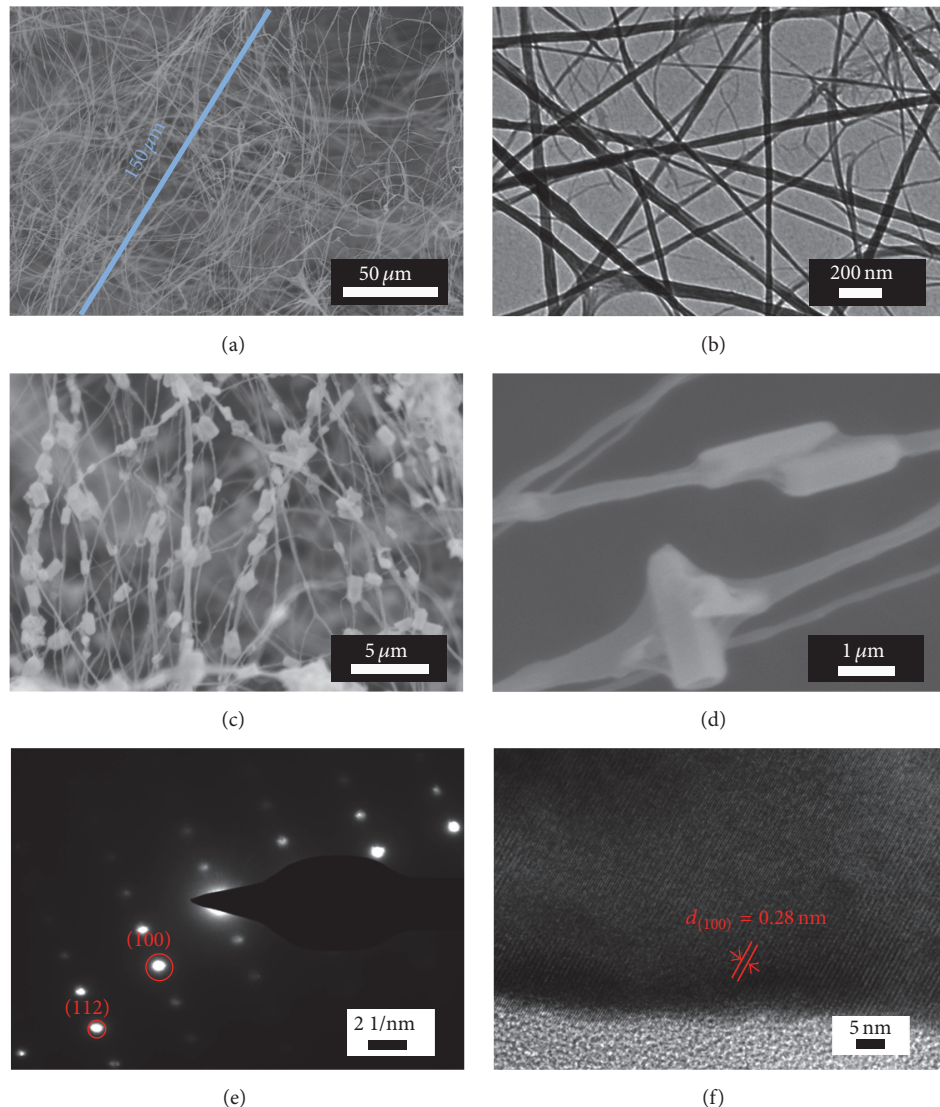


FIGURE 1: The morphology of CNF and CNFZ. (a) The SEM and (b) TEM image of CNF, (c) the SEM, (d) the enlarged image, (e) HRTEM, and (f) SADE of CNFZ.

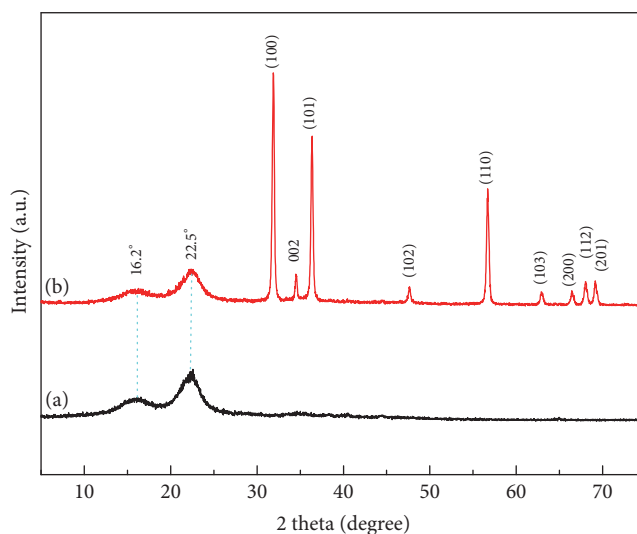


FIGURE 2: XRD patterns of (a) CNF and (b) CNFZ.

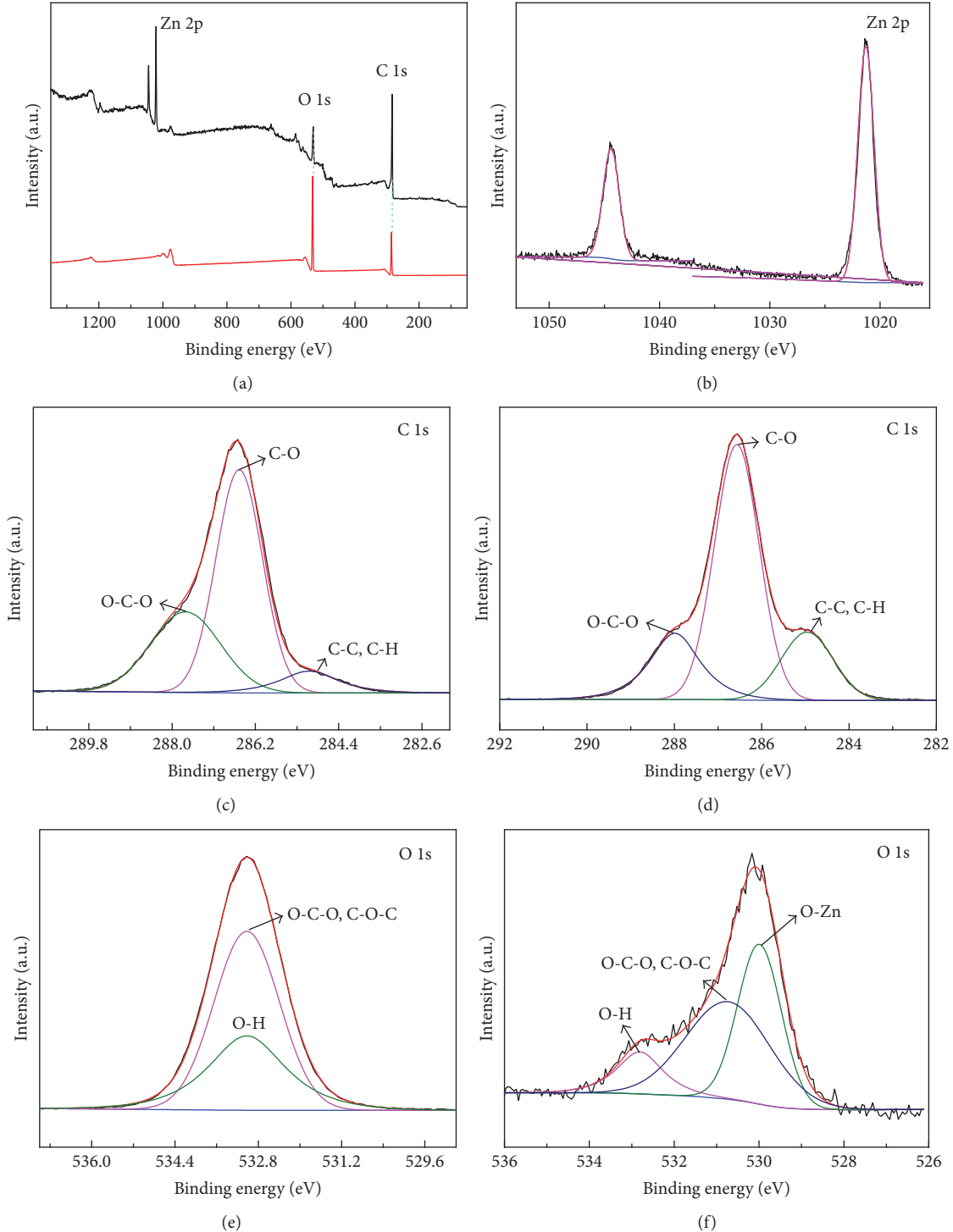


FIGURE 3: (a) A full scan XPS spectra of CNF and CNFT, (b) high-resolution XPS spectra of Zn element on CNFZ composite aerogel, (c and d) high-resolution XPS spectra of C 1s of CNF and CNFZ, and (e and f) high-resolution XPS spectra of O 1s of CNF and CNFZ.

wrapped ZnO rods like a net acted as a shell. Subsequently, freeze-drying was carried out to sublimate the liquid into gas phase. The lightweight aerogel with the structure of ZnO spawns wrapped in cellulose nanofibers was fabricated.

Figure 5 showed the reflection loss (RL) values versus frequency of the CNFZ at different thickness (1–5.5 mm)

with a filler loading of 30 wt%. It could be observed that the CNFZ exhibited a certain degree of abilities for EM wave absorption. The different thickness of the CNFZ had a great influence on the frequency of electromagnetism wave absorption properties. When the thickness increased, the frequency of RL peak had a tendency to shift from

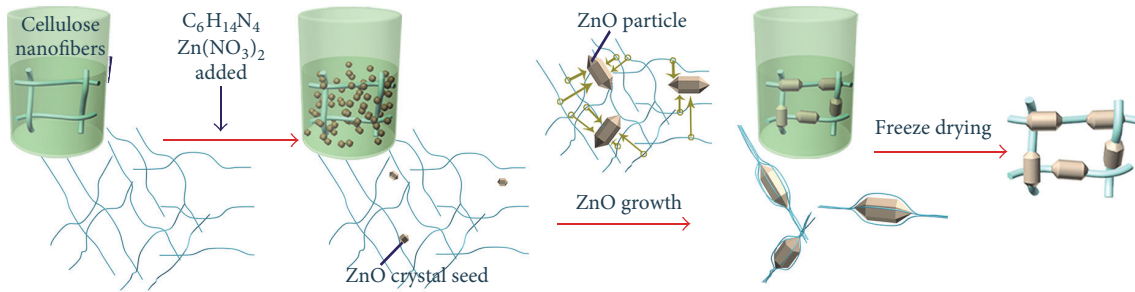


FIGURE 4: Schematic illustration of the formation process of spawns of rod-like ZnO wrapped in cellulose nanofibers.

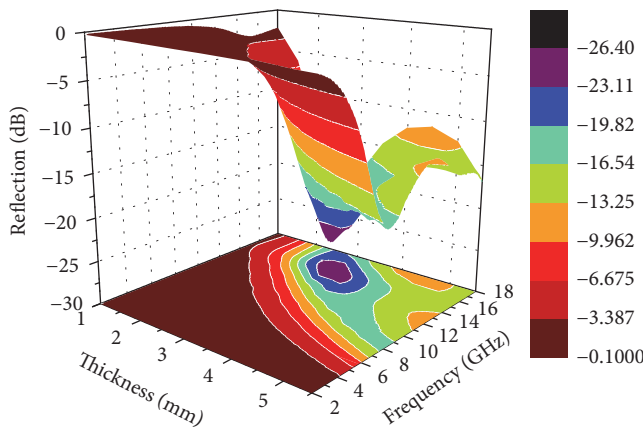


FIGURE 5: Reflection loss for the samples absorbers with loading of 30 wt% at different thickness.

high frequency to low frequency. The RL_{min} value reached -26.32 dB at 15.2 GHz when the thickness of the absorber was 3 mm. Importantly, the widest absorption bandwidth corresponding to RL value less than -10 dB was almost up to 12 GHz (6.0–18.0 GHz) at the thickness of 5.5 mm. In order to increase the properties of absorption for EM, many researches had been conducted in the previous investigation. The summary of results for EM absorption employed by different structure of ZnO was shown in Table 1. The RL behaviors of CNFZ usually depend on their loss mechanisms, which are determined by their nature and structure. The above results indicated that the spawns structure of rod-like ZnO wrapped in CNF had strong absorption for EM. This was mainly because of the interfacial electric polarization. It can be noticed that the spawns structure of rod-like ZnO wrapped in CNF had unique multiple interfaces between the rod-like ZnO, CNF, paraffin matrix, and air bubbles. It is available for the EM to penetrate the porous layer formed by the multiple poles at the interfaces and the energy will be induced into dissipative current, which leads to the energy attenuation.

4. Conclusions

Spawns structure of rod-like ZnO wrapped in CNF was successfully fabricated through a facile hydrothermal process. CNF could be close to ZnO rods and wrapped ZnO rods like spawns structure due to the basic physics of electrostatic

TABLE 1: Summary of results for EM absorption employed by different structure of ZnO.

Materials	Structure	RL_{min} (dB)	Width (GHz) ($RL_{min} \leq 10$)	Ref
ZnO	CNFZ	-26.32	12	This work
ZnO	Urchin-like ZnO hollow spheres	-20	1.2	[20]
ZnO	Zn(Fe)/ZnO nanocapsules	-18	8	[21]
ZnO	Uniform ZnO nanorods	-25.44	3.8	[22]
ZnO	Porous Fe ₃ O ₄ @ZnO sphere	-37.5	11.4	[23]

interaction between positively charged ZnO and negatively charged CNF. The composite aerogel in a wax matrix exhibits excellent EM wave absorption performance. The widest absorption bandwidth with RL values less than -10 dB was up to 12 GHz (6.0–18.0 GHz) and the minimum RL value reached -26.32 dB at 15.2 GHz.

Conflicts of Interest

The authors declare that there are no conflicts of interest regarding the publication of this manuscript.

Acknowledgments

This work was supported by Zhejiang Provincial Natural Science Foundation of China (no. LZ14C160001), Scientific Research Foundation of Zhejiang A&F University (Grant no. 2014FR077), Public Projects of Zhejiang Province (no. 2015C32014), and the Fund for Innovative Research Team of Forestry Engineering Discipline (101-206001000713).

References

- [1] S. Alexander, V. Gomez, and A. R. Barron, "Carboxylation and decarboxylation of aluminum oxide nanoparticles using bifunctional carboxylic acids and octylamine," *Journal of Nanomaterials*, vol. 2016, Article ID 7950876, 2016.
- [2] D.-Y. Kang, P. Pokharel, Y.-S. Kim, S. Choi, and S.-H. Choi, "Synthesis of metal oxide decorated polycarboxyphenyl polymer-grafted multiwalled carbon nanotube composites by

- a chemical grafting approach for supercapacitor application," *Journal of Nanomaterials*, vol. 2015, Article ID 535319, pp. 1–11, 2015.
- [3] A. S. Lanje, S. J. Sharma, R. S. Ningthoujam, J.-S. Ahn, and R. B. Pode, "Low temperature dielectric studies of zinc oxide (ZnO) nanoparticles prepared by precipitation method," *Advanced Powder Technology*, vol. 24, no. 1, pp. 331–335, 2013.
 - [4] Y.-H. Lin and J.-C. Chou, "Interface study on amorphous indium gallium zinc oxide thin film transistors using high-k gate dielectric materials," *Journal of Nanomaterials*, vol. 2015, Article ID 782786, pp. 1–6, 2015.
 - [5] J. Xu, Z. Chen, J. A. Zapien, C.-S. Lee, and W. Zhang, "Surface engineering of ZnO nanostructures for semiconductor-sensitized solar cells," *Advanced Materials*, vol. 26, no. 31, pp. 5337–5367, 2014.
 - [6] J. Liu, W. Cao, H. Jin, J. Yuan, D. Zhang, and M. Cao, "Enhanced permittivity and multi-region microwave absorption of nanoneedle-like ZnO in the X-band at elevated temperature," *Journal of Materials Chemistry C*, vol. 3, no. 18, pp. 4670–4677, 2015.
 - [7] S. S. Arbuj, N. Rumale, A. Pokle et al., "Synthesis of photoluminescent ZnO nanopencils and their photocatalytic performance," *Science of Advanced Materials*, vol. 6, no. 2, pp. 269–275, 2014.
 - [8] F. Davar, A. Majedi, and A. Mirzaei, "Green synthesis of ZnO nanoparticles and its application in the degradation of some dyes," *Journal of the American Ceramic Society*, vol. 98, no. 6, pp. 1739–1746, 2015.
 - [9] J. Zeng, S. Liu, J. Cai, and L. Zhang, "TiO₂ immobilized in cellulose matrix for photocatalytic degradation of phenol under weak UV light irradiation," *Journal of Physical Chemistry C*, vol. 114, no. 17, pp. 7806–7811, 2010.
 - [10] T. Thorvaldsen, B. B. Johnsen, T. Olsen, and F. K. Hansen, "Investigation of theoretical models for the elastic stiffness of nanoparticle-modified polymer composites," *Journal of Nanomaterials*, vol. 2015, Article ID 281308, pp. 1–17, 2015.
 - [11] M. Fujita, N. Idota, K. Matsukawa, and Y. Sugahara, "Preparation of oleyl phosphate-modified TiO₂/poly(methyl methacrylate) hybrid thin films for investigation of their optical properties," *Journal of Nanomaterials*, vol. 2015, Article ID 297197, 2015.
 - [12] L. Berglund, M. Noël, Y. Aitomäki, T. Öman, and K. Oksman, "Production potential of cellulose nanofibers from industrial residues: efficiency and nanofiber characteristics," *Industrial Crops and Products*, vol. 92, pp. 84–92, 2016.
 - [13] C. Moser, G. Henriksson, and M. E. Lindström, "Specific surface area increase during cellulose nanofiber manufacturing related to energy input," *BioResources*, vol. 11, no. 3, pp. 7124–7132, 2016.
 - [14] H. Almasi, B. Ghanbarzadeh, J. Dehghannya, A. A. Entezami, and A. K. Asl, "Novel nanocomposites based on fatty acid modified cellulose nanofibers/poly(lactic acid): morphological and physical properties," *Food Packaging and Shelf Life*, vol. 5, pp. 21–31, 2015.
 - [15] Y. Jiao, C. Wan, T. Qiang, and J. Li, "Synthesis of superhydrophobic ultralight aerogels from nanofibrillated cellulose isolated from natural reed for high-performance adsorbents," *Applied Physics A: Materials Science and Processing*, vol. 122, pp. 1–10, 2016.
 - [16] W. Chen, Q. Li, J. Cao et al., "Revealing the structures of cellulose nanofiber bundles obtained by mechanical nanofibrillation via TEM observation," *Carbohydrate Polymers*, vol. 117, pp. 950–956, 2015.
 - [17] N. Amiralian, P. K. Annamalai, P. Memmott, E. Taran, S. Schmidt, and D. J. Martin, "Easily deconstructed, high aspect ratio cellulose nanofibres from Triodia pungens; an abundant grass of Australia's arid zone," *RSC Advances*, vol. 5, no. 41, pp. 32124–32132, 2015.
 - [18] J. Xie, C.-Y. Hse, C. F. De Hoop, T. Hu, J. Qi, and T. F. Shupe, "Isolation and characterization of cellulose nanofibers from bamboo using microwave liquefaction combined with chemical treatment and ultrasonication," *Carbohydrate Polymers*, vol. 151, pp. 725–734, 2016.
 - [19] K. V. Gurav, M. G. Gang, S. W. Shin et al., "Gas sensing properties of hydrothermally grown ZnO nanorods with different aspect ratios," *Sensors and Actuators B: Chemical*, vol. 190, no. 1, pp. 439–445, 2014.
 - [20] G. Wu, Y. Cheng, Q. Xie, Z. Jia, F. Xiang, and H. Wu, "Facile synthesis of urchin-like ZnO hollow spheres with enhanced electromagnetic wave absorption properties," *Materials Letters*, vol. 144, no. 1, pp. 157–160, 2015.
 - [21] Z. H. Wang, L. W. Jiang, D. Li et al., "Permittivity and permeability of Zn(Fe)/ZnO nanocapsules and their microwave absorption in the 2–18GHz range," *Journal of Applied Physics*, vol. 115, no. 17, 401 pages, 2014.
 - [22] G.-S. Wang, Y.-Y. Wu, X.-J. Zhang, Y. Li, L. Guo, and M.-S. Cao, "Controllable synthesis of uniform ZnO nanorods and their enhanced dielectric and absorption properties," *Journal of Materials Chemistry A*, vol. 2, no. 23, pp. 8644–8651, 2014.
 - [23] D. Sun, Q. Zou, Y. Wang, Y. Wang, W. Jiang, and F. Li, "Controllable synthesis of porous Fe₃O₄@ZnO sphere decorated graphene for extraordinary electromagnetic wave absorption," *Nanoscale*, vol. 6, no. 12, pp. 6557–6562, 2014.

Research Article

Influence of Heat Treatment on the Morphologies of Copper Nanoparticles Based Films by a Spin Coating Method

Wei Liu,^{1,2} Jiayu Guo,¹ Zhonghua Fan,³ Xiaorong Wang,³ Dingkun Yu,³ Rong Chen,³ Shisheng Huang,³ and Peng He²

¹College of Materials Science and Engineering, China Jiliang University, Hangzhou 310018, China

²State Key Laboratory of Advanced Welding and Joining, Harbin Institute of Technology, Harbin 150001, China

³Hangzhou Huaguang Advanced Welding Materials Co., Ltd., Hangzhou 311112, China

Correspondence should be addressed to Peng He; hepeng@hit.edu.cn

Received 12 December 2016; Accepted 6 March 2017; Published 20 March 2017

Academic Editor: Xiaowei He

Copyright © 2017 Wei Liu et al. This is an open access article distributed under the Creative Commons Attribution License, which permits unrestricted use, distribution, and reproduction in any medium, provided the original work is properly cited.

We have investigated the influence of heat treatment on the morphologies of copper nanoparticles based films on glass slides by a spin coating method. The experiments show that heat treatment can modify the sizes and morphologies of copper nanoparticles based films on glass slides. We suggest that through changing the parameters of heat treatment process may be helpful to vary the scattering and absorbing intensity of copper nanoparticles when used in energy harvesting/conversion and optical devices.

1. Introduction

Synthesis of metal nanoparticles with novel size-dependent physical and chemical and optical properties (e.g., quantum-confinement effects) plays a crucial role in many fields, such as optical label, catalysis, printed circuits, nanobrazing, and sensors during the past decade [1–5]. Among these various metal nanoparticles, noble metal nanoparticles such as Au, Ag, and Pt are getting special attention as they can be used in labels of immunoassays, lithographic fabrication, electronics, solar cell, nanobrazing, and surface enhanced spectroscope [6–10]. It is because they have large absorption and scattering coefficients. Furthermore, noble metal nanoparticles can be synthesized in different components, shapes (e.g., nanowire, nanodisk, nanorod, nanosphere, nanocube, and core-shell structure), and geometrical configurations, with which they can be self-assembled into different complex nanostructures required. Through these methods, the interaction between light and materials can be controlled and manipulated at a certain wavelength scale when they are used in energy harvesting/conversion and optical devices. Recently, a method is developed to enhance the efficiency and stabilize the emission spectrum in organic light-emitting diodes (OLEDs) using

a light scattering layer fabricated with silver nanowires [11]. It is enhanced by 49.1% for the integrated external quantum efficiency. To reduce the usage of semiconductor materials, self-assembled gold nanorods are used to increase the photoconductivity in thin amorphous silicon semiconducting films. It is enhanced by a factor of 2 across the entire visible spectrum [12]. However, the high cost of noble metal nanoparticles has hindered their practical use.

In recent years, there are significant efforts to search cheap metal nanoparticles in order to displace noble metal nanoparticles such as Au, Ag, and Pt, although the studies still have little research. Recently, aluminum nanoparticle and copper nanoparticles have attracted interest as alternative candidates. In order to enhance the solar absorption, a method is suggested to fabricate aluminum nanoparticles based structure using a porous template assisted self-assembly process [13]. It is demonstrated that the effective solar absorption can be over 96%. However, the plasmon resonance wavelength of aluminum nanoparticles lies at the wavelength of around 150 nm. In order to be used in energy harvesting/conversion devices, it should be shifted with changing the shape and geometrical configurations of aluminum nanoparticles. Due to its high oxidation activity, it is difficult to synthesize

various shapes such as nanosphere, nanowire, and nanorod using a simple and cheap method. Copper nanoparticles are promising for these applications because of their considerably low cost compared to Ag, Au, and Pt, high electrical and thermal conductivities, and excellent resistance to ion migration. Furthermore, the plasmon resonance wavelength of copper nanoparticles lies in the visible wavelength region, similar to that of gold and silver nanoparticles. The scattering efficiency can be varied by changing shapes and geometrical configurations. Compared with the difficulty of synthesizing aluminum nanoparticles, various shapes and geometrical configurations of copper nanoparticles and copper based alloy nanoparticles have been synthesized by physical, chemical, and biological methods [2]. The study of various geometrical configurations and shapes has been conducted thoroughly and substantial progress has been made [14]. However, only little research has been focused on enhancing luminescence of laser dye or rare-earth by plasmonic coupling and scattering of copper nanoparticles [15, 16]. In addition, there are many reports on preparing nanoparticles film using self-assembly technique (utilizing the chemical interaction between nanoparticles and the surface), lithography, and spin coating methods [17–19]. Among these methods, the spin coating method has getting attractions because self-assembly technique and lithography methods need a lot of procedures. Ag nanoparticle film is fabricated by the spin coating method and the sintering effect is investigated [20]. Unfortunately, there are few reports on preparing copper nanoparticles film using spin coating method.

In this paper, a simpler and cheaper method by the spin coating was used to fabricate copper nanoparticle based films on glass slides. Due to the importance of the shapes of copper nanoparticles when they are used in energy harvesting/conversion and optical devices, the influence of heat treatment on the sizes and morphologies of copper nanoparticles based film was investigated.

2. Experimental Details

2.1. Preparation of Copper Nanoparticles. Copper nanoparticles were synthesized by a mature polyol method in ambient atmosphere. Details of preparation process were described elsewhere [21]. The sodium hypophosphite monohydrate ($\text{NaH}_2\text{PO}_2 \cdot \text{H}_2\text{O}$), copper nitrate trihydrate ($\text{Cu}(\text{NO}_3)_2 \cdot 3\text{H}_2\text{O}$), ethylene glycol, and polyvinylpyrrolidone (PVP, K29-32) were purchased from Aladdin Chemical Reagent Co. Ltd., P. R. China. The average molecular weight of the PVP polymer used was 58000. All the chemical reagents were used as received. PVP was used to get an organic shell on the surface of copper nanoparticles for avoiding being oxidized. The following procedure was used to prepare copper nanoparticles. First, 4 g $\text{NaH}_2\text{PO}_2 \cdot \text{H}_2\text{O}$ and 2.5 g PVP were dissolved into 40 mL ethylene glycol at 90°C. Then, 10 mL of 1 M ethylene glycol solution of $\text{Cu}(\text{NO}_3)_2 \cdot 3\text{H}_2\text{O}$ at 90°C was injected into the above prepared solution of $\text{NaH}_2\text{PO}_2 \cdot \text{H}_2\text{O}$ and PVP polymer under vigorously stirring.

The mixture solution was stirred for about 10 minutes and cooled down to room temperature. Finally, the prepared copper nanoparticles were separated by centrifugation, washed with absolute alcohol, and repeated for three times. After the above steps, it was well-dispersed in absolute alcohol again and the suspension can be stable for several weeks.

2.2. Preparation of Copper Nanoparticle Based Films. To get the copper nanoparticle based films on glass slides, the required concentration of copper nanoparticles in absolute alcohol (0.4 g/4 g) was prepared under ultrasonic treatment for about 30 minutes. After setting well washed glass slides on the disk of the spin-coater machine, the solution of copper nanoparticles was dropped and spin-coated with 1000 rev. min⁻¹ for 12 seconds in air. Finally, the glass slides were kept in a tube furnace and annealed in a 5% $\text{H}_2\text{-N}_2$ mix gas atmosphere for one hour at 100°C, 150°C, 200°C, 300°C, and 400°C, respectively.

2.3. Characterization of As-Prepared Copper Nanoparticles and Annealed Copper Nanoparticles Based Films. Thermo-gravimetric measurement (TG) was carried out by SMP/PF7548/MET/600W thermogravimetric/differential thermal analyzer from the Swiss Mettler company. The heating rate is 10°C/minute of the heating rate with argon as a testing atmosphere. The size and morphology of copper nanoparticles was investigated by scanning electron microscopy (SEM) using a Hitachi SU8010 field-emission scanning electron microscope. X-ray diffraction (XRD) patterns were obtained on a D2 Phaser Benchtop XRD system (Bruker AXS, Germany).

3. Results and Discussion

To investigate the relation between the scattering and absorbing intensity with the size of copper nanoparticles, the extinction, scattering, and absorbing spectra of copper nanoparticles are simulated by Mie theory given by BHMIE code [22]. The Drude-Lorentz model for copper is obtained from by Ung and Sheng [23] The Drude-Lorentz parameters for copper are obtained from Rakić et al. [24]. The diameters of spherical nanoparticle considered are 120 nm, 160 nm, 320 nm, and 640 nm, respectively. Figure 1 shows the extinction, scattering and absorbing spectra of copper nanoparticles with different diameters. It has been found that the tunability of extinction, scattering, and absorbing efficiency can be controlled effectively by change in diameters of copper nanoparticles. The methods of varying the diameters of copper nanoparticles here are heat treatment.

Figure 2 shows the XRD patterns of the as-prepared copper nanoparticles based films on glass slides. The results are in agreement with the values for a face-centered cubic crystal structure of copper phase (JCPDS number 04-0836). The peaks at $2\theta = 43.17^\circ$, 50.33° , and 74.16° correspond to (111), (200) and (220) Bragg reflections, respectively. No observed diffraction peaks are detected from any other impurities. These results identify that, under the protection

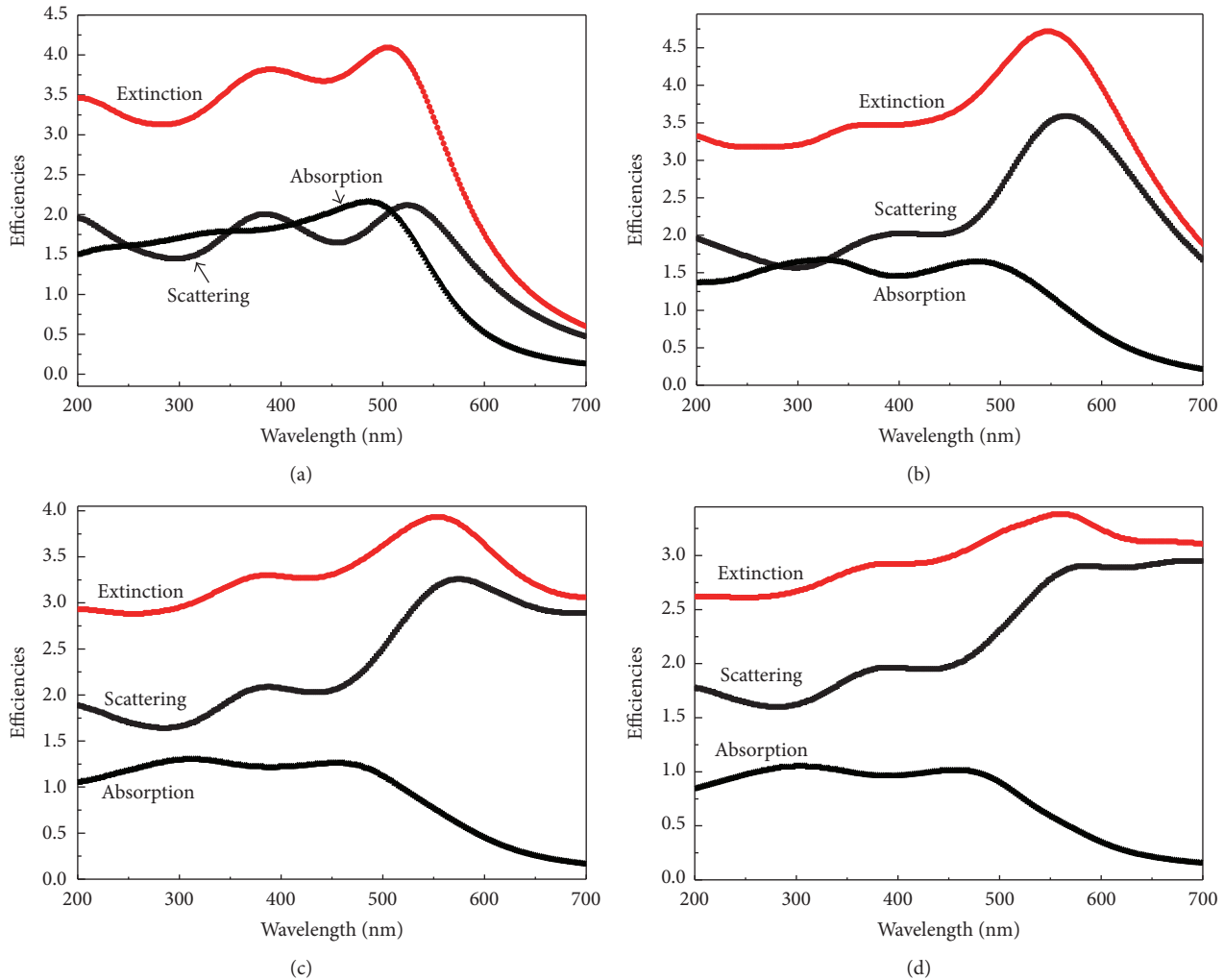


FIGURE 1: Calculated extinction, scattering, and absorption spectra of copper nanoparticles with different diameters. (a) 120 nm, (b) 160 nm, (c) 320 nm, and (d) 640 nm.

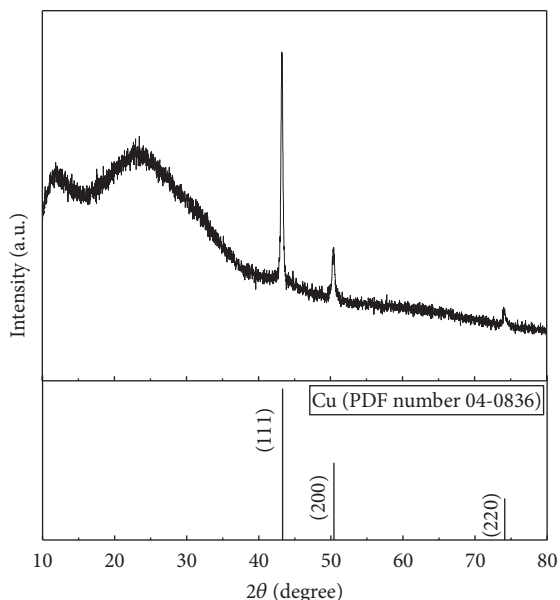


FIGURE 2: XRD diffraction patterns of the as-prepared copper nanoparticles based films on glass slides without anneal.

by PVP polymer, the as-prepared copper nanoparticles are hardly oxidized into Cu_2O , CuO , or $\text{Cu}(\text{OH})_2$. The sharp and strong diffraction peaks confirm that the as-prepared copper nanoparticles are highly crystalline.

TG analysis in an Ar atmosphere was used to study thermal decomposition behaviors of the as-prepared PVP coated copper nanoparticles, shown in Figure 3. An Ar atmosphere was used for TG measurement in order to prevent the oxidation of copper nanoparticles. The results indicate that the weight loss of $\sim 2.5\%$, which could be attributed to small amount of absolute alcohol, ethylene glycol, and PVP polymer absorbed on the surface of as-prepared copper nanoparticles. The weight increases again at temperature over 600°C , which is ascribed to the oxidation of Cu nanoparticles.

To investigate the oxidation protection performance of copper nanoparticles based films on glass slides, XRD patterns are measured at different heat treatment temperatures. According to TG analysis shown in Figure 3, the copper nanoparticles based films were annealed in a 5% $\text{H}_2\text{-N}_2$ atmosphere for one hour at 100°C , 150°C , 200°C , 300°C , and 400°C , respectively. Considering the glass transition

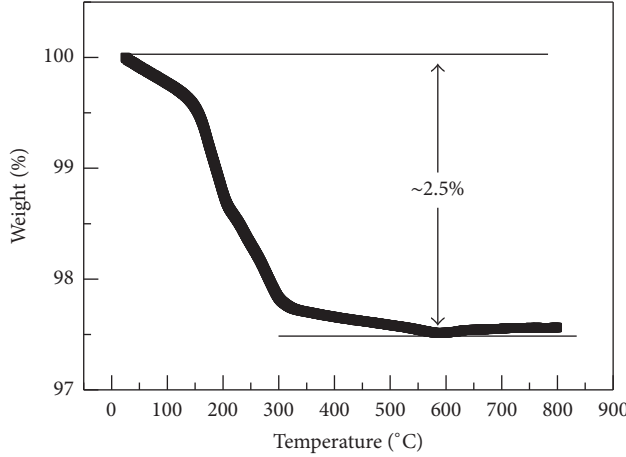


FIGURE 3: Thermal analysis of the as-prepared copper nanoparticles with argon as a testing atmosphere.

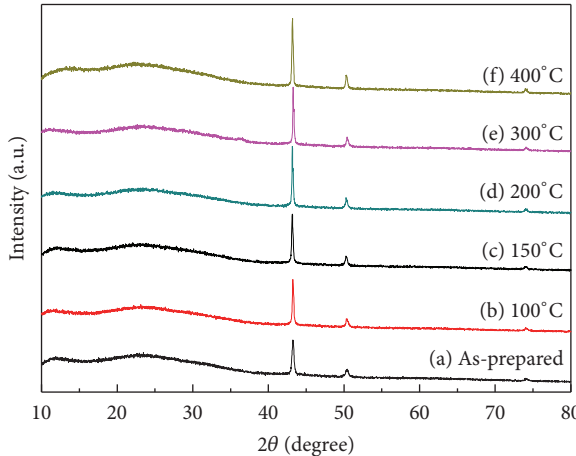


FIGURE 4: XRD diffraction patterns of the copper nanoparticles based films on glass slides annealed at different heat treatment temperatures by a spin coating method: (a) as-prepared, (b) 100°C, (c) 150°C, (d) 200°C, (e) 300°C, and (f) 400°C.

temperature of glass slides used as substrates, the highest heat treatment temperature used is 400°C. As shown in Figure 4, the intensity of the XRD peaks increases with heat treatment temperature from room temperature to 400°C. These results show that the crystallizations of copper nanoparticles in the films become better. There are no observed characteristic peaks attributed to oxide impurities such as Cu₂O, CuO, or Cu(OH)₂ till 400°C.

Due to the importance of the shapes and geometrical configurations of copper nanoparticles when used in energy harvesting/conversion and optical devices, it is significant to control the size and morphologies of copper nanoparticles. One of the simple methods to control them is changing the parameters of heat treatment process. Under heat treatment the residual solvent and organics are removed, leading to coalescence between adjacent copper nanoparticles. Figure 5 shows SEM images of the copper nanoparticles based films on

glass slides. These results show that the copper nanoparticles pack to a multilayered structure. When heat treated at temperature under 200°C, the morphologies of copper nanoparticles are still isolated nanoparticles, which are independent of heat treatment and the distributions of the size of copper nanoparticles are not uniform, shown in Figures 5(a)–5(c). The sintering process has not happened at these temperatures. However, when the heat treatment temperature increases to 200°C, the copper nanoparticles start to melt as shown in Figure 5(d). As the heat treatment temperature increases to 300°C, the size of copper nanoparticles increases obviously, as shown in Figure 5(e). When the heat treatment temperature increases to 400°C, the size of copper nanoparticles continues to increase and some copper nanoparticles are interconnected, indicating that apparent sintering necks appeared. Furthermore, significant coarsening can be observed, shown in Figure 5(f).

4. Conclusions

We have reported on the influence of heat treatment on the sizes and morphologies of copper nanoparticles based films by a simple spin coating method. The heat treatment of copper nanoparticles based films on glass slide may be a promising method for modulating the sizes and morphologies of copper nanoparticles. When increasing the heat treatment temperature, the size keeps no obvious change while increasing at a critical heat treatment temperature. Significant coarsening of copper nanoparticles occurs when it continues increasing heat treatment temperature. Through this method it may be helpful to vary the scattering and absorbing intensity of copper nanoparticles within the entire visible spectrum.

Conflicts of Interest

The authors declare that they have no conflicts of interest.

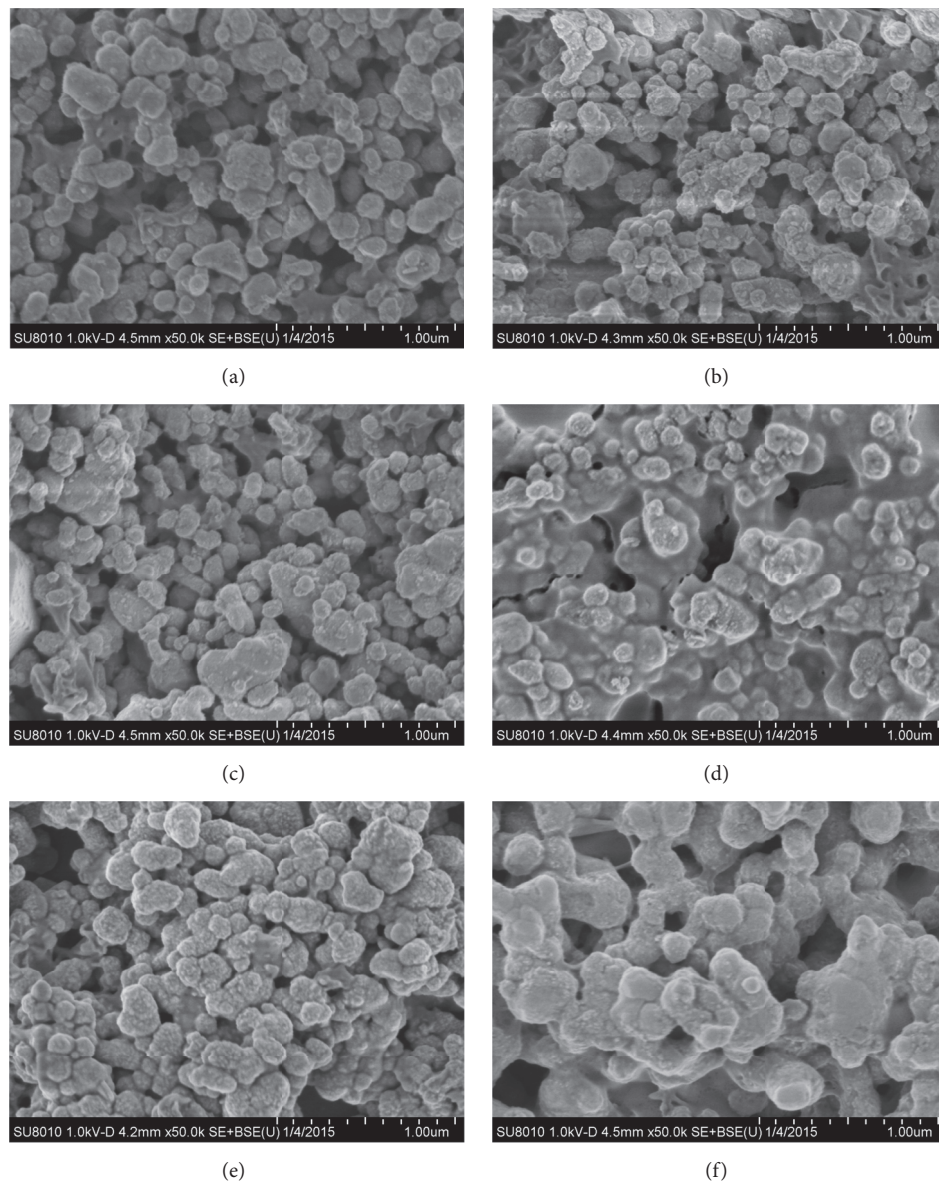


FIGURE 5: SEM images of the copper nanoparticles based films on glass slides at different heat treatment temperatures by a spin coating method: (a) as-prepared, (b) 100°C, (c) 150°C, (d) 200°C, (e) 300°C, and (f) 400°C.

Acknowledgments

This work is partially supported by the Natural Science Foundation of Zhejiang (LY16F050005).

References

- [1] S. Sarfraz, A. T. Garcia-Esparza, A. Jedidi, L. Cavallo, and K. Takanabe, “Cu-Sn bimetallic catalyst for selective aqueous electroreduction of CO₂ to CO,” *ACS Catalysis*, vol. 6, no. 5, pp. 2842–2851, 2016.
- [2] M. B. Gawande, A. Goswami, F.-X. Felpin et al., “Cu and Cu-based nanoparticles: synthesis and applications in catalysis,” *Chemical Reviews*, vol. 116, no. 6, pp. 3722–3811, 2016.
- [3] K. J. Carroll, J. Ulises Reveles, M. D. Shultz, S. N. Khanna, and E. E. Carpenter, “Preparation of elemental Cu and Ni nanoparticles by the polyol method: an experimental and theoretical approach,” *Journal of Physical Chemistry C*, vol. 115, no. 6, pp. 2656–2664, 2011.
- [4] C. Schöttle, P. Bockstaller, D. Gerthsen, and C. Feldmann, “Tungsten nanoparticles from liquid-ammonia-based synthesis,” *Chemical Communications*, vol. 50, no. 35, pp. 4547–4550, 2014.
- [5] H. Shirai, M. T. Nguyen, Y. Ishida, and T. Yonezawa, “A new approach for additive-free room temperature sintering of conductive patterns using polymer-stabilized Sn nanoparticles,” *Journal of Materials Chemistry C*, vol. 4, no. 11, pp. 2228–2234, 2016.
- [6] X. Liu and D. Y. Lei, “Simultaneous excitation and emission enhancements in upconversion luminescence using plasmonic double-resonant gold nanorods,” *Scientific Reports*, vol. 5, Article ID 15235, 2015.

- [7] J. Henzie, S. C. Andrews, X. Y. Ling, Z. Li, and P. Yang, "Oriented assembly of polyhedral plasmonic nanoparticle clusters," *Proceedings of the National Academy of Sciences of the United States of America*, vol. 110, no. 17, pp. 6640–6645, 2013.
- [8] H. Zhang, M. Cao, W. Wu, H. Xu, S. Cheng, and L.-J. Fan, "Polyacrylonitrile/noble metal SiO₂ nanofibers as substrates for the amplified detection of picomolar amounts of metal ions through Plasmon-enhanced fluorescence," *Nanoscale*, vol. 7, no. 4, pp. 1374–1382, 2015.
- [9] D. D. Liana, B. Raguse, J. J. Gooding, and E. Chow, "Toward paper-based sensors: turning electrical signals into an optical readout system," *ACS Applied Materials and Interfaces*, vol. 7, no. 34, pp. 19201–19209, 2015.
- [10] K. Suganuma, S. Sakamoto, N. Kagami, D. Wakuda, K.-S. Kim, and M. Nogi, "Low-temperature low-pressure die attach with hybrid silver particle paste," *Microelectronics Reliability*, vol. 52, no. 2, pp. 375–380, 2012.
- [11] K. Lee, J.-W. Shin, J.-H. Park et al., "A light scattering layer for internal light extraction of organic light-emitting diodes based on silver nanowires," *ACS Applied Materials and Interfaces*, vol. 8, no. 27, pp. 17409–17415, 2016.
- [12] C.-S. Chang and L. J. Rothberg, "Plasmon-enhanced photoconductivity in amorphous silicon thin films by use of thermally stable silica-coated gold nanorods," *Chemistry of Materials*, vol. 27, no. 9, pp. 3211–3215, 2015.
- [13] L. Zhou, Y. Tan, J. Wang et al., "3D self-assembly of aluminium nanoparticles for plasmon-enhanced solar desalination," *Nature Photonics*, vol. 10, no. 6, pp. 393–398, 2016.
- [14] S. Bhanushali, P. Ghosh, A. Ganesh, and W. Cheng, "1D copper nanostructures: progress, challenges and opportunities," *Small*, vol. 11, no. 11, pp. 1232–1252, 2015.
- [15] R. Reisfeld, M. Grinberg, V. Levchenko et al., "Sol-gel glasses with enhanced luminescence of laser dye Rhodamine B due to plasmonic coupling by copper nanoparticles," *Optical Materials*, vol. 36, no. 10, pp. 1611–1615, 2014.
- [16] H. K. Dan, D. Zhou, R. Wang et al., "Effect of Copper nanoparticles on the enhancement of upconversion in the Tb³⁺/Yb³⁺ co-doped transparent glass-ceramics," *Optical Materials*, vol. 39, pp. 160–166, 2015.
- [17] Y.-K. Hong, H. Kim, G. Lee et al., "Controlled two-dimensional distribution of nanoparticles by spin-coating method," *Applied Physics Letters*, vol. 80, no. 5, pp. 844–846, 2002.
- [18] H. Kodama, S. Momose, N. Ihara, T. Uzumaki, and A. Tanaka, "Disk substrate deposition techniques for monodisperse chemically synthesized FePt nanoparticle media," *Applied Physics Letters*, vol. 83, no. 25, pp. 5253–5255, 2003.
- [19] S. Li, W. Li, Q. Liu et al., "Spin-coated Ag nanoparticles onto ITO substrates for efficient improvement of polymer solar cell performance," *Journal of Materials Chemistry C*, vol. 3, no. 6, pp. 1319–1324, 2015.
- [20] K.-S. Chou, K.-C. Huang, and H.-H. Lee, "Fabrication and sintering effect on the morphologies and conductivity of nano-Ag particle films by the spin coating method," *Nanotechnology*, vol. 16, no. 6, pp. 779–784, 2005.
- [21] J. Yan, G. Zou, A. Hu, and Y. N. Zhou, "Preparation of PVP coated Cu NPs and the application for low-temperature bonding," *Journal of Materials Chemistry*, vol. 21, no. 40, pp. 15981–15986, 2011.
- [22] C. F. Bohren and D. R. Huffman, *Absorption and Scattering of Light by Small Particles*, Wiley, New York, NY, USA, 1998.
- [23] B. Ung and Y. Sheng, "Interference of surface waves in a metallic nanoslit," *Optics Express*, vol. 15, no. 3, pp. 1182–1190, 2007.
- [24] A. D. Rakić, A. B. Djurišić, J. M. Elazar, and M. L. Majewski, "Optical properties of metallic films for vertical-cavity optoelectronic devices," *Applied Optics*, vol. 37, no. 22, pp. 5271–5283, 1998.